

STUDY OF THERMOELECTRIC GENERATORS AND PEROVSKITE SOLAR CELLS  
FOR RENEWABLE ENERGY APPLICATIONS

by

ZHONGLIANG OUYANG

DAWEN LI, COMMITTEE CHAIR  
GREGORY THOMPSON  
GARY MANKEY  
GREG SZULCZEWSKI  
HAIBIN NING

A DISSERTATION

Submitted in partial fulfillment of the requirements  
for the degree of Doctor of Philosophy  
in the Department of Electrical and Computer Engineering  
in the Graduate School of  
The University of Alabama

TUSCALOOSA, ALABAMA

2020

Copyright Zhongliang Ouyang 2020  
ALL RIGHTS RESERVED

## ABSTRACT

This dissertation aims at explorations of two promising renewable energy devices: one is thermoelectric generators (TEGs) and the other is perovskite solar cells (PVSCs). The first half of this dissertation (Chapter 2 & 3) focuses on the simulation study of TEGs while the second half (Chapter 4 & 5) concentrates on the experimental study of PVSCs. Chapter 1 serves as an overall introduction of TEGs and PVSCs.

Chapter 2 investigates simulation of segmented TEGs with various state-of-the-art thermoelectric (TE) materials between 300 K and 1000 K. The influence of thermal radiation, electrical and thermal contact effects have been studied. The results show that these effects, if well-regulated, do not prevent segmented TEGs from achieving high efficiency and output power density.

In Chapter 3, segmented TEGs have been further modelled to find out the best cost-performance ratios. The results reveal that successful segmentation of TE materials can offer a cost-performance ratio of  $\sim 0.86 \text{ \$ W}^{-1}$ , less than commercially desired cost-effectiveness of  $1 \text{ \$ W}^{-1}$ , while maintaining an efficiency of 17.8% and delivering a power density over 3 Watt  $\text{cm}^{-2}$ . These results predict the commercial feasibility and competitiveness of segmented TEGs in the same dollar per watt metrics as other renewable energy devices.

Chapter 4 presents a rapid layer-specific annealing on perovskite active layer enabled by ultraviolet (UV) light-emitting diode (LED) and efficiency close to 19% is achieved in a simple planar inverted structure. These results justify that if the UV dosage is well-managed,

UV light is capable of annealing perovskite into high-quality film rather than simply damaging it. Moreover, the layer-specific photonic treatment allows accurately estimating the deposition energy required to form perovskite film at device quality level.

Chapter 5 exhibits an effort towards scalable manufacturing of perovskite solar panels. Perovskite mini-modules have been demonstrated with blade-coating and rapid thermal processing (RTP) in ambient environment. Mini-modules with an active area over 2.7 cm<sup>2</sup> exhibit a champion efficiency of 17.73%. These results pave the way for large-scale production of PVSCs through high-speed roll-to-roll printing.

Chapter 6 summarizes the conclusions and proposes a possible future work.

## **DEDICATION**

This dissertation is dedicated to my family.

## LIST OF ABBREVIATIONS AND SYMBOLS

TEG Thermoelectric generator

TE Thermoelectric

$P$  Output power

$I_e$  Electrical current

$\alpha$  Seebeck coefficient

$\rho$  Electrical resistivity

$R$  Resistance

$\sigma$  Electrical conductivity

$\kappa$  Thermal conductivity

$T$  Absolute temperature

$T_h, T_H$  Temperatures of TEG's hot side

$T_c, T_C$  Temperatures of TEG's cold side

$ZT$  Figure of merit

$L, l$  TEG leg length

$A$  Cross-section area of the TEG leg

Subscript  $n$  n-type

Subscript  $p$  p-type

$\vec{q}$  Heat flux

$\vec{J}$  Electric current density

$\vec{E}$  Electric field

$\eta$  Efficiency

*C.P.* Cost-performance

$C_{tot}$  Overnight capital cost

$D$  Density

$F$  Fill factor of TEG

$h$  Heat transfer coefficients

$\Omega_g$  Gravimetric material prices

$\Omega_{M,g}$  Gravimetric manufacturing price

$\Omega_{M,A}$  Areal manufacturing price

$\Omega_{HX}$  Heat exchanger price

PVSCs Perovskite solar cells

PVK Perovskite

UV Ultraviolet

LED Light-emitting diode

PCE Power-conversion efficiency of PVSCs

$FF$  Fill factor of PVSCs

$V_{OC}$  Open-circuit voltage of PVSCs

$J_{SC}$  Short-circuit current density of PVSCs

EQE External quantum efficiency

$A$  Absorption of light

$k$  Extinction coefficient

$z$  Thickness

$\lambda$  Wavelength

$E$  Energy

$S$  Area of the PVSCs

$I$  UV irradiance

$t$  Time of UV exposure

$Q$  Heat

$C_p$  Specific heat

RTP Rapid thermal processing

MPP Maximal power point of PVSCs

## **ACKNOWLEDGMENTS**

I want to take this chance to thank everyone who has helped me with my Ph.D. study and research at The University of Alabama. I am fortunate to have you around in this journey.

First, I would like to express my great gratitude for my advisor, Dr. Dawen Li. Dr. Li is not only a knowledgeable mentor but also a sincere friend, who has been providing me with persistent help, continuous guidance and valuable advice. Without Dr. Li, I wouldn't be able to carry out these interesting projects and would not have the opportunity to improve myself through the exploration in the related fields.

Next, I would like to thank my committee members, Dr. Greg Thompson, Dr. Gary Mankey, Dr. Greg Szulczewski and Dr. Haibin Ning, for their great help and inspiring questions of both my academic study and dissertation writing.

Also, I would like to thank my colleagues. I would like to thank Dr. Sheng Bi, Dr. Ziyou Zhou, Dr. Shoieb Shaik for their help and collaboration. I would also thank Dr. Maikel F. A. M. van Hest, Dr. Mengjin Yang and Dr. James B. Whitaker for their help during my time at National Renewable Energy Laboratory.

I thank financial supports from National Science Foundation (NSF) and the scholarships from both the Materials Science program and the MINT center.

Last but not least, I would like to thank my family who have always been supportive of me. Their great love, care and understanding is the most motivation with which I complete my Ph. D. study and research.

## CONTENTS

ABSTRACT .....	ii
DEDICATION .....	iv
LIST OF ABBREVIATIONS AND SYMBOLS .....	v
ACKNOWLEDGMENTS .....	viii
LIST OF TABLES .....	xii
LIST OF FIGURES .....	xiii
CHAPTER 1. INTRODUCTION .....	1
1.1 Thermoelectric Generators (TEGs).....	2
1.2 Perovskite Solar Cells (PVSCs).....	5
CHAPTER 2. MODELLING OF SEGMENTED HIGH-PERFORMANCE THERMOELECTRIC GENERATORS WITH EFFECTS OF THERMAL RADIATION, ELECTRICAL AND THERMAL CONTACT RESISTANCES .....	9
2.1 Method .....	10
2.1.1 Governing Equations .....	10
2.1.2 Material Properties.....	13
2.1.3 TEG Leg Geometries .....	16
2.2 Results and Discussion .....	18
2.2.1 Symmetrical Models .....	18
2.2.2 Non-symmetrical Models.....	21
2.2.3 Compatibility of Segmented TE Materials .....	24

2.2.4 Thicknesses of Individual Segments.....	27
2.2.5 Thermal Radiation Loss .....	28
2.2.6 Contact Resistances .....	30
<b>CHAPTER 3. DESIGN OF SEGMENTED HIGH-PERFORMANCE THERMOELECTRIC GENERATORS WITH COST IN CONSIDERATION .....</b>	<b>32</b>
3.1 Method .....	35
3.1.1 Governing Equations of TEG Physics .....	35
3.1.2 Cost–performance Metrics.....	37
3.1.3 Properties of Segmented TE Materials and Contact Resistances .....	41
3.1.4 TEG Module Geometries .....	44
3.2 Results and Discussion .....	46
3.2.1 Optimization of $An/Ap$ Geometrical Ratio.....	46
3.2.2 Optimization for Cost Performance .....	50
<b>CHAPTER 4. RAPID LAYER-SPECIFIC ANNEALING ENABLED BY ULTRAVIOLET LED WITH ESTIMATION OF DEPOSITION ENERGY FOR HIGH-PERFORMANCE PEROVSKITE SOLAR CELLS .....</b>	<b>57</b>
4.1 Experimental Section .....	58
4.2 Results and Discussion .....	60
4.2.1 UV-LED-annealing of $\text{MAPbI}_3$ and $\text{PC}_{71}\text{BM}$ Films.....	60
4.2.2 Photovoltaic (PV) Performances of PVSCs with UV-LED-annealing Only on PVSK Layer .....	63
4.2.3 Device Performance with UV-LED-annealing for Both $\text{MAPbI}_3$ PVSK Active Layer and $\text{PC}_{71}\text{BM}$ ETL Layer .....	67
4.2.4 Characterization of PVSK Thin Films for Comparison in Performance .....	74
4.2.5 Deposition energy of PVSK Films .....	78

CHAPTER 5. TOWARDS SCALABLE PEROVSKITE SOLAR MODULES USING BLADE-COATING AND RAPID THERMAL PROCESSING .....	85
5.1 Experimental Section .....	88
5.2 Results and Discussion .....	91
5.2.1 Thermal Budget of RTP on Perovskite Layer .....	91
5.2.2 Upscaling of PVSCs .....	98
CHAPTER 6. CONCLUSIONS AND FUTURE WORK .....	101
6.1 Conclusions.....	101
6.2. Future Work .....	105
REFERENCES .....	108
APPENDIX.....	118
LIST OF PUBLICATIONS AND PATENTS .....	118
Journal Publications .....	118
Patents .....	119

## LIST OF TABLES

<b>Table 1.</b> Temperature dependence of $ZTs$ and Seebeck coefficients for used TE materials....	14
<b>Table 2.</b> Temperature dependence of resistivities $\rho$ ( $\times 10^{-5} \Omega m$ ) and thermal conductivities $\kappa$ ( $W m^{-1} K^{-1}$ ) for the used TE materials. ....	15
<b>Table 3.</b> Temperature dependence of resistivity ( $\Omega m$ ) and thermal conductivity ( $W m^{-1} K^{-1}$ ) for copper contacts.....	15
<b>Table 4.</b> Dimensions of non-symmetrical models. ....	18
<b>Table 5.</b> Comparison of optimal $An/Ap$ ratios between 3D simulation and estimation from Equation (14). .....	24
<b>Table 6.</b> Densities and prices of TE materials used in this study. <sup>[13-16, 28-29, 31, 93, 96-99]</sup> .....	40
<b>Table 7.</b> TEG manufacturing cost and heat exchanger prices used in this study. <sup>[92-93, 100]</sup> .....	40
<b>Table 8.</b> Photovoltaic parameters of devices from both the UV- and thermal-annealing.....	65
<b>Table 9.</b> Physical properties of materials for different layers.....	80
<b>Table 10.</b> Optimization process of RTP versus hot-plate annealing. Active area = $0.105 cm^2$ . ....	93

## LIST OF FIGURES

<b>Figure 1.</b> A schematic TEG model with segmented legs. ....	16
<b>Figure 2.</b> Illustration of a) symmetrical model with $8 \times 8$ legs, and b) non-symmetrical model with $2 \times 2$ legs used in simulation. ....	17
<b>Figure 3.</b> a) Efficiency of thermoelectric modules versus total number of TEG legs. The leg thickness is set to be 10 mm. b) Efficiency versus thickness of TEG legs, which is based on 256 ( $16 \times 16$ ) total number of TEG legs. c) The required heat power versus leg thickness with various temperature differences. d) Effects of number of TEG legs on output current, output voltage and output power. The temperature difference $\Delta T = 500K$ , and leg thickness $L = 10$ mm. ....	20
<b>Figure 4.</b> TEG efficiency (a, b & c) and output power per unit area (d, e & f) at different geometrical ratios. For all three TEG modules, the maximum efficiency is indeed achieved using non-symmetrical cross-section areas. The non-symmetrical TEG modules are built with the best p-type TE materials along with a) & d) n-type 1, b) & e) n-type 2, and c) & f) n-type 3 TE materials. ....	22
<b>Figure 5.</b> a) TEG Efficiency vs. temperature differences for TEGs with the combination of the current best p-type and the present strongest n-type TE materials (inset: TEG efficiency vs. hot side temperature at different $ZT$ values, where cold side temperature has been set to 300K). b) & c) Compatibility factors of the series of best p-type and strongest n-type TE materials, respectively. The dashed lines indicate the interfaces between segments. ....	26
<b>Figure 6.</b> a) TEG Efficiency vs. geometrical ratios of the best p-type teaming with 3 or 4 layers of the strongest n-type TE materials @ $\Delta T = 700$ K. b) Compatibility factors of the $BaLaYbCo_4Sb_{12}$ layer in comparison with the other three layers.....	27
<b>Figure 7.</b> Temperature distribution in a 3D non-symmetrical TEG module, $An/Ap = 0.141$ , with the best p-type TE materials and 3 layers of the strongest n-type TE materials.....	28
<b>Figure 8.</b> TEG efficiency, output power density and input heat density vs. emissivity/thermal radiation. ....	30
<b>Figure 9.</b> a) TEG efficiency and b) output power density vs. electrical contact resistance. c) TEG efficiency and d) output power density vs. thermal contact resistance.....	31

<b>Figure 10.</b> Schematic of the thermoelectric operation and parameter denotation. ....	36
<b>Figure 11.</b> $ZT$ values of (a) p-type and (b) n-type segmented TE materials at different operating temperature ranges. L, M, H denote low, medium and high temperatures, respectively. ....	43
<b>Figure 12.</b> Compatibility factors (a) & (b) and power factors (c) & (d) for p-type group 1 & group 2 and n-type group 1 & group 2, respectively. ....	44
<b>Figure 13.</b> Typical current-dependency of the output voltage, efficiency and output power density in a segmented TEG. ....	47
<b>Figure 14.</b> a) Modelling example of segmented TEG modules, and b) the corresponding temperature distribution. ....	48
<b>Figure 15.</b> Optimal $An/Ap$ ratio for the highest output power densities and corresponding TEG efficiencies for different assemblies of two p-type legs and two n-type legs. ....	50
<b>Figure 16.</b> Cold side temperatures and output power densities of a TEG module versus the heat transfer coefficients at the cold side.....	51
<b>Figure 17.</b> Output power and corresponding heat transfer coefficients versus leg lengths of TEGs. ....	53
<b>Figure 18.</b> Cost-performance ratio versus leg lengths of different TEG modules. ....	54
<b>Figure 19.</b> Cost-performance ratios, TEG efficiencies and power densities versus different cold-side temperature and fixed hot-side temperature at 1000 K. The unit price of $10 \text{ \$ W}^{-1} \text{ K}$ for heat exchangers is used here. ....	56
<b>Figure 20.</b> (a) spectral extinction coefficients of $\text{MAPbI}_3$ PVS film; (b) illustration of UV annealing on the PVS light-absorbing (active) layer, which starts as the transparent MAI- $\text{PbI}_2$ -DMSO adduct; c) dark brown $\text{MAPbI}_3$ film forms after proper UV annealing ( $> 9$ seconds) and (d) illustration of UV annealing on the PCBM ETL layer, which doesn't show any visible color change. ....	63
<b>Figure 21.</b> a) Performance comparison between thermal-annealed and UV-annealed PVSCs; b) the J-V characteristics of PVSCs in reverse scan with different UV annealing time from 7s to 13s on the PVS active layer only. For all the devices involved, no annealing of any kind (neither thermal nor UV annealing) was applied on $\text{PC}_{71}\text{BM}$ layers.....	65
<b>Figure 22.</b> a) J-V curves with apparent hysteretic behavior at different scan rates. PVSCs with UV annealing of 11s (100% intensity) on the $\text{MAPbI}_3$ layer but no UV annealing on the $\text{PC}_{71}\text{BM}$ layer. b) Hysteresis-free J-V characteristics at different scan rates, which are from the best PVSCs with the optimized UV-LED-annealing conditions: 11s (100% intensity) on the	

MAPbI<sub>3</sub> active layer and 1s (10% intensity) on the PC<sub>71</sub>BM ETL layer.....66

**Figure 23.** Cross-sectional SEM images of a) MAI-PbI<sub>2</sub>-DMSO / PEDOT:PSS / ITO / glass before any annealing, b) Al/PC<sub>71</sub>BM/MAPbI<sub>3</sub>/PEDOT:PSS/ITO with PVK layer & PC<sub>71</sub>BM layer annealed by UV for 11s (100%) & 1s (10%), respectively and c) Al/PC<sub>71</sub>BM/MAPbI<sub>3</sub>/PEDOT:PSS/ITO with both the PVK layer & PC<sub>71</sub>BM layer annealed by hot plate at 100 °C for 30 minutes.....69

**Figure 24.** Optimization of UV annealing on the PC<sub>71</sub>BM layer: a) using 100% UV intensity on PC<sub>71</sub>BM with different irradiation time from 0.5s to 2s; b) irradiating the PC<sub>71</sub>BM layer for 1s with different UV intensities from 10% to 50%, while result of 10% UV intensity for 0.5s on PC<sub>71</sub>BM is also included. For all the devices involving in the PC<sub>71</sub>BM annealing optimization, 11 seconds of 100% UV intensity were applied to the PVK layers.....70

**Figure 25.** Performance comparison between devices with different UV annealing times from 9s to 11s with the same UV annealing condition on the PC<sub>71</sub>BM layer: 10% UV intensity for 1s.....70

**Figure 26.** a) Hysteresis-free J-V characteristics of PVSCs with both PVK and PC<sub>71</sub>BM annealed (either UV-annealed or thermal-annealed); b) EQEs and integrated  $J_{scs}$  of the best thermal-annealed PVSC and the champion UV-annealed PVSC. Histograms of c) PVSCs (50 devices) with UV annealing of 11s (100% intensity) on the MAPbI<sub>3</sub> layer but no UV annealing on the PC<sub>71</sub>BM layer, and d) PVSCs (50 devices) with UV annealing of 11s (100% intensity) on the MAPbI<sub>3</sub> layer and UV annealing of 1s (10% intensity) on the PC<sub>71</sub>BM layer.....73

**Figure 27.** XRD characterization of perovskite thin films thermal-annealed at 100 °C for 30 minutes and UV-annealed samples with different irradiation times from 0s to 11s.....76

**Figure 28.** UV-Vis spectrum of perovskite thin film thermal-annealed at 100 °C for 30 minutes and UV-annealed samples with different illumination times from 7s to 13s.....76

**Figure 29.** Top-view SEM images of a) non-annealed MAI-PbI<sub>2</sub>-DMSO film, b)-e) MAPbI<sub>3</sub> films with varied UV annealing times of 7s, 9s, 11s & 13s, and f) MAPbI<sub>3</sub> film with thermal-annealing at 100 °C for 30 minutes. The scale bar is 1 micrometer. All PVK films are deposited on the PEDOT:PSS/ITO/glass substrates.....77

**Figure 30.** a) Schematic of transmission measurement through different layers, including cleaned ITO/glass, PEDOT:PSS/ITO/glass, and the conversion of MAI-PbI<sub>2</sub>-DMSO to MAPbI<sub>3</sub> on top of PEDOT:PSS/ITO/glass. The UV source intensity is labeled as 100% as benchmark for all the transmission percentage denotation. And b) transmission & reflection intensities during 11 seconds of UV irradiation. The PVK layer underwent a transformation from MAI-PbI<sub>2</sub>-DMSO adduct to MAPbI<sub>3</sub> during this 11-second period.....84

**Figure 31.** Trends of a) efficiency, b) FF, c)  $J_{sc}$  and d)  $V_{oc}$  at different RTP temperatures for

different time. Active area = 0.105 cm <sup>2</sup> .....	93
<b>Figure 32.</b> Trends of a) efficiency, b) <i>FF</i> , c) <i>J<sub>sc</sub></i> and d) <i>V<sub>oc</sub></i> at different RTP temperatures for 5, 10 and 20 seconds. Active area = 0.105 cm <sup>2</sup> .....	94
<b>Figure 33.</b> a) XRD and b) UV-Vis results of selected annealing conditions.....	95
<b>Figure 34.</b> Top-view SEM images of RTP films at a) 110 °C for 30 s, b) 140 °C for 20 s, c) hot-plate annealed at 140 °C for 2 minutes, d) 110 °C 5 s, and e) 250 °C 5 s. The scale bar is 1 $\mu$ m.....	96
<b>Figure 35.</b> a) J-V curves of RTP devices at 110 °C for 30 s & 140 °C for 20 s, and hot-plate annealed at 140 °C for 2 minutes. b) EQEs of the corresponding devices. ....	97
<b>Figure 36.</b> a) J-V curves of mini-modules made from RTP at 140 °C for 20 s and hot-plate annealed at 140 °C for 2 minutes. b) quasi-SPOs of the corresponding mini-modules. Active area = 2.7 cm <sup>2</sup> . Inset left: P-V curves of mini-modules; Inset right: photo of a mini-module. ....	99
<b>Figure 37.</b> Box charts of a) efficiency, b) <i>FF</i> , c) <i>J<sub>sc</sub></i> and d) <i>V<sub>oc</sub></i> for mini-modules annealed by RTP and hot plate. Active area = 2.7 cm <sup>2</sup> .....	100

## **CHAPTER 1. INTRODUCTION**

The development of the world depends on energy. With advances of the science and technology, there is an ever increasing demand for energy but concurrently exist a fear of depletion of traditional energy sources (fossil fuels) and concerns of the negative effects (such as global warming) associated with consuming conventional energy sources.

Renewable energy is the most promising solution to this dilemma. Of all the renewable energy, solar and thermal energy are the top two in terms of capacity. Other renewable energy, such as hydro, wind and biomass, are actually derivatives of the solar energy.

Thermal energy is widely present in every aspect of the world and the majority of it goes to waste. To crop thermal energy, the conventional way is via a heat engine and follows a tortuous path from the heat to mechanical energy and finally to electricity. A more straightforward technique using the so-called thermoelectric generators (TEGs) converts heat directly into electricity through Seebeck effect.<sup>[1]</sup> To harvest solar energy, the straightest method is through photovoltaic devices (also known as solar cells), of which the perovskite solar cells (PVSCs) are the rising star. The most direct approaches are always appealing but usually not the easiest ones. Currently, both TEGs and PVSCs are intensively-researched fields. While they are very promising, these two technologies have their respective issues.

The overall objectives of this PhD study are to advance the science and engineering of the above-mentioned two devices, i.e. TEGs and PVSCs, towards the final commercialization of them.

## 1.1 Thermoelectric Generators (TEGs)

As a promising renewable energy source, TEGs hold the potential to power everything from small electronics to large grids without any emission of greenhouse gas to the environment. TEGs are solid-state devices without moving parts, thus operating quietly, holding a long service life (over 30 years) and requiring almost no maintenance.<sup>[2-3]</sup> The huge amount of untamed heat, if properly utilized by TEGs, can help meet the ever-increasing energy demand around the globe. However, the thermoelectric (TE) technology has only found limited number of practical applications, the most well-known ones are powering the NASA space probes.<sup>[2, 4-6]</sup> Extensive studies have been conducted to make TEGs feasible in reality, however, thermoelectric (TE) technology is still far from being widely employed in practical applications.<sup>[3, 7-10]</sup> One of the major issues that hinders TEGs from large scale production and popularization would be the low thermal-to-electricity conversion efficiency, which is caused by the low figure of merit ( $ZT$ ) of thermoelectric materials.<sup>[11]</sup> Generally speaking,  $ZT \sim 1$  is an entry-level for a TE material to be practical.<sup>[12]</sup> Larger values are preferred and give rise to higher efficiencies.  $ZT$  is a temperature-dependent value and might vary drastically with little temperature change. Some prototype TE devices adopt TE materials with an average  $ZT$  below 1 over its operating temperature range, making the overall efficiencies of the devices far below 10%. TE materials have been widely studied and recent progress in  $ZT$  shows great promise in the development of new generation TEGs. Xie et al. developed p-type nanostructured  $(\text{Bi},\text{Sb})_2\text{Te}_3$  bulk materials with an average  $ZT \sim 1.4$  between 300 and 450K.<sup>[13]</sup> Zhao et al. synthesized a p-type MgAgSb-based bulk material with a maximum  $ZT$  of  $\sim 1.4$  at 475K.<sup>[14]</sup> In 2014, Wu et al. created p-type K-doped

$\text{PbTe}_{0.7}\text{S}_{0.3}$  bulk materials with a minimum and maximum  $ZT \sim 1.56$  at 550K and 2.2 at 800K, respectively.<sup>[15]</sup> Also in 2014, Zhao et al. manufactured p-type SnSe single crystals with an impressive  $ZT$  of  $2.6 \pm 0.3$  at 923K, along with an average  $ZT$  well above 2 from 800K to 975K.<sup>[16]</sup> The development of n-type TE materials, on the other hand, has experienced a gentle progress instead of an equally rapid one as p-type TE materials.<sup>[17-27]</sup> In the low temperature range (300K ~ 500K), Liu et al. fabricated Cu-Doped BiTeSe bulk materials maintaining an average  $ZT$  value slightly higher than unity.<sup>[28]</sup> In the mid-high temperature range, Hsu et al. exhibited a material system  $\text{AgPb}_m\text{SbTe}_{2+m}$  possessing a maximum  $ZT$  of 2.2 at 800K.<sup>[29]</sup> Beyond 800K, Shi et al. and Basu et al. introduced multiple-filled skutterudites with  $ZT = 1.7$  at 850 K<sup>[30]</sup> and silicon germanium alloys ( $\text{Si}_{80}\text{Ge}_{20}$ ) with  $ZT \sim 1.84$  at 1073 K<sup>[31]</sup>, respectively. Further enhancement of  $ZT$  value is a hard task and usually not achievable at low temperature.<sup>[1]</sup> In addition to  $ZT$ , according to the theory, the ultimate efficiency of a TEG is also determined and capped by the so-called Carnot efficiency  $\eta_c = (T_h - T_c)/T_h$ , where  $T_h$  and  $T_c$  are the temperatures of TEG's hot side and cold side, respectively.<sup>[32]</sup> Compared to enhancing  $ZT$ , it is relatively easier to augment the Carnot efficiency. If  $T_c$  is kept at a constant temperature, for example, room temperature, then higher  $T_h$  will lead to higher ultimate efficiencies of TEGs. In other words, big temperature gradient across the TEG could yield a high-efficiency outcome, assuming that the employed TE material would not deteriorate radically over a large temperature range.

Currently, no single TE material is qualified for this mission and different TE materials excel in their respective temperature ranges. Increasing the Carnot efficiency indicates that more than one TE material are needed since no single TE material possesses

high  $ZT$  values over a broad enough temperature range. One question arises naturally: is it possible to build TEGs with various TE materials and make them cooperate with each other to result in an overall high performance? There are two approaches to put various TE materials into cooperation for the same TEG device. One is using multi-stage design with different electrical circuits built for various TE materials working in different temperature stages.<sup>[33-35]</sup> This method places less restrictions on the selection of TE materials but introduces heat shunts from high temperature stages directly to the load.<sup>[36]</sup> The other strategy is segmenting TE materials continuously into the same electrical circuit.<sup>[37]</sup> This tactic doesn't have thermal energy loss through shunts but imposes relatively more stringent restraints on the selection of TE materials. A few researchers have done some work in this respect, for example, Snyder et al. introduced a function called compatibility factor that characterizes the feasibility of combining two or more TE materials without having them adversely interacting with each other.<sup>[36, 38]</sup> McEnaney et al. discussed the modelling of segmented TEGs using  $\text{Bi}_2\text{Te}_3$  and Skutterudite.<sup>[39]</sup> Hadjistassou et al. described a design method of segmented  $\text{Bi}_2\text{Te}_3-\text{PbTe}$  TEGs in terms of comparing the average and collective Seebeck coefficient of  $\text{Bi}_2\text{Te}_3-\text{PbTe}$  to that of the pure  $\text{Bi}_2\text{Te}_3$  and  $\text{PbTe}$  materials.<sup>[40]</sup> Ngan et al. provided an overview of theoretical efficiencies of segmented TEGs with various combinations of TE materials, by using a custom-made 1D numerical model.<sup>[41]</sup> However, there are few studies using the established 3D simulation environment, such as Ansys or Comsol, to accurately evaluate the performance of complex TEG modules with most up-to-date material combinations. For example, Xiao et al. analyzed one unicouple (a pair of p element and n element) model with bismuth telluride and filled-skutterudite.<sup>[33]</sup> Erturun et al. tested thermo-

mechanical performance of four-leg models by using BiTe and CoSb-based Skutterudite.<sup>[42]</sup>

One-unicouple models with various footprints were utilized by Rezania et al. to study the

optimization of power generation based on p-type  $Zn_4Sb_3$  and n-type  $Mg_2Si_{1-x}Sn_x$ .<sup>[43]</sup>

Nevertheless, these 3D models are simple in geometry with less number of TE unicouples,

and use out-of-date materials. Also their results were obtained without taking thermal transfer

loss and contact effects of any kind into consideration.

## **1.2 Perovskite Solar Cells (PVSCs)**

Perovskite solar cells (PVSCs) have experienced rapid development in the last ten

years with a record certified efficiency of 25.2% reported.<sup>[44-46]</sup> Compared to the dominant

technologies such as silicon photovoltaics, PVSCs have the great advantages of solution

processability and low-cost manufacturing potential.<sup>[47-56]</sup> However, the current mainstream

fabrication methods of PVSCs involve thermal annealing. Thermal annealing is a lengthy and

energy-inefficient process, serving as a potential bottleneck in the large-scale, commercial

production of PVSCs.<sup>[57-67]</sup> Thus, thermal annealing needs to be excluded from the chain of

fabrication before the economical manufacturing scale-up of PVSCs can be realized. As an

alternative, photonic energy can be utilized directly for many physical and chemical

processes, whereas thermal energy acts primarily by increasing the temperature and desired

changes come as a byproduct. So far, photonic treatments have been sparingly tried for

annealing the perovskite (PVSK) active layers despite the interesting effects light has on the

PVSK film and lattice.<sup>[68-70]</sup> Troughton et al. presented PVSCs with efficiency of 10.0% by

exposing the as-deposited mixed halide ( $CH_3NH_3PbI_{3-x}Cl_x$ ) PVSK film to a near-infrared

(NIR) halogen lamp for 2.5 seconds.<sup>[71]</sup> The same research group improved the power-conversion efficiencies (PCEs) of the same structure to 11.3% by photonic flash-annealing via a xenon lamp in 1.15 milliseconds.<sup>[72]</sup> Regardless of the lamp's type, their photon-annealed devices didn't perform as well as their hot-plate-annealed counterparts. Lavery et al. irradiated  $\text{CH}_3\text{NH}_3\text{PbI}_3$  thin film with intense light pulsed for 2 milliseconds from a xenon lamp. The resulting devices showed PCEs up to 12.3%, comparable to that of hot-plate-annealed samples.<sup>[73]</sup> Pool et al. applied radiative thermal annealing (RTA, also known as rapid thermal processing, RTP) to the formamidinium lead iodide ( $\text{FAPbI}_3$ ) PVK solar absorbers. They achieved PCEs up to 14.15% with the radiative thermal annealing, similar to their best efficiency of 13.80% from hot-plate thermal annealing.<sup>[74]</sup>

Although the above-mentioned studies employed photonic annealing, they couldn't take full advantage of photonic treatments because they never went beyond the concept of thermal annealing: they still used temperature to quantify the photonic annealing process. Also, their light sources were not energy efficient for the mission of PVSK annealing. They utilized sources which had wide wavelength distributions and part of their spectrums were infrared (IR) light radiation. This is not ideal because PVSK materials for photovoltaic purposes usually have an extremely weak absorption in the IR range.<sup>[75]</sup> For instance, a halogen lamp contains a major portion of IR light. As a direct result, the IR radiation will first heat everything else around the PVSK material but not the perovskite itself. The annealing energy as heat will then transfer to the PVSK layer through thermal conduction. Therefore, the IR annealing approach is similar to the traditional hot-plate thermal annealing, as they both anneal the PVSK layer with the thermal energy. On the other hand, the major output of

Xenon lamps is visible light, which will transmit through transparent precursor films, such as the MAI-PbI<sub>2</sub>-DMSO adduct<sup>[58]</sup>. This also leads to inefficient photonic annealing of the targeted PVK active layer.

It is believed that the key objective of thin-film annealing is to concentrate on a single layer while minimally affected other layers.<sup>[76]</sup> This will bring significant advantages, such as avoiding overheating and damage of underlying films. Such highly layer-selective annealing capabilities can never be realized by hot-plate thermal annealing since all stacking layers are heated up simultaneously. Likewise, layer-specific annealing has not been accomplished by photonic approaches using the above-mentioned light sources either. In order to fully realize the layer-specific potential of photonic treatments and break through the limitations of thermal annealing, a specialized light source with a carefully selected wavelength must be used to ensure that the vast majority of the photons generated by the light source will be absorbed and utilized by the PVK active layer. Light-emitting diodes (LEDs) are one such light source that can have an emission spectrum as narrow as 10 nm. When given the same amount of output power as the prior researches' lamps, LEDs have many more photons concentrated in a narrow spectrum, leading to much more efficient absorption and effective photonic treatment of the target layer. Different LEDs have their unique signature peak wavelengths in every range including ultraviolet (UV), visible and IR. The wavelength of LED irradiation can be specifically chosen to match the peak absorption of the target layer. The strong photonic absorption and exponential decay of light intensity in the aiming layer will have the energy supply concentrated on a single layer, leading to a highly-selective and layer-specific photonic treatment. Furthermore, as solid-state devices, LEDs are more

efficient for energy conversion from electricity to light than other kinds of lamps. As a result, the overall energy consumption in the mass production of PVSCs can be substantially reduced. In addition, LEDs have advantages like much better longevity and zero warm-up time, which makes LED light much cheaper and more reliable in the long run than other lamps, and suitable for pulsed irradiation as well.

## **CHAPTER 2. MODELLING OF SEGMENTED HIGH-PERFORMANCE THERMOELECTRIC GENERATORS WITH EFFECTS OF THERMAL RADIATION, ELECTRICAL AND THERMAL CONTACT RESISTANCES**

Although segmenting approach is lucrative, it inevitably gives rise to some new issues. One is that segmentation introduces new interfaces between TE materials in addition to leg-electrode interfaces. These interfaces host electrical and thermal contact resistances, which not only incur net losses, for example, extra Joule heat, but can also cause temperature redistribution in the TEG leg, offsetting the optimal temperature range for each TE materials, thereby reducing the overall efficiency and output power. The other issue is the pronounced thermal transfer loss, which includes thermal convection and radiation loss. When aiming at higher efficiency with segmented structure, higher temperature has to be involved, leading to a possibly much greater level of thermal convection and radiation losses. The convection loss can be eliminated by appropriate insulation, thus it is not considered in this study.<sup>[77]</sup> The radiation and contact losses deserve serious attention for a successful construction of segmented TEGs. Most of the contact-related studies focused only on the interfaces between the TE materials and the electrodes.<sup>[78-81]</sup> Even with the segmented structure, just a single TEG leg with only one interface between two TE materials was investigated.<sup>[82]</sup> None of them considers contact resistances from both segment-segment and segment-electrode interfaces. Furthermore, to the best of my knowledge, there is no simulation study on the effect of the thermal radiation loss.

In this chapter, more sophisticated geometries with up to 128 unicouples (16x16 =

256 legs) are adopted to build symmetrical and non-symmetrical TEG models. Manifold selection of TE materials, covering both the moderate ones and the best ones, are employed to fulfill the simulation. The thermal and electric properties of the TE materials are all temperature dependent, spanning a wide temperature range, extracted directly from the recently published experimental data. Moreover, the segmentation compatibility has been confirmed for the combination of the current best p-type and the strongest n-type TE materials. On the basis of TEG model with the optimized p-n leg ratio, thermal radiation and contact resistances have been taken into account. Both the electrical and thermal contact resistances at segment-segment and segment-electrode interfaces are examined. In addition, thermal radiation effect has also been explored with the radiation level from zero to perfect blackbody. The results demonstrate that the TEG performance experiences plateaus at lower contact resistance ranges, indicating that if interfaces could be well controlled, the contact effects would not have remarkable influence on the TEG performance. Overall speaking, the segmentation of the best p-type TE materials and strongest n-type TE materials up to date provides a promising route to achieve a high performance TEG. All the simulations in this study are implemented by using the 3D finite element analysis (FEA) solver ANSYS.

## 2.1 Method

### 2.1.1 Governing Equations

To get the insight of numerical simulation, I have first derived the analytical solution for one dimensional TEG problem, involving n pairs of thermocouples and an external load with resistance  $R_L$ . Each TEG thermocouple consists of one p element (leg) and one n

element. In the derivation, all the thermal transfer loss, electrical and thermal contact resistances are ignored. When the system arrives at a steady state, the power absorbed at the hot side of the TEG module and the power released at the cold junction can be expressed as following,<sup>[1, 32]</sup>

$$P_h = n \left[ I_e T_h \alpha - \frac{1}{2} I_e^2 R + K(T_h - T_c) \right] \quad (1)$$

$$P_c = n \left[ I_e T_c \alpha + \frac{1}{2} I_e^2 R + K(T_h - T_c) \right] \quad (2)$$

In both Equation (1) and (2), the first terms in the square brackets represent Peltier heat (power) generated, while the second and third terms denote Joule heat (power) and Fourier heat (power) transfer, respectively. The ratio 1/2 in front of the Joule term indicates that each of the hot junction and cold junction "consumes" half of the total created Joule heat, since the TEG module has the same number of p-type elements as n-type elements. The Seebeck coefficient  $\alpha$ , resistance of a thermocouple  $R$  (with  $\rho$  being the electrical resistivity), and thermal conductance  $K$  (with  $\kappa$  being the thermal conductivity) can be written more explicitly as

$$\alpha = (\alpha_p - \alpha_n) \quad (3)$$

$$R = \frac{\rho_p L}{A_p} + \frac{\rho_n L}{A_n} \quad (4)$$

$$K = \frac{1}{L} (\kappa_p A_p + \kappa_n A_n) \quad (5)$$

where the subscripts indicate p-type and n-type with  $L$  as the TEG leg length and  $A$  as the cross-section area of the TEG leg. As the difference between  $P_h$  and  $P_c$ , the output power of the system can also be expressed in terms of the current and the external load resistance  $R_L$ . In addition, the electrical current in the system equals the Seebeck emf divided by the total resistance (internal  $R$  plus external  $R_L$ ).

$$P_h - P_c = W = I_e^2 R_L \quad (6)$$

$$I_e = \frac{\alpha(T_h - T_c)}{R + R_L} \quad (7)$$

Combining Equation (1), (2), (6) and (7), the efficiency of the TEG module can be

represented as,

$$\eta = \frac{P_h - P_c}{P_h} = \eta_c \frac{\beta}{(1+\beta)+(1+\beta)^2 \cdot (ZT_h)^{-1} - \eta_c/2} \quad (8)$$

where  $\beta = \frac{R_L}{R}$ ,  $Z = \frac{\alpha^2}{RK} (= \frac{\alpha^2}{\rho\kappa})$  when referring to a single leg with sole TE material) and  $\eta_c = \frac{T_h - T_c}{T_h}$ . It can be shown that the maximum efficiency occurs at  $\beta = \frac{R_L}{R} = \sqrt{1 + Z\bar{T}}$ , where  $\bar{T}$

is the average of  $T_h$  and  $T_c$ .

$$\eta_{max} = \frac{T_h - T_c}{T_h} \left( \frac{\sqrt{1+Z\bar{T}} - 1}{\sqrt{1+Z\bar{T}} + \frac{T_c}{T_h}} \right) \quad (9)$$

Equation (9) indicates that  $\eta_{max}$  increases monotonically with  $Z\bar{T}$ . Once  $T_h$  and  $T_c$  have been chosen, the efficiency of the TEG module can be further optimized by maximizing  $Z$ . It is worth noting that all the above deductions are based on small temperature difference assumption:  $T_h - T_c = \Delta T \rightarrow 0$ . Under this prerequisite, the Seebeck coefficients, resistivities and thermal conductivities of both n and p-type semiconductors can be deemed as constants. As a result, it is not hard to verify that  $Z$  would reach its extreme value when the following relation is established.

$$\frac{A_n}{A_p} = \sqrt{\frac{\rho_n \kappa_p}{\rho_p \kappa_n}} \quad (10)$$

Generally speaking, a single TE material could be depicted by the dimensionless figure of merit  $ZT$ , defined as  $ZT = \alpha^2 T / \rho\kappa$ , and the optimal efficiency is still determined by Equation (9).

The 1D mathematical model presented above can only be used to get analytical solution under small temperature difference assumption:  $T_h - T_c = \Delta T \rightarrow 0$ , or in other

words, constant thermoelectric properties of the TE materials. However, when temperature-dependent TE properties are involved, only numerical solution could be obtained. In this study, the coupled thermoelectric equations used by the FEA solver are

$$\vec{q} = T\alpha\vec{J} + \kappa\vec{\nabla}T \quad (11)$$

$$\vec{J} = \sigma(\vec{E} + \alpha\vec{\nabla}T) = \frac{1}{\rho}(\vec{E} + \alpha\vec{\nabla}T) \quad (12)$$

where  $\vec{q}$  is the heat flux,  $\vec{J}$  is the electric current density,  $\alpha$  is the Seebeck coefficient,  $\sigma$  ( $\rho$ ) is the electrical conductivity (resistivity),  $\kappa$  is the thermal conductivity,  $\vec{E}$  is the electric field and  $T$  is the absolute temperature.

## 2.1.2 Material Properties

From a wide selection of TE materials, I choose the best p-type TE materials so far, covering different temperature ranges, from  $\text{Bi}_2\text{Te}_3$  alloy for room temperature, to  $\text{MgAgSb}$  for mid-temperature, and to  $\text{PbTeS}$  and  $\text{SnSe}$  for high-temperature application. On the other hand, three distinctive n-type material combinations are used for comparison and conclusion without loss of generality. **Table 1** shows a detailed temperature dependence of  $ZTs$  and Seebeck coefficients of those TE materials used in this study. It is worth mentioning that  $ZTs$  are used for choosing TE materials but not input into the simulation. The thermoelectric properties that are input directly into the simulation, except Seebeck coefficients, are electrical resistivities and thermal conductivities, which are all temperature dependent and listed in **Table 2**. Under the p-type and n-type 1 categories are the TE materials with the best performance to date. In addition, copper is used for electrodes. Its thermoelectric properties

are also temperature dependent as shown in **Table 3**. Through all the simulations, the cold side temperature of the TEG models is set to 300 K (room temperature), while the hot side temperature is chosen to be 500K, 800K and 1000 K. **Figure 1** illustrates the segmented TEG unicouple with three p-type materials and two n-type materials, and the TEG legs are connected thermally in parallel but electrically in series. In this study, more or less TE materials are chosen for both p-type and n-type legs based on the temperature difference between the hot side and the cold side.

**Table 1.** Temperature dependence of  $ZTs$  and Seebeck coefficients for used TE materials.

	p-type		n-type 1		n-type 2		n-type 3	
	300-400K BiSbTe <sup>[13]</sup>		300-400K CuBiTeSe <sup>[28]</sup>		YbCoSb <sup>[83]</sup>		Pb(S,Se,Te) <sup>[84]</sup>	
	450-500K MgAgSb <sup>[14]</sup>		450-800K AgPbSbTe <sup>[29]</sup>					
	550-800K KPbTeS <sup>[15]</sup>		850-1000K SiGe <sup>[31]</sup>					
	850-1000K SnSe <sup>[16]</sup>							
$T$ (K)	$ZT$	$\alpha(\mu V)$	$ZT$	$\alpha(\mu V)$	$ZT$	$\alpha(\mu V)$	$ZT$	$\alpha(\mu V)$
300	1.38	210	1.04	-186	0.38	-122	0.07	-50
350	1.47	220	1.06	-192	0.45	-128	0.12	-60
400	1.49	230	1.09	-194	0.55	-138	0.20	-75
450	1.36	233	1.06	-220	0.65	-143	0.29	-90
500	1.38	220	1.18	-245	0.75	-151	0.40	-108
550	1.56	235	1.34	-270	0.88	-158	0.53	-123
600	1.80	263	1.43	-305	1.00	-166	0.66	-140
650	1.95	283	1.64	-330	1.09	-173	0.79	-158
700	2.05	303	1.73	-350	1.18	-179	0.90	-175
750	2.18	308	1.94	-360	1.25	-183	0.95	-192
800	2.20	308	2.10	-375	1.33	-187	1.01	-205
850	2.39	340	1.40	-288	N/A			
900	2.53	340	1.50	-290				
950	2.48	335	1.58	-290				
1000	2.31	330	1.66	-290				

**Table 2.** Temperature dependence of resistivities  $\rho$  ( $\times 10^{-5} \Omega \text{ m}$ ) and thermal conductivities  $\kappa$  ( $\text{W m}^{-1} \text{ K}^{-1}$ ) for the used TE materials.

	p-type		n-type 1		n-type 2		n-type 3	
	300-400K BiSbTe <sup>[13]</sup>		300-400K CuBiTeSe <sup>[28]</sup>		YbCoSb <sup>[83]</sup>		Pb(S,Se,Te) <sup>[84]</sup>	
$T (\text{K})$	$\rho$	$\kappa$	$\rho$	$\kappa$	$\rho$	$\kappa$	$\rho$	$\kappa$
300	0.80	1.20	1.00	1.00	0.420	2.8	0.49	2.18
350	1.05	1.10	1.20	1.01	0.455	2.8	0.56	1.88
400	1.35	1.05	1.30	1.06	0.495	2.8	0.67	1.67
450	2.40	0.75	1.33	1.55	0.506	2.8	0.84	1.50
500	2.20	0.80	1.75	1.45	0.543	2.8	1.06	1.37
550	2.75	0.71	2.22	1.35	0.557	2.8	1.25	1.25
600	3.60	0.64	3.13	1.25	0.580	2.85	1.55	1.15
650	4.45	0.60	3.70	1.17	0.615	2.90	1.90	1.08
700	5.31	0.59	4.50	1.1	0.644	2.95	2.38	1.00
750	5.53	0.59	4.76	1.05	0.659	3.05	3.00	0.97
800	5.75	0.60	5.10	1.05	0.679	3.10	3.50	0.95
850	11.8	0.35	6.3	0.8	N/A			
900	11.8	0.35	6.3	0.8				
950	12.7	0.34	6.1	0.83				
1000	14.3	0.33	5.9	0.86				

**Table 3.** Temperature dependence of resistivity ( $\Omega \text{ m}$ ) and thermal conductivity ( $\text{W m}^{-1} \text{ K}^{-1}$ ) for copper contacts.

$T (\text{K})$	Resistivity	Thermal conductivity
300	1.73E-08	397
500	3.02E-08	388
800	4.97E-08	370
1000	6.26E-08	357

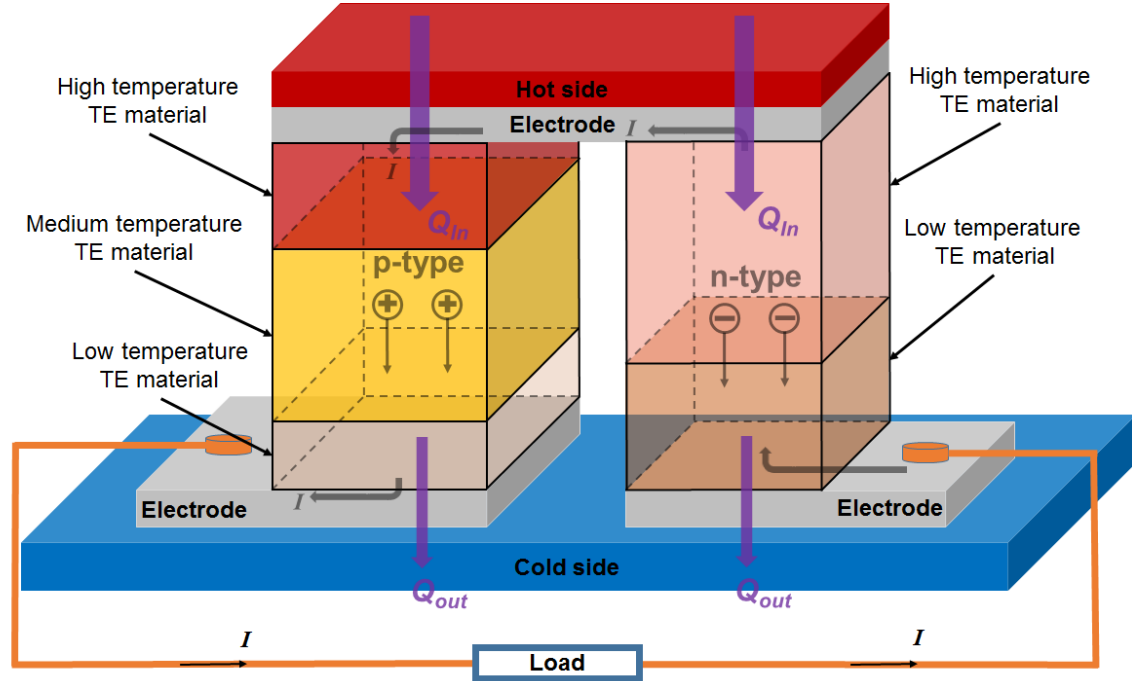


**Figure 1.** A schematic TEG model with segmented legs.

### 2.1.3 TEG Leg Geometries

The performance of TEGs with various leg geometries has been investigated to study the possibility of segmenting different TE materials to form a high-efficiency TEG device. The TEG models are divided into two categories: symmetrical models, i.e. p-type and n-type legs sharing the same geometry, and non-symmetrical models, in which p-leg and n-leg have different cross-sectional area as shown in **Figure 2**. All the symmetrical models are built with an overall active cross-section area of  $1474.56 \text{ mm}^2$  (the summation of the cross-section area of all the TEG legs). Total leg numbers varies from 16 ( $4 \times 4$ ), 64 ( $8 \times 8$ ), 144 ( $12 \times 12$ ) to 256 ( $16 \times 16$ ), which correspond to single leg dimensions (either p- or n-type) of  $9.6 \text{ mm} \times 9.6 \text{ mm}$ ,  $4.8 \text{ mm} \times 4.8 \text{ mm}$ ,  $3.2 \text{ mm} \times 3.2 \text{ mm}$  and  $2.4 \text{ mm} \times 2.4 \text{ mm}$ , respectively. Four different leg thicknesses are utilized, including 3 mm, 10 mm, 15 mm and 20 mm.

In modelling non-symmetrical leg geometries, the cross-sectional area of one type of legs is fixed, while the dimensions of the other type of legs change. Therefore this category can be further classified into two groups: group 1 with fixed p-type leg dimension of 9.6 mm  $\times$  9.6 mm, while n-type legs adopt cross-sections from 2.4 mm  $\times$  2.4 mm to 8.4 mm  $\times$  8.4 mm; group 2 with n-type legs set at 9.6 mm  $\times$  9.6 mm and p-type legs ranging from 2.4 mm  $\times$  2.4 mm to 8.4 mm  $\times$  8.4 mm. These non-symmetrical models have 2  $\times$  2 legs and share the same leg length of 10 mm. The non-symmetrical geometries used in the simulation are listed in **Table 4**. The symmetrical dimensions with  $A_p = A_n = 9.6 \text{ mm} \times 9.6 \text{ mm}$  are also included in the table for comparison.

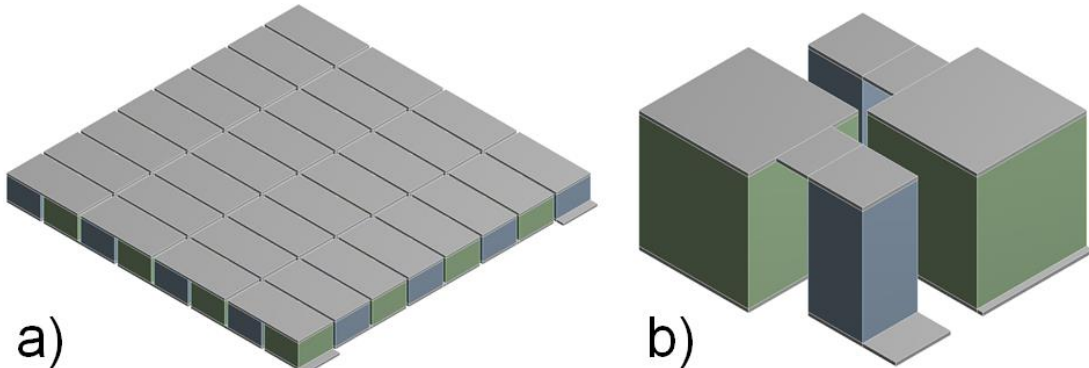


**Figure 2.** Illustration of a) symmetrical model with 8  $\times$  8 legs, and b) non-symmetrical model with 2  $\times$  2 legs used in simulation.

**Table 4.** Dimensions of non-symmetrical models.

Non-symmetrical models (L=10 mm, 2x2 legs)		
Group 1 ( $A_p > A_n$ )	Group 2 ( $A_p < A_n$ )	Total cross-section area (mm <sup>2</sup> )
$A_p=9.6 \times 9.6 \text{ mm}^2$	$A_n=9.6 \times 9.6 \text{ mm}^2$	
$A_n(\text{mm}^2)$	$A_p(\text{mm}^2)$	
2.4×2.4	2.4×2.4	195.84
3.6×3.6	3.6×3.6	210.24
4.8×4.8	4.8×4.8	230.4
6.0×6.0	6.0×6.0	256.32
7.2×7.2	7.2×7.2	288
8.4×8.4	8.4×8.4	325.44
9.6×9.6	9.6×9.6	368.64

## 2.2 Results and Discussion

### 2.2.1 Symmetrical Models

In modelling symmetrical TEG modules, the state-of-the-art p-type materials BiSbTe, MgAgSb, PbTeS and SnSe are combined for p-type legs, and identical resistivities, thermal conductivities, and Seebeck coefficients flipped to negative values are used for n-leg modelling. For a temperature difference of  $\Delta T=200\text{K}$  ( $300\text{K} \sim 500\text{K}$ ), TEG legs are segmented with BiSbTe and MgAgSb. In such temperature gradient, the two material segments are enough to ensure a uniformly high  $ZT$  across the legs. Since no single TE material is able to keep a  $ZT$  greater than unity over a large temperature range, as the  $\Delta T$  increases, more TE materials are required to advance thermoelectric energy conversion over large temperature difference. Thus the third and fourth layers of TE materials are added to TEGs for  $\Delta T=500\text{K}$  and  $700\text{K}$ .

**Figure 3a & 3b** show simulation results of thermoelectric energy-conversion efficiency as the total number of TEG legs and leg thickness vary. This efficiency from

symmetrical modelling is actually the so-called leg efficiency since only the properties of p-type materials are used. Neither the TEG leg thickness nor the total number of TEG legs has any significant influence on the efficiency of the TE modules. This conclusion verifies the 1-D analytical result in Equation (9) that there is no explicit term related to geometric factors, such as the total number of TEG legs and leg thickness. With adopted segmentation of TE materials, the leg efficiency of the TE modules depends heavily on temperature difference between the hot side and the cold end. For  $\Delta T=200K$ ,  $500K$  and  $700K$ , the TEG leg efficiencies are around 10.0%, 18.6% and 24.7%, respectively. These results approximate the theoretical upper limits, indicating that these materials are compatible as the segmentation follows a certain sequence.<sup>[36, 38, 41]</sup>

In addition to the efficiency, the heat absorption and output power were also studied for the symmetrical models. **Figure 3c** shows heat absorption rates at the TEG hot side as a function of leg thickness for various temperature differences. For any given temperature difference, as the TEG leg thickness increases, the required heat absorption decreases. The underlying principle is straightforward: a longer TEG leg is more difficult for heat to pass through, and thus easier for the TEG hot side to accumulate heat. As a result, less input heat power is required to reach or maintain the same temperature difference. From another perspective, if the input heat flux is constant, for instance, the exhaust heat from an engine, a longer leg length will create a greater temperature difference, thus leading to higher efficiencies. As demonstrated in **Figure 3c**, for TEGs with leg thickness of ~ 6mm, 10mm and 13mm, an input heat power of 100W can produce a temperature gradient of 200K (point A), 500K (B) and 700K (C), respectively.

**Figure 3d** shows that the output power barely experiences any change as the total number of TEG legs varies. As the total number of TEG legs increases, more pairs of p and n legs are connected in series, resulting in enhanced output voltage but reduced output current, keeping the output power almost the same. In practice, the number of TEG legs will mainly be determined by the load resistance, since the maximum efficiency and the maximal output power occur at  $\frac{R_L}{R} = \sqrt{1 + ZT}$  and  $\frac{R_L}{R} = 1$ , respectively. In other words, a larger load resistance requires a greater internal resistance of the TEG. For a given available surface area of a heat source, a high-performance TEG module can be achieved by shrinking down the cross-section area of individual leg thereby building more TEG legs.

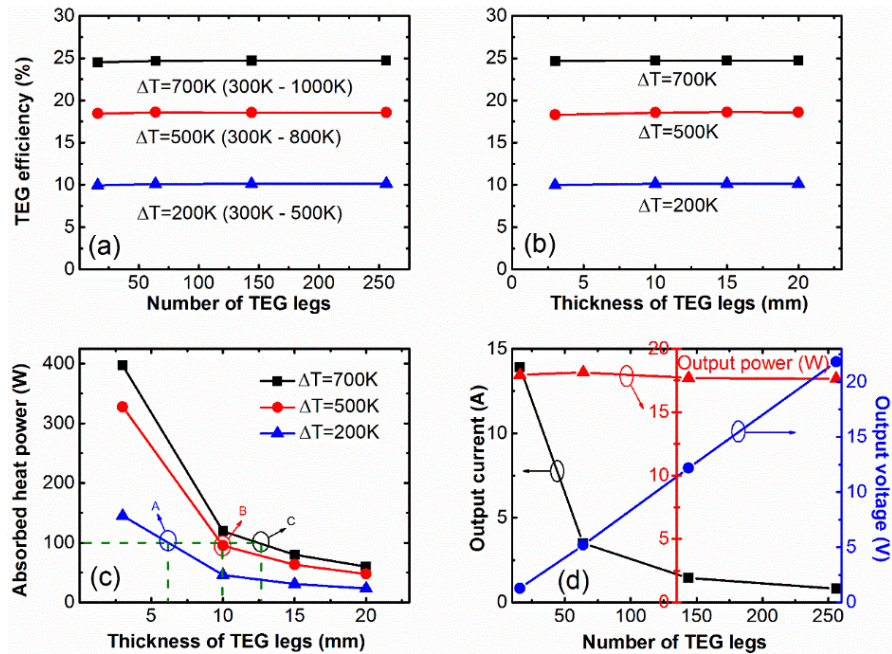


**Figure 3.** a) Efficiency of thermoelectric modules versus total number of TEG legs. The leg thickness is set to be 10 mm. b) Efficiency versus thickness of TEG legs, which is based on 256 (16 x 16) total number of TEG legs. c) The required heat power versus leg thickness with various temperature differences. d) Effects of number of TEG legs on output current, output voltage and output power. The temperature difference  $\Delta T = 500K$ , and leg thickness L= 10 mm.

## 2.2.2 Non-symmetrical Models

Non-symmetrical TEGs are modelled using the same p-type materials with three different combinations of n-type materials as listed in **Table 1**. Three temperature differences,  $\Delta T=200\text{K}$ ,  $\Delta T=500\text{K}$  and  $\Delta T=700\text{K}$ , are used in the simulation. The combination of the best p-type TE materials with the strongest n-type TE materials could yield an efficiencies of up to 17.0% and 20.9% at  $\Delta T = 500 \text{ K}$  and  $\Delta T = 700 \text{ K}$ , respectively. The simulation results also show that the maximum efficiencies are achieved by non-symmetrical TEGs for all three combinations (shown in **Figure 4a, 4b & 4c**), given that p-type and n-type materials are not the same. Since the n-type materials are universally weaker compared to their p-type counterparts, the peak performance of the TEG modules emerges when the p-type legs have larger cross-sectional area than the n-type legs. Similar to efficiency, the relationship  $A_n < A_p$  is also necessary for the maximum output power per unit area, which is in good agreement with a previous study.<sup>[43]</sup> In addition, the output power densities can reach and exceed  $2.1 \text{ Watt cm}^{-2}$  at optimal geometrical ratio with a temperature difference of 700 K, as shown in **Figure 4d**. Even with  $\Delta T = 500 \text{ K}$ , the output power densities can far surpass  $1.0 \text{ Watt cm}^{-2}$ . This capability of generating high power density will have great impact on utilizing vehicles' exhaust heat. For example, assuming that an exhaust pipe with 1m length and 10 cm diameter is completely covered with the proposed TEG device, the output power can be more than 6 kW, given that the exhaust temperature is around 500 °C, As noticed from **Figure 4**, the maximum efficiency and peak output power do not concur at the same optimal geometrical ratio, since their triggering conditions are different:  $\frac{R_L}{R} = 1$  for the maximum output power, and  $\frac{R_L}{R} = \sqrt{1 + Z\bar{T}}$  for the peak efficiency. Moreover, since less cross-section

area of n-type legs is required for reaching peak performance, non-symmetrical models would need less TE materials as compared to the symmetrical model, especially when the leg thickness is large, therefore leading to an economical design.

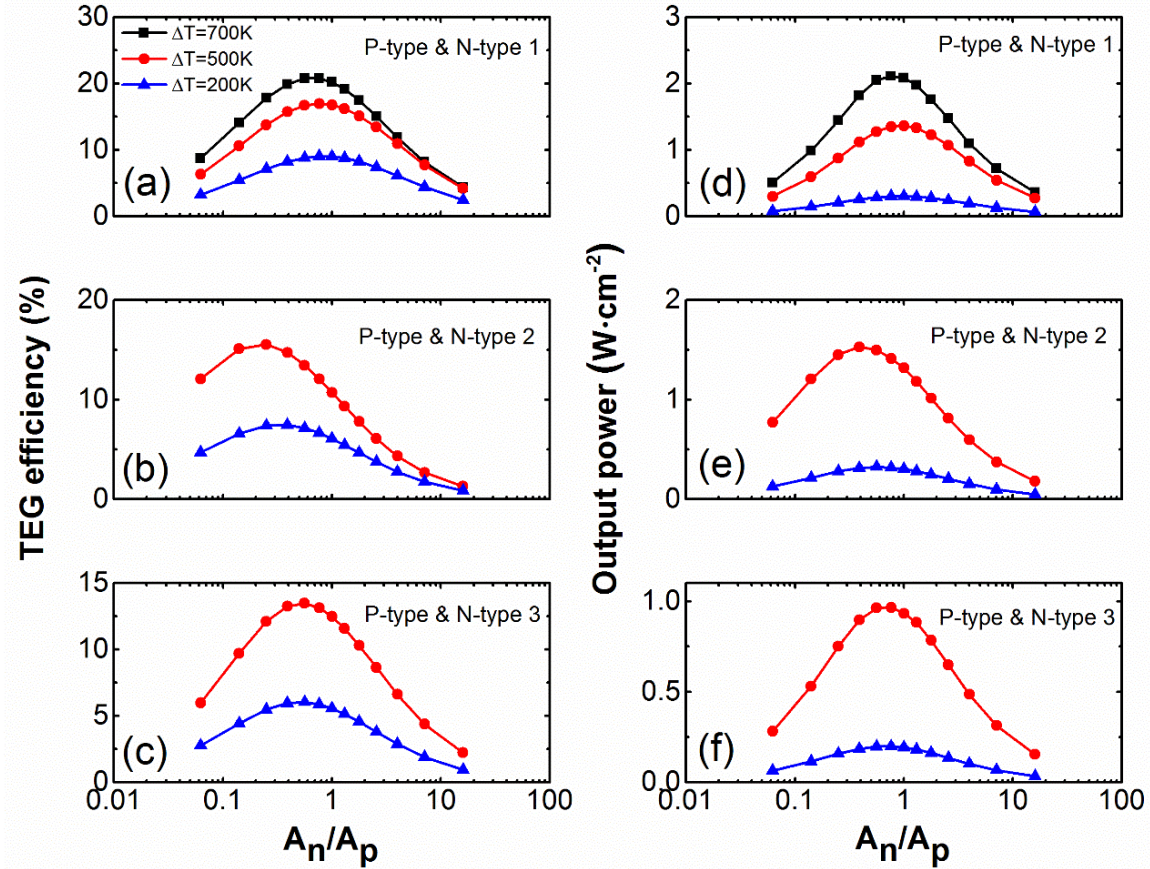


**Figure 4.** TEG efficiency (a, b & c) and output power per unit area (d, e & f) at different geometrical ratios. For all three TEG modules, the maximum efficiency is indeed achieved using non-symmetrical cross-section areas. The non-symmetrical TEG modules are built with the best p-type TE materials along with a) & d) n-type 1, b) & e) n-type 2, and c) & f) n-type 3 TE materials.

Nevertheless, above results indicate that the maximum efficiency and output power density are indeed achieved by non-symmetrical TEGs, given that p-type and n-type materials are not the same. This conclusion is supported by Equation (10), although it only

applies when temperature difference approaches zero ( $\Delta T \rightarrow 0$ ). To find the optimal cross-section ratio  $A_n/A_p$  at which the maximum efficiency could be achieved in a segmented leg structure, the Equation (10) that associates the extensive quantity (cross-section area  $A_n$  and  $A_p$ ) with the intensive properties of materials (electrical resistivity  $\rho$  and thermal conductivity  $\kappa$ ) has to be modified,

$$\frac{A_n}{A_p} = \sqrt{\frac{\rho_n(T) \cdot \kappa_p(T)}{\rho_p(T) \cdot \kappa_n(T)}} = \left( \int_{T_c}^{T_h} \sqrt{\frac{\rho_n(T) \cdot \kappa_p(T)}{\rho_p(T) \cdot \kappa_n(T)}} dT \right) / (T_h - T_c) \quad (13)$$

where  $\sqrt{\frac{\rho_n(T) \cdot \kappa_p(T)}{\rho_p(T) \cdot \kappa_n(T)}}$  is the average over temperature range from  $T_c$  to  $T_h$ . If  $\rho(T)$  and  $\kappa(T)$  of the TE materials are known in the operating temperature range, Equation (13) can be used to accurately calculate the optimal TEG leg geometries. However, in reality  $\rho(T)$  and  $\kappa(T)$  are typically discrete values obtained from the experiment. As a consequence, the integrations in Equation (13) should be replaced by summation, such as

$$\frac{A_n}{A_p} = \sqrt{\frac{\rho_n(T) \cdot \kappa_p(T)}{\rho_p(T) \cdot \kappa_n(T)}} = \left( \sum_{T_c}^{T_h} \sqrt{\frac{\rho_n(T) \cdot \kappa_p(T)}{\rho_p(T) \cdot \kappa_n(T)}} \Delta T \right) / (T_h - T_c) \quad (14)$$

In this work, a temperature interval of  $\Delta T = 50 K$  is adopted, alike most of the TE-related publications. **Table 5** compares the optimal geometrical ratios  $A_n/A_p$  between 3D simulation and estimation from Equation (14). The ratios from calculation and simulation match well with deviation less than 10%, which confirms the feasibility of the proposed Equation (14) for TEGs with segmented legs. To reach the highest TEG efficiency with given material combination, Equation (14) can be utilized to estimate the optimal geometrical ratio of TEG legs before conducting the simulation for guiding experiment.

**Table 5.** Comparison of optimal  $A_n/A_p$  ratios between 3D simulation and estimation from Equation (14).

Temperature range	300K - 500K			300K - 800K			300K - 1000K
	1	2	3	1	2	3	
N-type	1	2	3	1	2	3	1
Optimal ratio from simulation	0.90	0.36	0.56	0.77	0.25	0.56	0.66
Optimal ratio from Eq. (14)	0.89	0.35	0.52	0.76	0.25	0.52	0.68
Difference	-1.1%	-2.8%	-7.1%	-1.3%	0.0%	-7.1%	3.0%

### 2.2.3 Compatibility of Segmented TE Materials

From the simulation, the combination of the current best p-type and the present strongest n-type TE materials can yield efficiencies of up to 9.0%, 17.0% and 20.9% respectively with temperature differences of 200K, 500K and 700K, as shown in **Figure 5a**. These efficiencies are close to the theoretical upper limits of TE materials with  $ZT=2$  as exhibited in the inset of **Figure 5a** (deduced from Equation (9)), indicating that these TE materials are compatible and suitable to form segmented TE legs. According to the definition of the compatibility factor from Snyder et al.,  $s(T) = \frac{\sqrt{1+ZT}-1}{\alpha T}$ , any two TE materials with  $s$  values differing by a factor of 2 or more could not be connected to yield an effective segmentation.<sup>[38]</sup> Notice that  $s$  is temperature dependent and thus not unique for any TE material in its working temperature range. Based on  $ZT$  values and Seebeck coefficients in **Table 1**, the compatibility factors of the best p-type and n-type TE materials used in the simulation have been estimated, as exhibited in **Figure 5b & 5c**, respectively. Although p-type SnSe doesn't match directly with  $(Bi,Sb)_2Te_3/MgAgSb$ , since their compatibility factors differed by more than a factor of 2, however, the intermediate  $PbTe_{0.7}S_{0.3}$  segment has appropriate  $s$  values that are close to those of SnSe and  $(Bi,Sb)_2Te_3/MgAgSb$  at the overlapping temperatures. Besides,  $PbTe_{0.7}S_{0.3}$  is self-compatible<sup>[38]</sup> in its own operating

temperature range, i.e., its  $s$  value experiences only a mild variation (less than a factor of 2) in this temperature range. Therefore, the compatibility factor of the entire p-leg transformed smoothly from 300K to 1000K. The similar smooth transition of  $s$  value can also be observed for n-type TE materials in **Figure 5c**. This suave evolution of compatibility factor guarantees a successful segmentation even if the  $s$  values at the two ends (cold side and hot side) differ by more than a factor of 2.

Figure of merit  $ZT$  is typically the first property to look at when choosing TE materials for segmentation purpose. The second most important parameter for segmentation, the compatibility factor, should also be given enough attention. As demonstrated in the **Figure 6**, only high  $ZT$  will not ensure high efficiency. Figure S2a shows that the addition of a layer BaLaYbCo<sub>4</sub>Sb<sub>12</sub>, which has the highest  $ZT$  value of 1.66 around 850 K, reduces the optimal TEG efficiency instead of increasing it. **Figure 6b** clearly illustrated that  $s$  values of BaLaYbCo<sub>4</sub>Sb<sub>12</sub> do not match well with compatibility factors of other segmented materials. This result verifies that compatibility factor cannot be ignored when segmenting different TE materials. In summary, when taking a TE material for segmentation, not only  $ZT$  value but also compatibility factor have to be examined. A smooth change of  $s$  value from one end of the TEG leg to the other is needed for a successful segmentation of different high- $ZT$  TE materials, even if the change in  $s$  is more than a factor of 2 from the cold side to the hot side. Besides, each segmented TE material should have its own  $s$  value varying less than a factor of 2 in its operating temperature range.

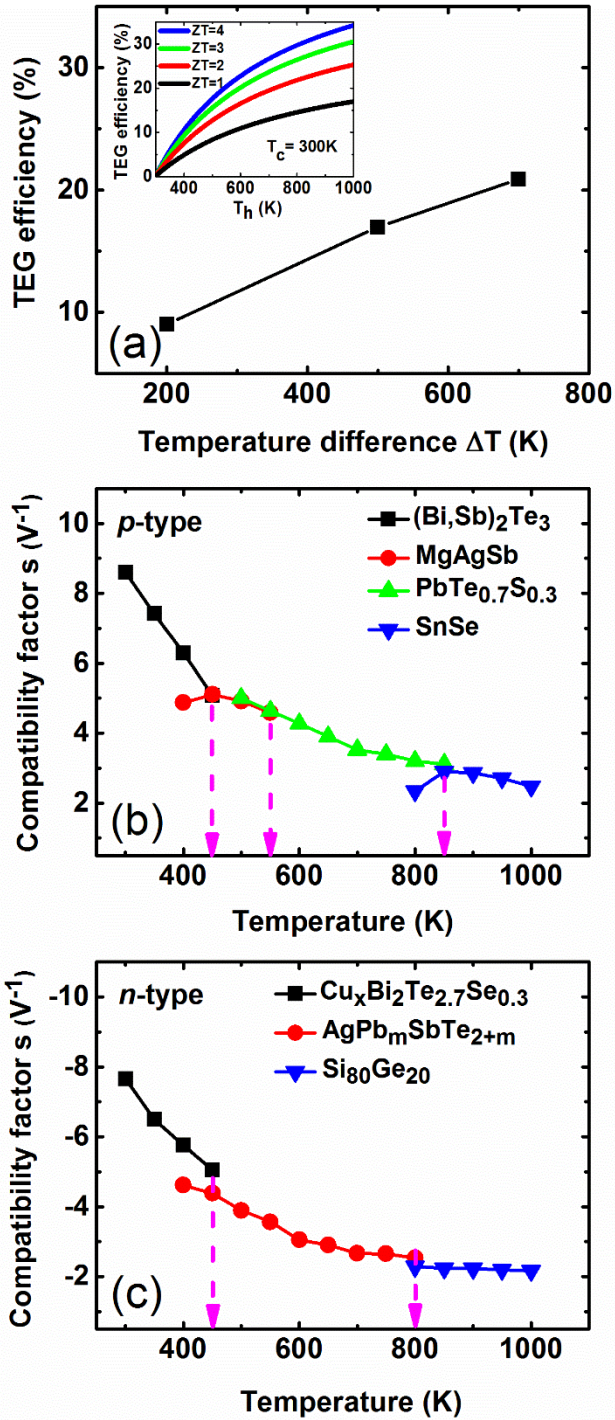


**Figure 5.** a) TEG Efficiency vs. temperature differences for TEGs with the combination of the current best p-type and the present strongest n-type TE materials (inset: TEG efficiency vs. hot side temperature at different  $ZT$  values, where cold side temperature has been set to 300K). b) & c) Compatibility factors of the series of best p-type and strongest n-type TE materials, respectively. The dashed lines indicate the interfaces between segments.

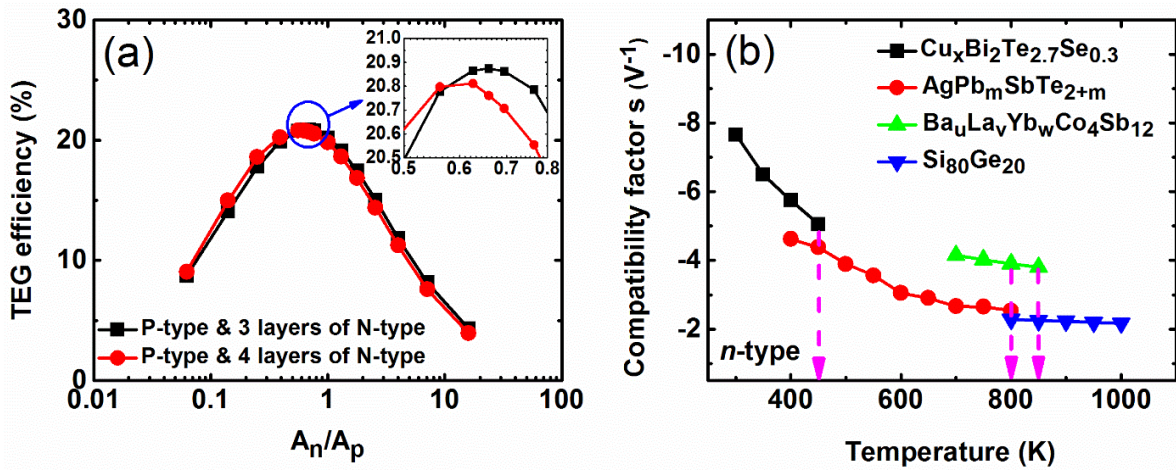


**Figure 6.** a) TEG Efficiency vs. geometrical ratios of the best p-type teaming with 3 or 4 layers of the strongest n-type TE materials @  $\Delta T = 700$  K. b) Compatibility factors of the BaLaYbCo<sub>4</sub>Sb<sub>12</sub> layer in comparison with the other three layers.

## 2.2.4 Thicknesses of Individual Segments

The simulation results can also be used to guide the fabrication of the TEG devices.

**Figure 7** shows the temperature distribution in a non-symmetrical TEG module with cold side at 300K and hot side at 1000K, from which the thickness of different TE materials in the leg can be determined based on their optimal temperature ranges. If the TEG leg length changes and the temperatures of both the hot side and cold end remain the same, the thickness of each individual layer can still be estimated based on the relative thickness percentages of the respective TE materials from the numerical simulation while maintaining the TEG efficiency.

For the TEG model with the optimized leg geometry, i.e. 9.6 mm  $\times$  9.6 mm for p-legs and 7.8 mm  $\times$  7.8 mm for n-legs, of the best TE materials' combination, thermal radiation, electrical and thermal contact resistances have been added as boundary conditions. The four

segmented p-type TE materials and three n-type TE materials introduce 9 interfaces per unicouple, including 5 segment-segment and 4 segment-electrode interfaces.

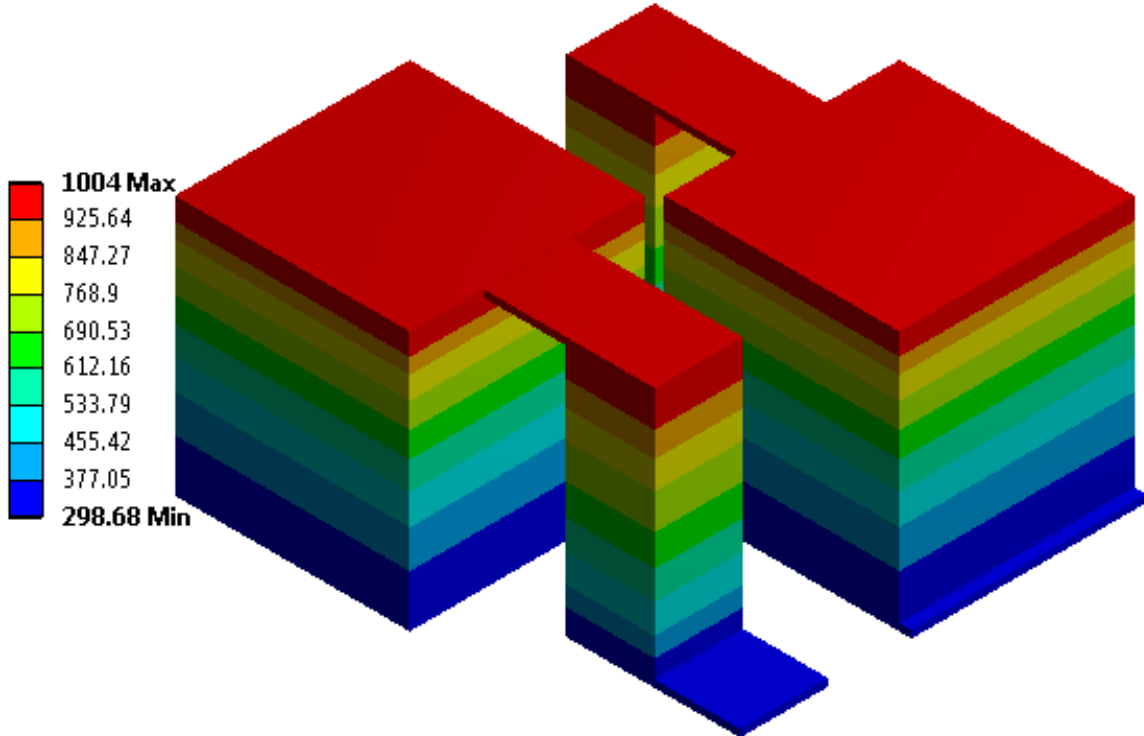


**Figure 7.** Temperature distribution in a 3D non-symmetrical TEG module,  $A_n/A_p = 0.141$ , with the best p-type TE materials and 3 layers of the strongest n-type TE materials.

## 2.2.5 Thermal Radiation Loss

In modelling thermal radiation loss, emissivity from 0 to 1 are adopted, which corresponds to zero radiation loss and total black body radiation, respectively. **Figure 8** shows that TEG efficiency decreases monotonically with the increase of the emissivity. With the highest level of radiation loss, the TEG efficiency falls to around 16.3%, which is still much higher than the efficiency of the currently state-of-the-art TEGs. The output power

density stays nearly the same, which is due to the gain of the input heat power density for keeping the preset end temperatures of the TEG module. Although not exhibited here, the thermal radiation of any level does not have a noticeable effect on the temperature distribution of the TEG module, therefore it is not necessary to optimize the thicknesses of individual segmentations through iteration to obtain the best performance. It is worth mentioning that in my simulation the radiation is net loss without considering the reabsorption by the adjacent TEG leg faces. With reabsorption, the TEG efficiency could be slightly higher than that shown in **Figure 8** but will not exceed the point at zero emissivity. According to Stefan-Boltzmann Law and Second Law of Thermodynamics, a good emitter is also a good absorber and vice versa. If the emissivity is low, then the reabsorption will be weak and have little influence on the TEG performance. In the contrary, at high emissivity, the reabsorption will be strong, but it could never overturn the massive loss induced by the high level of radiation. Therefore, here I only consider thermal radiation as net loss to obtain the ultimate values.

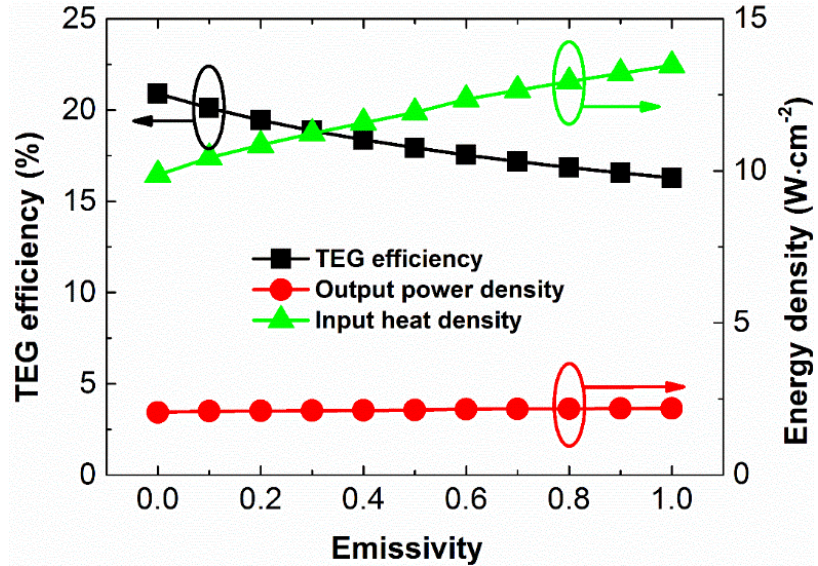


**Figure 8.** TEG efficiency, output power density and input heat density vs. emissivity/thermal radiation.

## 2.2.6 Contact Resistances

In this study, electrical and thermal contact resistances at both segment-segment and leg-copper interfaces have been considered. The electrical contact resistance has been reported to have typical values falling in the range of  $1 \times 10^{-9} - 1 \times 10^{-7} \Omega \cdot m^2$ .<sup>[85]</sup> **Figure 9a & 9b** shows the influence of such electrical contact resistance on the TEG efficiency and output power density. As anticipated, when the electrical contact resistance increases, both efficiency and out power decreases, although there exists a plateau for electrical contact resistance less than  $1 \times 10^{-8} \Omega \cdot m^2$ . With growing of the electrical contact resistance, the temperature distribution profile of the TEG legs is found to change accordingly. The thicknesses of each individual segmentation have been optimized iteratively to ensure that the physical interfaces match with the corresponding temperature distribution.

On the other hand, thermal contact resistance at interfaces varying in the range of  $1 \times 10^{-6} - 5 \times 10^{-4} m^2 \cdot K \cdot W^{-1}$  have been reported.<sup>[86]</sup> **Figure 9c & 9d** shows the thermal

contact resistance does not have significant effect on the efficiency and output power density at the values less than  $5 \times 10^{-4} \text{ m}^2 \cdot \text{K} \cdot \text{W}^{-1}$ , only beyond which the performance of the TEG module degrades rapidly. Similar to the influence from electrical contact resistance, as the thermal contact resistance increases, the temperature distribution profile also changes accordingly. The thicknesses have to be optimized iteratively to achieve the temperature distribution coincidental with the physical interfaces.

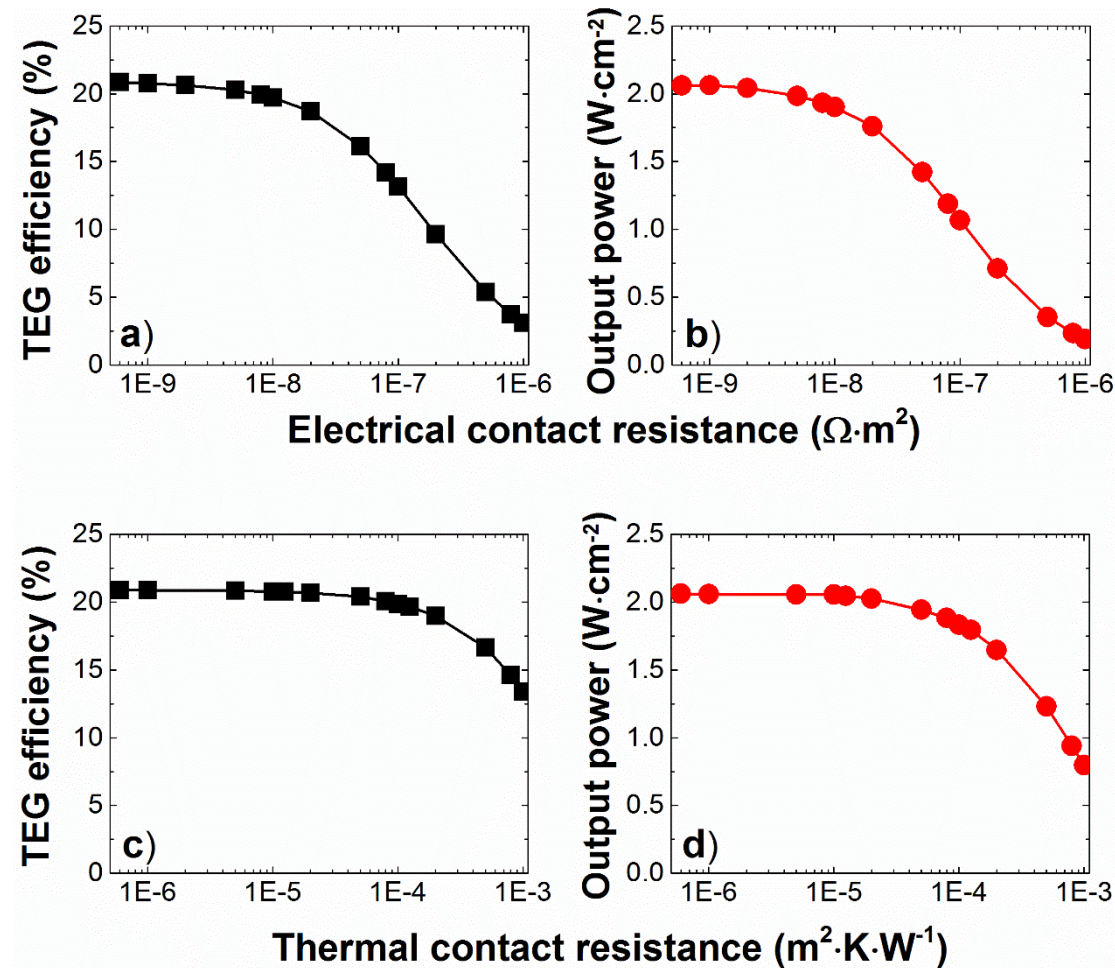


**Figure 9.** a) TEG efficiency and b) output power density vs. electrical contact resistance. c) TEG efficiency and d) output power density vs. thermal contact resistance.

### **CHAPTER 3. DESIGN OF SEGMENTED HIGH-PERFORMANCE THERMOELECTRIC GENERATORS WITH COST IN CONSIDERATION**

With prudent choice of compatible high-performance TE materials, segmented TEGs can be quite lucrative in terms of both efficiency and output power density. In the last chapter, I have shown that efficiency of over 20% and aerial power density over 2 Watt cm<sup>-2</sup> are possible at the temperature difference of 700 K, taking into account the effects of electrical and thermal contact resistances as well as the thermal radiation.<sup>[87]</sup> When choosing candidates for segmentation, compatibility is as important as high *ZT*. Although great effort has been made to increase *ZT*, the progress has stagnated.<sup>[7, 88]</sup> A diverting part of the research passion in the field is to escalate the TE power factor, which can be simply viewed as the product of *ZT* and the thermal conductivity. TE materials with larger power factor are expected to produce greater output power without necessarily higher efficiency. Compared with high-*ZT* Chalcogenides and SiGe, Skutterudites (SKDs) and Half-Heuslers (HHs) are representative TE materials of superior power factors but moderate *ZTs*.<sup>[89-90]</sup> SKDs and HHs are also promising candidates for segmented TEGs. Ngan et al. used a customized 1D numerical model to estimate efficiencies of segmented TEGs with various combinations of TE materials, including HHs.<sup>[41]</sup> McEnaney et al. studied segmented model with Bi<sub>2</sub>Te<sub>3</sub> and SKDs.<sup>[39]</sup> Zhang et al. have successfully built bismuth telluride/SKDs segmented TE modules with a current highest efficiency of 12% at a temperature difference of 541 K, matching results of their theoretical simulation.<sup>[91]</sup> In fact, most of the research projects in the TE field focus on improving the thermoelectric properties of TE materials or performance of TEG

devices.

In reality, it is the cost-performance ratio rather than the high performance alone that will lead to the widespread employment of a technology. For example, photovoltaic (PV) cells have established their competence and taken large market share with their  $\sim 1$  dollar per watt ( $\$/\text{watt}^{-1}$ ) cost-effectiveness. TEGs should be judged with the same metrics in order to compete with other energy sources. Yee et al. have formulated an instructive method to apply the  $\$/\text{W}$  metrics to the TEG power generation.<sup>[92]</sup> In their ensuing work, cost-performance with optimal fill factors (active cross-sectional area of TEG to area of heat exchangers) and leg lengths of 30 different TE materials has been assessed on the level of a unicouple, *i.e.* one pair of n-leg and p-leg, assuming same magnitude of temperature-independent Seebeck coefficients, electrical conductivity and thermal conductivity for both n- and p-type legs.<sup>[93]</sup> Due to the strong temperature-dependence of these TE material properties and the possible differences between the n- and p- type legs, the more complicated numerical approaches such as finite element method (FEM) should be implemented to more accurately evaluate the TEG performance and associated cost-effectiveness. Rezania et al. have utilized finite element analysis solver ANSYS to appraise the power per price for a unicouple system consisting of  $\text{Zn}_4\text{Sb}_3$  as p-leg and  $\text{Mg}_2\text{Si}_{1-x}\text{Sn}_x$  as n-leg, but their analysis does not take the cost-contribution from the heat exchanger system into account.<sup>[43]</sup> Kim et al. proposed a design with spacer inserted inside TE legs and claimed that the cost drop outpaces the reduction of the output power by performing ANSYS simulation.<sup>[94]</sup> Benday et al. analyzed the performance and economic possibility of 4 TE materials utilizing ANSYS modelling, finding out that heat sources of higher temperature are desired for improvement of financial

feasibility of TEGs.<sup>[95]</sup> However, all of the above-mentioned cost-performance evaluations have not taken electrical and thermal resistances into account. More importantly, no work has been done on the cost-effectiveness of segmented TEG systems with compatible state-of-the-art TE materials to fully study their potential in practical applications.

In this chapter, I carefully select 10 high-performance TE materials, with 5 p-types and 5 n-types, in the category of Chalcogenides, SiGe alloy, Skutterudites and Half-Heuslers. The selecting criteria are based on an overall consideration of the TE materials for segmentation, including figure of merit ( $ZT$ ), compatibility factors and power factors. Two p-type and two n-type segmented TEG legs are formed by the selected TE materials to generate four combinations of TEG modules. Systematical modelling of these segmented TEG modules are carried out by the 3D finite element analysis (FEA) with ANSYS. All the thermoelectric properties of the TE materials are temperature dependent, spanning a temperature range from 300 K to 1000 K, extracted directly from the published experimental data.<sup>[13-16, 28-29, 31, 96-98]</sup> Contact effects at the TE-TE and TE-electrode interfaces have also been taken into account, including both the electrical and thermal contact resistances. Optimum cross-sectional area ratios ( $A_n/A_p$ ) of TEG n-leg to p-leg have been identified for the maximal device performance, by applying the type I boundary conditions (BCs), which are the fixed temperature at hot sides (1000 K) and cold sides (300 K) of the TEG modules. Based on the discovered cross-sectional area ratios, optimal TEG leg lengths for the best cost-performance ratio have been found by employing type II BCs with constant temperature at hot sides (1000 K) while altering the heat transfer coefficients of cold sides. The results show that the output power density of TEGs can be enhanced conditionally by SKDs and

HHs, indicating that TE materials with high power factors but relatively low  $ZTs$  might be preferred for applications in which cost is less important. When costs are taken into consideration, including materials, heat transfer and manufacturing cost, TE materials of higher  $ZTs$  demonstrate notable advantages over their counterparts with higher power factors. The successful segmentation of high- $ZT$  TE materials is able to offer a cost-performance ratio of  $\sim 0.86 \text{ \$ W}^{-1}$ , while maintaining an efficiency of 17.8% and delivering a power density of over  $3.0 \text{ Watt cm}^{-2}$ . On the other hand, segmented TE modules involving TE materials with larger power factors can only provide a cost-performance ratio of  $\sim 1.11 \text{ \$ W}^{-1}$ , corresponding efficiency of 16.2% and power density of  $\sim 2.4 \text{ Watt cm}^{-2}$ . These results confirm that  $ZT$  is indeed the top benchmark for selecting TE materials. More importantly, the low dollar-per-watt value along with the high efficiency and power density make it possible for segmented TEGs to be competitive with other renewable energy sources such as photovoltaic cells.

### 3.1 Method

#### 3.1.1 Governing Equations of TEG Physics

When the system arrives at a steady state, the heat flux  $\vec{q}$  ( $\text{W} \cdot \text{cm}^{-2}$ ) absorbed at the hot side of the TEG module and the current density  $\vec{J}$  ( $\text{A} \cdot \text{cm}^{-2}$ ) flows in the TEG legs can be expressed by equation (11) and (12) from Chapter 2 as follows,<sup>[32]</sup>

$$\vec{q} = T\alpha\vec{J} + \kappa\vec{\nabla}T \quad (11)$$

$$\vec{J} = \frac{1}{\rho}(\vec{E} + \alpha\vec{\nabla}T) \quad (12)$$

where  $\alpha$ ,  $\rho$ ,  $\kappa$ ,  $\vec{E}$  and  $T$  are the Seebeck coefficient, electrical resistivity, thermal

conductivity, electrical field and absolute temperature, respectively. The sign convention of each vectors are shown in **Figure 10**. Here a 1D denotation is used for the analytical deduction in a single p-type TEG leg, while the 3D form is used for couples of p-type and n-type TEG legs in the numerical simulation by ANSYS.

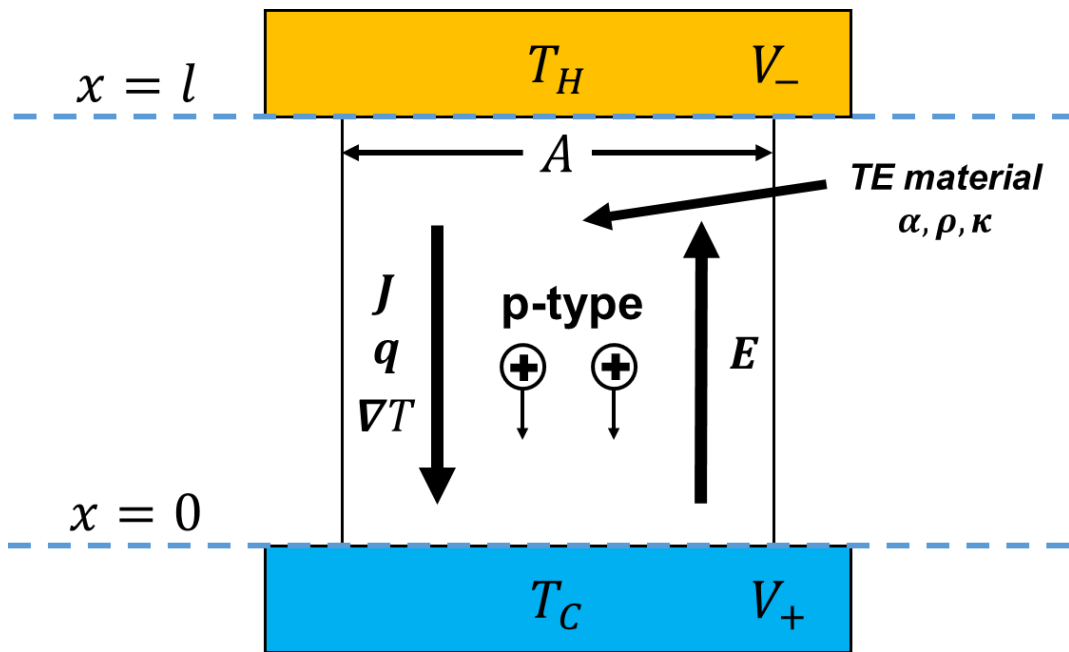


**Figure 10.** Schematic of the thermoelectric operation and parameter denotation.

Equation (11) shows that the total heat (power) absorbed equals Peltier heat (power) generated, plus Fourier heat (power) transferred. Equation (12) expresses a modified Ohm's law by taking Seebeck effect into account. Assuming  $T_H - T_C = \Delta T \rightarrow 0$ , equation (11) can be approximated by equation (15) and the overall efficiency of TEG can be denoted by equation (9) in Chapter 2.

$$q = \left( T_H \frac{\alpha^2}{\rho} + \kappa \right) \frac{\Delta T}{l} \quad (15)$$

$$\eta_{max} = \frac{T_H - T_C}{T_H} \left( \frac{\sqrt{1 + Z\bar{T}} - 1}{\sqrt{1 + Z\bar{T}} + \frac{T_C}{T_H}} \right) \quad (9)$$

In equation (15),  $l$  is the length of TEG leg and  $\alpha^2\rho^{-1}$  is the so-called TE power factor (P.F.) of the TE material. In equation (9),  $Z = \frac{\alpha^2}{\rho\kappa}$  and  $Z\bar{T}$  is the average figure of merit in the range between the hot-side temperature  $T_H$  and the cold-side temperature  $T_C$ . Equation (15) shows clearly that the heat flux at hot side is influenced by the power factor, thermal conductivity, temperature difference and the length of the TEG leg, without explicit dependence on the cross-sectional area. In order to maximize the efficiency in equation (9), two additional requirements need to be met, as indicated in formulas below.<sup>[1]</sup>

$$\beta = \frac{R_L}{R} = \sqrt{1 + Z\bar{T}} \quad (16)$$

$$\frac{A_n}{A_p} = \sqrt{\frac{\rho_n \kappa_p}{\rho_p \kappa_n}} \quad (10)$$

Equation (16) is the relation between the external load resistance  $R_L$  and the TEG inner resistance  $R$  that yields the highest efficiency, as compared with the relation  $R_L = R$ , which produces the maximum output power. In Chapter 2, I found that the following modification of equation (10) is convenient for estimating and choosing the initial cross-sectional area of the TEG legs before conducting actual simulation on segmented TEGs.<sup>[87]</sup>

$$\frac{A_n}{A_p} = \sqrt{\frac{\rho_n(T) \cdot \kappa_p(T)}{\rho_p(T) \cdot \kappa_n(T)}} = \left( \sum_{T_C}^{T_H} \sqrt{\frac{\rho_n(T) \cdot \kappa_p(T)}{\rho_p(T) \cdot \kappa_n(T)}} \Delta T \right) / (T_H - T_C) \quad (14)$$

### 3.1.2 Cost–performance Metrics

The cost-performance  $C.P.$  of a TEG can be defined as the ratio of the overnight capital cost  $C_{tot}$  to the power generation capability  $P$  of the TEG, expressed by equation

(17) with the unit of dollar per watt ( $\$ \text{W}^{-1}$ ).

$$C.P. = \frac{C_{tot}}{P} = \frac{\Omega_g D l A_{TE} + \Omega_{M,g} D l A_{TE} + \Omega_{M,A} A_{TE} + \Omega_{HX} h A_{HX}}{\eta A_{TE} q} \quad (17)$$

The overnight capital cost comprises i) the cost of TE materials, ii) manufacturing costs of the TE module and iii) the cost of heat exchangers on both sides. The cost of a TE material is the product of this material's gravimetric price  $\Omega_g$  ( $\$ \text{kg}^{-1}$ ), its density  $D$ , length  $l$  and cross-sectional area  $A_{TE}$ . Manufacturing costs are composed of the gravimetric manufacturing cost with a price of  $\Omega_{M,g}$  ( $\$ \text{kg}^{-1}$ ) and areal manufacturing cost with a price of  $\Omega_{M,A}$  ( $\$ \text{cm}^{-2}$ ). The former refers to the processing such as hot pressing, ball milling, etc., scaling with the weight of TE materials. The areal manufacturing cost involves processing like soldering, metallization, cutting and dicing, scaling with the active cross-sectional area of the TEG module. The cost of heat exchangers is the product of the unit price  $\Omega_{HX}$  ( $\$ \text{W}^{-1} \text{K}$ ), heat transfer coefficients  $h$  ( $\text{W m}^{-2} \text{K}^{-1}$ ) and the cross-sectional area  $A_{HX}$  of heat exchangers. The power generation capability  $P$  of the TEG is more straightforward, being the product of the TEG efficiency  $\eta$ , cross-sectional area  $A_{TE}$  and the heat flux  $q$  absorbed at the hot side. By utilizing expressions in equation (15) and defining the fill factor  $F = A_{TE}/A_{HX}$ , equation (17) can be simplified to equation (18), which is a quadratic equation of variable  $l$  since no other parameter has explicit dependence on the TEG leg length. This indicates that the TEG cost-performance ratio has a minimum at an optimal  $l$  value. Although equation (18) is for a TEG with a single leg, such a behavior is expected to be universal to any TEG module, including TEGs with multiple segmented p & n legs. In case of segmented TEGs, the cost for each individual TE materials is calculated first, then their contributions are summarized to the total cost.

$$C.P. = \frac{(\Omega_g + \Omega_{M,g})DFl^2 + (\Omega_{M,A}F + \Omega_{HX}h)l}{\eta F \left( T_H \frac{\alpha^2}{\rho} + \kappa \right) \Delta T} \quad (18)$$

$$(\Omega_g + \Omega_{M,g})_i D l A_{TE}$$

$$= A_p \sum_i (\Omega_g + \Omega_{M,g})_i D_{p,i} l_{p,i} + A_n \sum_j (\Omega_g + \Omega_{M,g})_j D_{n,j} l_{n,j} \quad (19)$$

As exhibited in equation (19), for example, the cost of  $i$ th p-type TE material equals the product of its collective price  $(\Omega_g + \Omega_{M,g})_i$ , density  $D_{p,i}$  length  $l_{p,i}$  and cross-sectional area  $A_p$  in the p-leg. It should be noted that the minimal cost-performance is calculated from equation (17) and (19) rather than equation (18), which is only deduced for theoretical analyzing purpose. The optimal leg length, output power and heat transfer coefficients are all obtained by simulation, while  $A_{TE}$ ,  $A_n$ ,  $A_p$  and  $A_{HX}$  will be discussed more in a later section. The densities and gravimetric prices of various TE materials<sup>[13-16, 28-29, 31, 96-98]</sup> are extracted from literatures and listed in **Table 6**.<sup>[93, 99]</sup> Some TE materials do not have exact prices published, therefore assuming the prices of the most similar ones will still yield a fairly accurate result. Meanwhile, the prices of manufacturing and heat exchangers are listed in

**Table 7.**<sup>[92-93, 100]</sup> Although being fabricated via different methods, all of 10 selected TE materials are bulk processed, and thus estimated to have the same fabricating price for simplicity, i.e., 2.4 \$ kg<sup>-1</sup> (ball milling + spark plasma sintering) for gravimetric manufacturing price and 1.68 × 10<sup>-2</sup> \$ cm<sup>-2</sup> for areal module price.<sup>[93]</sup> The segmentation of TE materials is usually achieved by soldering<sup>[101-102]</sup>, which will increase the total areal manufacturing cost. For example, one TEG leg with N segments of different TE materials will require N-1 times of soldering jobs in addition to the regular soldering/metallization of the electrodes. As a result, the areal cost for this segmented TEG leg approximately equals to

the product of the number N, the cross-section area of the leg and the areal manufacturing price. At present, the unit price of the heat exchangers is  $\sim 10 \text{ \$ W}^{-1} \text{ K}$  and dominates the total cost of the TEG system. However, current high prices can be significantly reduced by the large scale production and installation, providing a value of  $\sim 2.05 \text{ \$ W}^{-1} \text{ K}$  for the unit price of heat exchangers  $\Omega_{HX}$ , which contains prices of both heat exchangers and ceramic plates.<sup>[92]</sup> It is worth noting that any operating cost is excluded since the cost-performance ratio in this context is calculated as the overnight capital cost versus the TEG output power. Operating cost such as the circulation of cooling water is more appropriate for calculation of the \$ per kWh metrics and therefore is not in the scope of this study.

**Table 6.** Densities and prices of TE materials used in this study.<sup>[13-16, 28-29, 31, 93, 96-99]</sup>

Material name	Density $D$ (g cm <sup>-3</sup> )	Gravimetric material prices $\Omega_g$ (\$ kg <sup>-1</sup> )
(Bi,Sb) <sub>2</sub> Te <sub>3</sub>	6.4367	125.47
MgAgSb	6.2	114
PbTe <sub>0.7</sub> S <sub>0.3</sub>	7.07	83.81
SnSe	6.1	83.81
H-doped SnSe	6.1	83.81
CuxBi <sub>2</sub> Te <sub>2.7</sub> Se <sub>0.3</sub>	7.77	171
AgPb <sub>m</sub> SbTe <sub>2+m</sub>	9.27	83.81
Si <sub>80</sub> Ge <sub>20</sub>	2.8	371
Yb <sub>0.3</sub> Co <sub>4</sub> Sb <sub>12.2</sub>	7.48	64
Ti <sub>1-x</sub> Hf <sub>x</sub> NiSn <sub>1-y</sub> Sb <sub>y</sub>	9	166

**Table 7.** TEG manufacturing cost and heat exchanger prices used in this study.<sup>[92-93, 100]</sup>

Gravimetric manufacturing price $\Omega_{M,g}$ (\$ kg <sup>-1</sup> )	2.4
Areal manufacturing price $\Omega_{M,A}$ (\$ cm <sup>-2</sup> )	$1.68 \times 10^{-2}$
Heat exchanger price $\Omega_{HX}$ (\$ W <sup>-1</sup> K)	2.05* or 10

\* Possible price at large-scale production and installation.

### 3.1.3 Properties of Segmented TE Materials and Contact Resistances

My choice of TEG leg materials contains two general p-type groups and two general n-type groups. P-type 1 is the combination of current best p-type materials in terms of  $ZT$ , including  $(Bi,Sb)_2Te_3$ , MgAgSb,  $PbTe_{0.7}S_{0.3}$  and the un-doped SnSe for operating temperatures of  $300\text{ K} \sim 400\text{ K}$ ,  $450\text{ K} \sim 500\text{ K}$ ,  $550\text{ K} \sim 800\text{ K}$  and  $850\text{ K} \sim 1000\text{ K}$ , respectively.<sup>[13-16]</sup> P-type 2 is constructed by replacing  $(Bi,Sb)_2Te_3$ , MgAgSb and  $PbTe_{0.7}S_{0.3}$  in P-type 1 with the hole-doped SnSe.<sup>[96]</sup> For n-type 1 group,  $Cu_xBi_2Te_{2.7}Se_{0.3}$  are selected for low temperature,  $AgPb_mSbTe_{2+m}$  for medium temperature and  $Si_{80}Ge_{20}$  for high temperature ranges, representing the current best n-type combination in terms of  $ZT$ .<sup>[28-29, 31]</sup> The Yb-filled SKD ( $Yb_{0.3}Co_4Sb_{12.2}$ ) is teamed up with the  $Ti_{1-x}Hf_xNiSn_{1-y}Sb_y$  HHs to make up n-type 2 group, denoting the present top n-type combination in terms of power factors.<sup>[97-98]</sup> In total, four types of TEGs are constructed, including assemblies of “p-type 1 + n-type 1”, “p-type 1 + n-type 2”, “p-type 2 + n-type 1” and “p-type 2 + n-type 2”. The compatibility factors of the TE materials are calculated before selection to guarantee these TE materials would collaborate with each other in each group combination and leg construction, enhancing instead of adversely affecting the overall TEG performance. **Figure 11** shows a detailed  $ZT$  values of the chosen 10 TE materials at different working temperature ranges, including two p-type groups (a) and two n-type groups (b). **Figure 12a** and **12b** illustrate temperature dependence of the compatibility factors for all the chosen TE materials. The solid symbols represent type 1 TE materials, either p-type or n-type, while hollow symbols represent TE materials for type 2 collections of TE materials. It can be seen that the compatibility factors are in smooth transitions in the range of  $300\text{ K}$  to  $1000\text{ K}$  for both the two p-type and the two

n-type segmented legs. For example, the components of n-type 2, including Yb-SKD and the Half-Heuslers, have compatibility factors changing smoothly between  $-4 \text{ V}^{-1}$  and  $-2 \text{ V}^{-1}$  without any abrupt break. **Figure 12c** and **12d** show power factors of the selected TE materials versus temperature. The power factors of the p-type 2 is similar to that of the p-type 1, while the power factors of the n-type 2 is apparently much larger as compared to the n-type 1. It is worth pointing out that neither the figure of merits  $ZT$  nor the compatibility and power factors are entered in the simulation. However, TE properties like Seebeck coefficients, electrical resistivities and thermal conductivities are put directly into the simulation, all of which are also temperature dependent and extracted from respective literatures.<sup>[13-16, 28-29, 31, 96-98]</sup> Copper is adopted for electrodes, whose thermal and electric properties varies with temperature as well and can be found in **Table 3** from Chapter 2.<sup>[87]</sup> The ceramic substrates that sandwich the TE modules assume standard alumina ( $\text{Al}_2\text{O}_3$ ) with thermal conductivity of  $30 \text{ W m}^{-1} \text{ K}^{-1}$ .<sup>[43]</sup>

The electrical and thermal contact resistances are inevitable in any TEG module. If not well-controlled, these contact effects can be detrimental to the performance of TEGs.<sup>26</sup> Compared with thermal contact resistance, electrical contact resistance inflicts more serious impact on both the efficiency and output power density of TEGs. Several recent sources have reported that electrical contact resistances on the order of magnitude of  $10^{-10} \Omega \cdot m^2$  are obtainable, which reveals the practicability of creating high-quality interfaces.<sup>[91, 103-105]</sup> In this study, more conservative electrical contact resistance of  $1 \times 10^{-9} \Omega \cdot m^2$  is applied along with thermal contact resistance of  $1 \times 10^{-6} m^2 \cdot K \cdot W^{-1}$  for both the segment-segment and segment-electrode interfaces. The thermal contact resistance between the TEG

and cooling system is assumed to be ideal. In fact, Zhang et al. has demonstrated that the thermal contact resistance between TEG and cooling system is not a problem if well-managed.<sup>[91]</sup> In addition, thermal radiation and convection are also not considered in the modelling because such loss can be largely prohibited by filling and encapsulation.

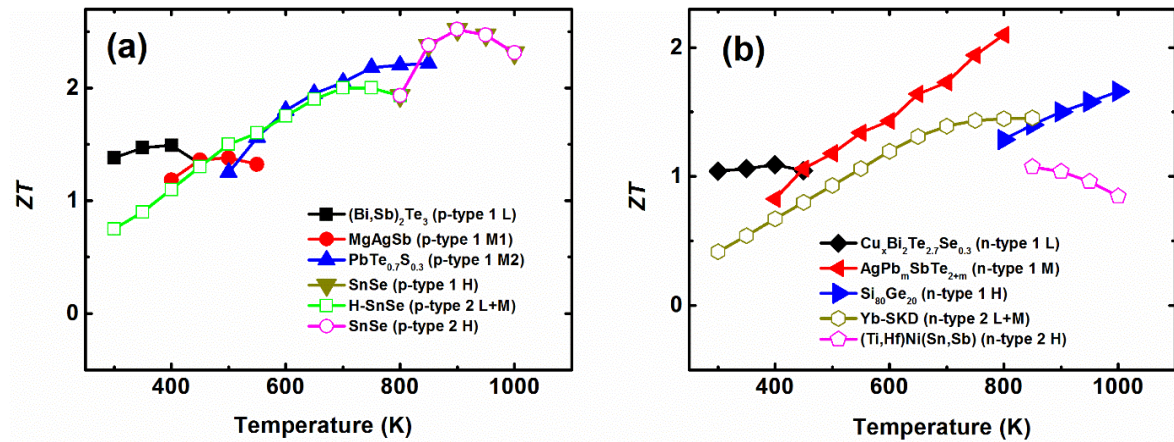


**Figure 11.**  $ZT$  values of (a) p-type and (b) n-type segmented TE materials at different operating temperature ranges. L, M, H denote low, medium and high temperatures, respectively.<sup>[13-16, 28-29, 31, 96-98]</sup>

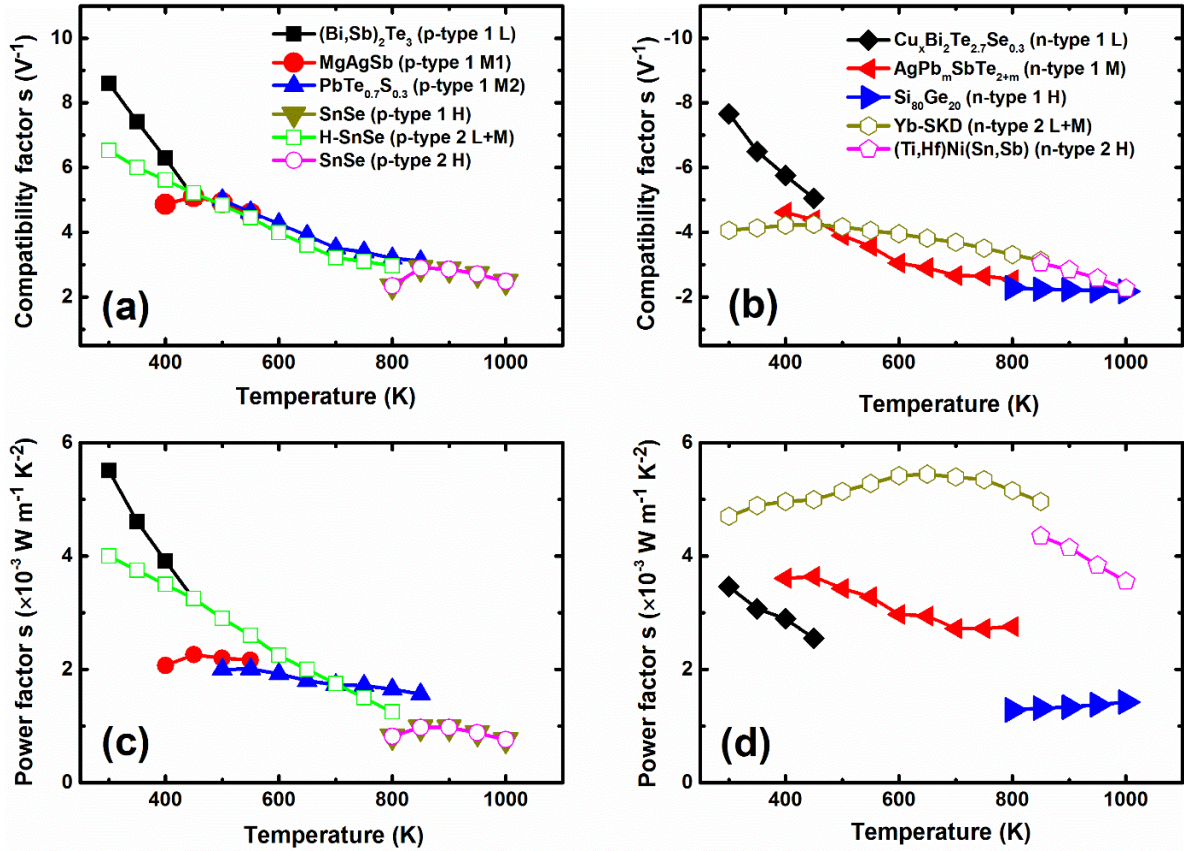


**Figure 12.** Compatibility factors (a) & (b) and power factors (c) & (d) for p-type group 1 & group 2 and n-type group 1 & group 2, respectively.<sup>[13-16, 28-29, 31, 96-98]</sup>

### 3.1.4 TEG Module Geometries

All of the TEG modules in this study are constructed with two unicouples which are connected electrically in series but thermally in parallel. Non-symmetrical leg geometries are employed to maximize the performance of TEG modules, due to the fact that n-type TE materials are universally weaker compared with their p-type counterparts. To be specific, the cross-sectional area of n-legs is smaller than the p-legs for realizing both the highest efficiency and the largest output power density. First, optimal ratios of  $A_n$  to  $A_p$  has been investigated, where  $A_n$  and  $A_p$  are cross-sectional areas of a single n-leg and p-leg,

respectively. At this stage, the length of TEG legs is kept constant at 1cm. The  $A_p$  is fixed at 1 cm × 1 cm throughout all the simulation, including the optimization of the leg length that will be discussed later. 1 cm × 1 cm cross-sectional area may seem large for one leg. The actual manufacturing usually utilizes a large number of TEG legs with small cross-sectional area to generate high output voltage for practical applications. It has been shown that with the same total active cross-sectional area and leg length of TEGs, the number of the legs should have negligible effect on both the efficiency and the output power density.<sup>[87]</sup> The TEGs used in this study with four legs each of 1 cm × 1 cm dimension could have overall equal cross-sectional areas, resulting in the same amount of TE materials used. Based on equation (14), a trial optimal  $A_n/A_p$  ratio for the highest efficiency is predicted for every assembly of p-type & n-type legs. This serves as a starting point, around which more points are assigned for simulation which attempts to find extremes for both the efficiency and output power density. Taking “p-type 1 + n-type 1” for example, the trial value of  $A_n/A_p$  ratio is calculated as 0.682, corresponding to an n-leg dimension of ~ 0.82 cm × 0.82 cm. An amending step of 0.02 cm is executed on the width of the n-leg, giving dimensions from 0.7 cm × 0.7 cm to 1.12 cm × 1.12 cm. Although the n-leg with dimensions over 1 cm × 1 cm are not necessary for tracing the maximal efficiency and power density, they are included here to offer better visual effect on the trend. During the process, the thicknesses of segmentations have been simulated iteratively to make sure that each material works in its designated temperature range. After identifying the largest output power density, the corresponding  $A_n/A_p$  ratio is kept unchanged for further optimization of the TEG leg length. The thickness of copper electrodes is 0.03 cm, which is not used in valuation of copper cost since the areal

manufacturing cost has already been accounted for. Similar situation applies to the ceramic plates' thickness of 0.05 cm, owing to the inclusion of ceramic plates' expenses into the price of heat exchangers  $\Omega_{HX}$ . The horizontal dimension of ceramic plates is chosen to be 3 cm  $\times$  3 cm, giving a cross-sectional area  $A_{HX}$  of 9 cm<sup>2</sup>.

### 3.2 Results and Discussion

#### 3.2.1 Optimization of $A_n/A_p$ Geometrical Ratio

At this stage, type I boundary conditions (BCs) are applied with hot sides and cold sides of TEG modules set to 1000 K and 300 K, respectively. With TEG leg length  $l = 1\text{ cm}$  and  $A_p = 1\text{ cm} \times 1\text{ cm}$ , varying the  $A_n/A_p$  ratio is actually altering the cross-sectional area of n-type legs. For each set of  $A_n$  and  $A_p$ , both the efficiency and output power density can be maximized with respective external load conditions, i.e.,  $R_L/R = \sqrt{1 + Z\bar{T}}$  for the efficiency and  $R_L = R$  for the output power density. The effect of an external load is simulated by changing the potential difference between two electrodes. In order to get the optimal  $A_n/A_p$  ratio, dynamic adjustment is needed simultaneously for two classes of parameters, including the magnitude of the external load and the thickness of each TE segment. **Figure 13** shows the typical current-voltage (I-V) curve and current-dependency of the TEG efficiency and output power density. Through modifying the potential difference V and iterative adjustment of the thickness of every segmentation, the highest efficiency and maximum output power density can be obtained for each  $A_n/A_p$  ratio by making sure that each TE material works in its designated temperature range. **Figure 14a** illustrates one of the constructed TEG modules utilized in this work with two p-type segments and three n-type

segments, corresponding to the assembly of “p-type 2 + n-type 1”. **Figure 14b** demonstrates the modelled temperature distribution in the same TEG module.

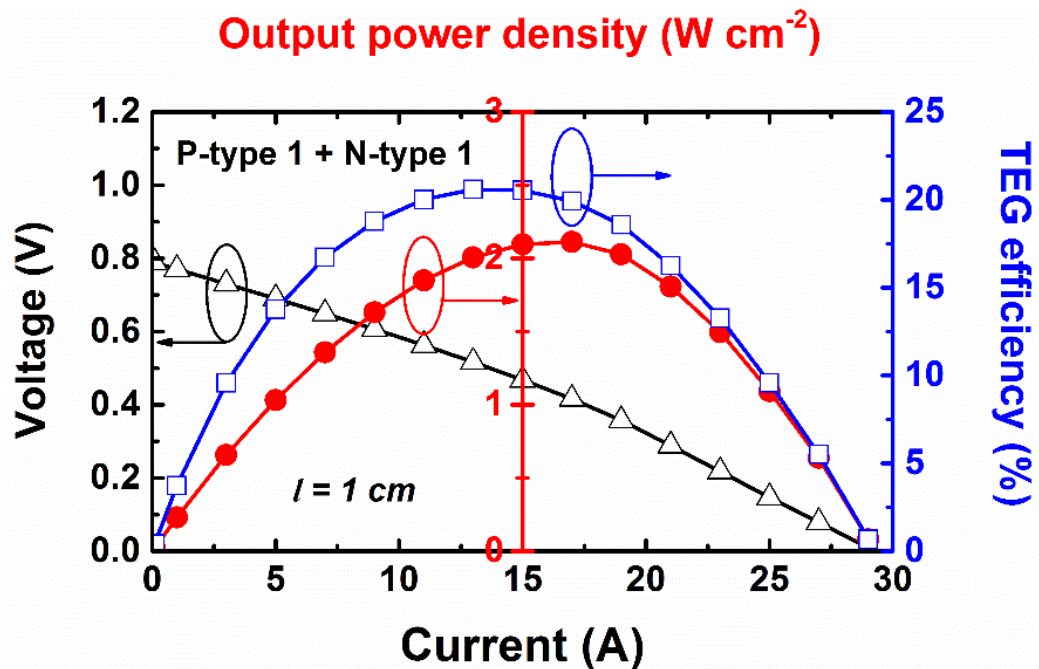


**Figure 13.** Typical current-dependency of the output voltage, efficiency and output power density in a segmented TEG.

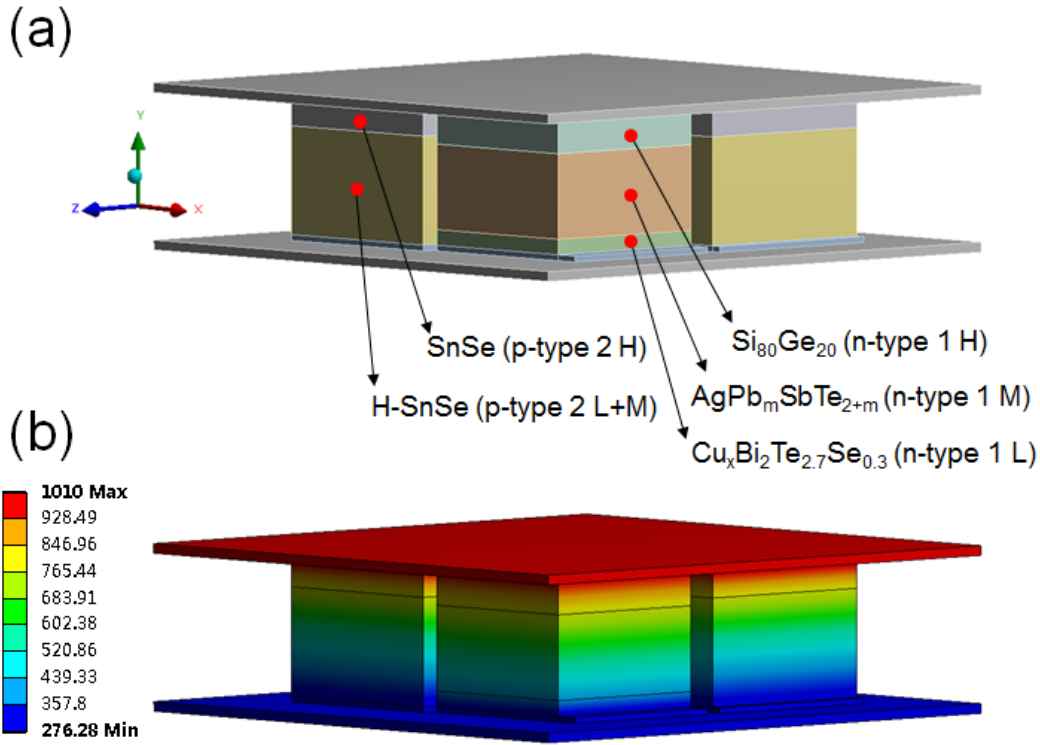


**Figure 14.** a) Modelling example of segmented TEG modules, and b) the corresponding temperature distribution.

Since the maximum output power is directly related to the estimation of cost-performance ratio, i.e. dollar per watt, the maximum output power density at each  $A_n/A_p$  geometrical ratio and corresponding efficiency are displayed in **Figure 15**. All four assemblies of “p-type 1 + n-type 1” (**Figure 15a**), “p-type 2 + n-type 1” (**Figure 15c**), “p-type 1 + n-type 2” (**Figure 15b**) and “p-type 2 + n-type 2” (**Figure 15d**) could provide peak output power densities of 2.14, 2.24, 2.55 and 2.72 Watt cm<sup>-2</sup>, respectively. With different assemblies, the largest output power densities occur at different  $A_n/A_p$  ratios, verifying that the adoption of uniform cross-sectional areas for TEG legs ( $A_n=A_p$ ) is not

beneficial to the TEG performance. Also from **Figure 15**, it can be observed that the largest output power densities come from TE materials with greater power factors but relatively lower  $ZTs$  (n-type 2) and the higher efficiency does not guarantee the larger output power density, given that the boundary conditions are fixed temperature at both the hot side and cold side of TEGs. For example, TEGs with n-type 2 (Yb-filled SKD + HHs) could produce ~ 20% more power over TEGs with n-type 1 (Chalcogenides and SiGe), even although the efficiencies are 2 percentage points lower. This can be better understood by comparing the results in **Figure 15** with the  $ZTs$  and power factors of different TE materials shown in **Figure 11** and **Figure 12**, respectively. While the  $ZTs$  of Yb-filled SKD and HHs are universally weaker, their power factors are considerably larger throughout the entire temperature range in the study, giving them an edge on power generation. According to equation (15), with their superior power factors, Yb-filled SKD and HHs will induce greater heat flux absorbed at hot sides of TEGs. At the same time, thermal energy expelled at the TEG cold sides is also expected to be significantly faster, implying the requirement of better heat exchangers. In reality, the cost of heat exchangers can be high enough to inhibit the practical application of a TEG. Even with an acceptable price of heat exchangers, the cost-performance rather than only the performance of TEGs should be carefully examined for more persuasive comparisons among different TEG modules or between TEGs and other energy sources.

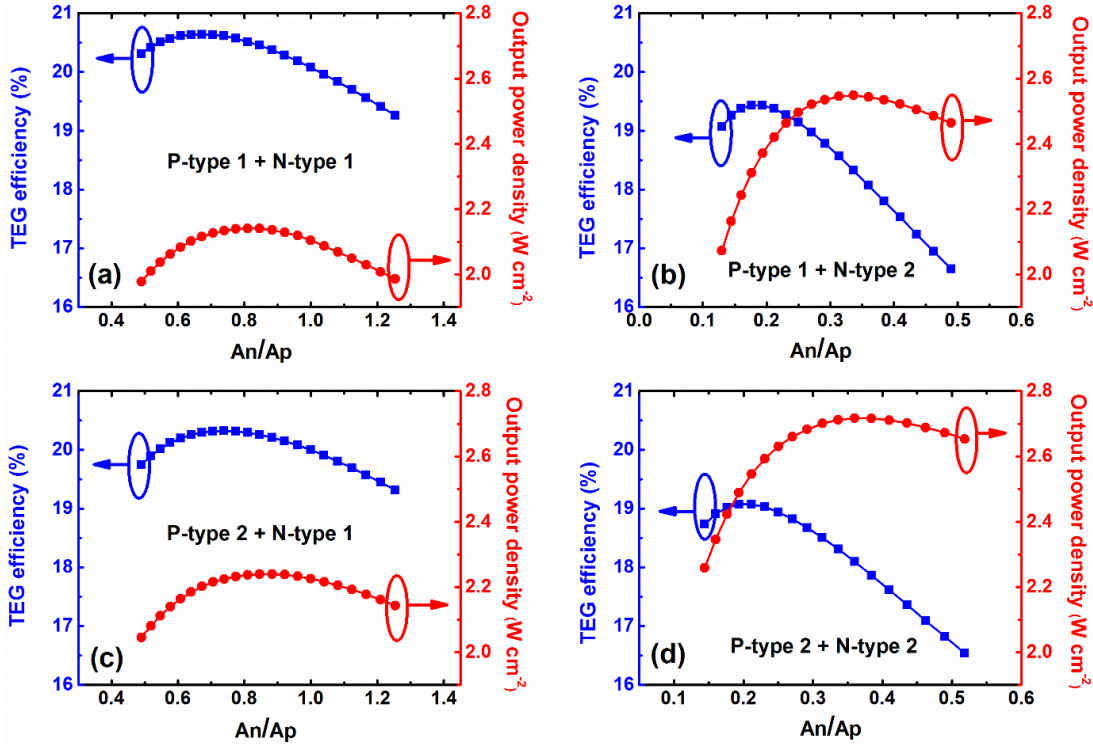


**Figure 15.** Optimal  $A_n/A_p$  ratio for the highest output power densities and corresponding TEG efficiencies for different assemblies of two p-type legs and two n-type legs.

### 3.2.2 Optimization for Cost Performance

With the optimized cross-sectional area ratios  $A_n/A_p$ , the TEG leg length  $l$  can be adjusted to search for the lowest cost-performance ratio. The second type of boundary conditions are implemented with the TEG hot side held at temperature of 1000 K while changing the heat transfer coefficients of the cold side. In addition, the cooling temperature of the heat sink is fixed at 276 K. For a specific assembly and TEG leg length  $l$ , there exists a heat transfer coefficient  $h$  that is sufficient to cool the cold side of the TEG module down to a targeted cold-side temperature, such as 300 K. Such values of the heat transfer coefficients will help maintain the appropriate temperature difference across the TEG, ensuring that the potential of selected TE materials can be fully realized. **Figure 16** displays the evolutions of

cold side temperature and output power density with respect to the variation of the heat transfer coefficient. The temperature of cold side decreases rapidly before approaching the temperature of the heat sink. Further increasing the heat transfer coefficient is no longer effective in reducing the temperature. The output power density escalates with the growth of the heat transfer coefficient but enters a saturation region when the descending of the temperature stagnates. From equation (15), dwindling the length of TEG legs can stimulate the increment of the output power when  $\Delta T$  is unchanged. With TEG leg length as a tunable parameter, the ratio of the heat transfer coefficient to the power generated is appraised for all four assemblies.

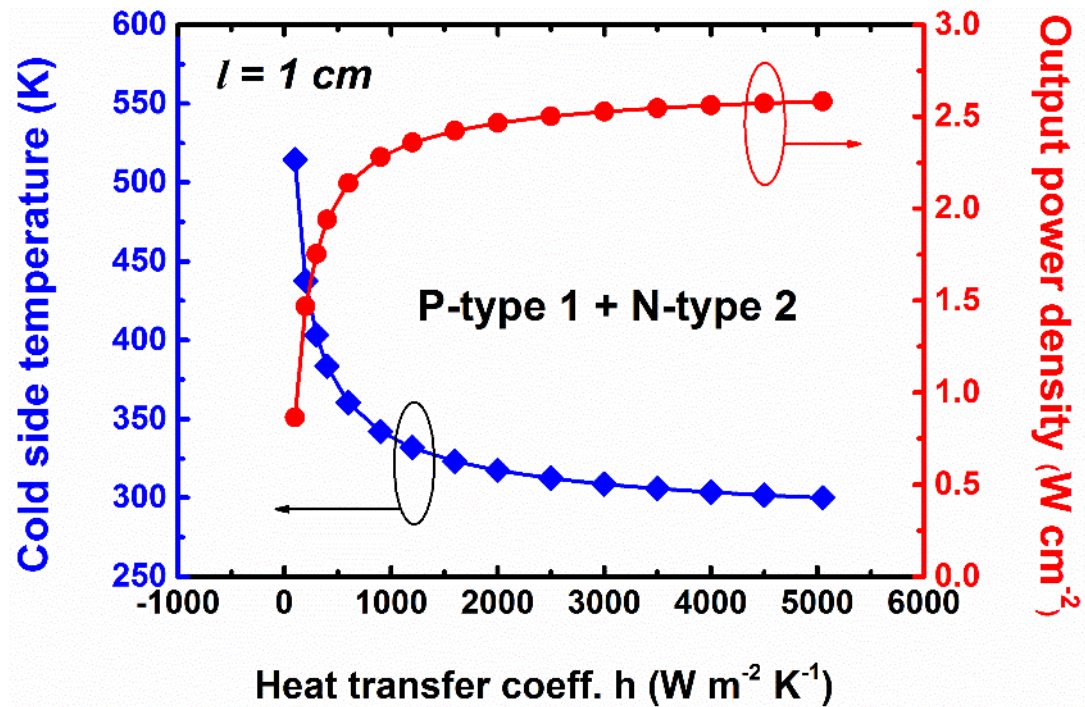


**Figure 16.** Cold side temperatures and output power densities of a TEG module versus the heat transfer coefficients at the cold side.

As shown in **Figure 17**, heat transfer coefficients arise more rapidly than the output power density, revealed by the trend of the  $h/P$  curves (green empty triangles). These results predicate that greater output power is attainable at the expense of more efficient heat exchangers. In other words, the superior output power is correlated with the higher cost. Moreover, TEGs with n-type 2 (Yb-filled SKD + HHs) require considerably larger heat transfer coefficients for generation of the same amount of power as compared with TEG modules involving n-type 1 (Chalcogenides and SiGe). For example, in order to produce 20 W of electricity, assemblies of “p-type 1 + n-type 1” and “p-type 2 + n-type 1” demand heat transfer coefficients of  $\sim 1 \times 10^4 \text{ Wm}^{-2}\text{K}^{-1}$ , while assemblies of “p-type 1 + n-type 2” and “p-type 2 + n-type 2” desire heat transfer coefficients of  $\sim 4 \times 10^4 \text{ Wm}^{-2}\text{K}^{-1}$ . It should be mentioned that the heat transfer coefficient of the forced water convection is in the range of  $300 \sim 10000 \text{ Wm}^{-2}\text{K}^{-1}$ . But this doesn’t deny the possibility of segmenting the Yb-filled SKD and HHs. In our simulation, the value of fill factor ( $F = A_{TE}/A_{HX}$ ) falls in the range between 0.30 and 0.41. NASA has successfully installed GPHS-RTG with  $F = 0.034$ , indicating that ceramic plates in our modelling can be  $\sim 10$  times larger for alleviating the burden of the heat transfer coefficient by ten-fold.

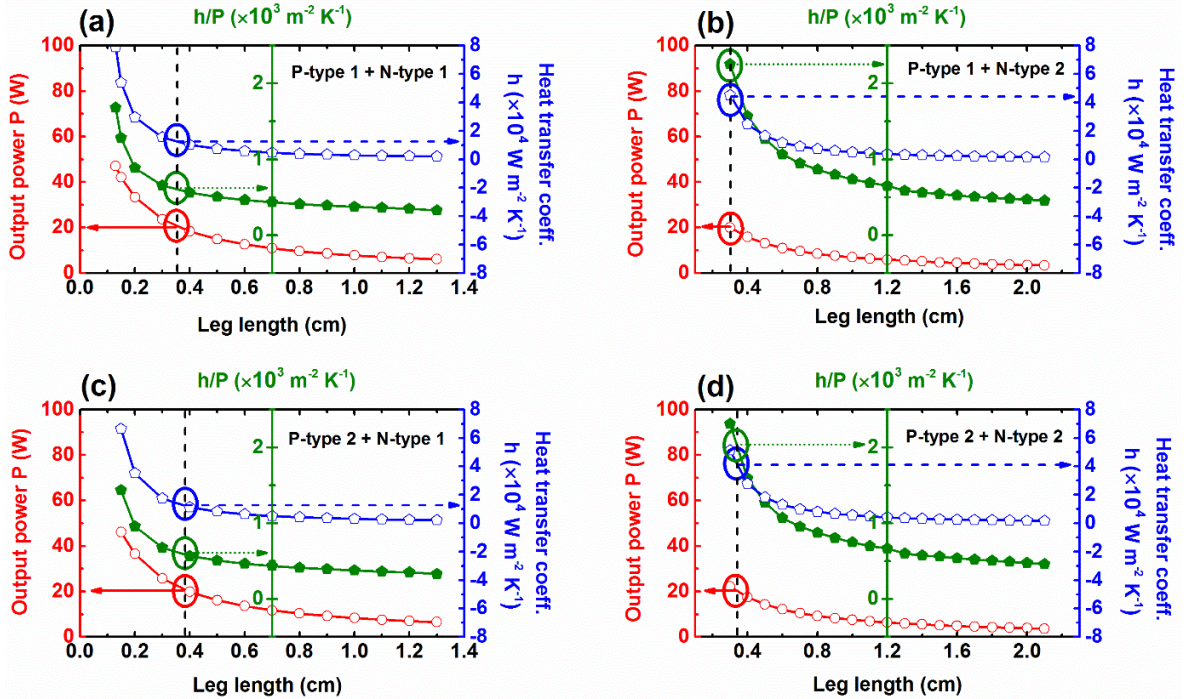


**Figure 17.** Output power and corresponding heat transfer coefficients versus leg lengths of TEGs.

With obtained optimized dimensions, output power, corresponding heat transfer coefficients, and various prices listed in both the **Table 6** and **Table 7** as well, the cost-performance ratios for the four different assemblies of TEGs can be evaluated as described in section 3.1.2. The ideal operating temperature range is from 300 K to 1000 K. Although maintaining 300 K at cold-side is challenging, this temperature configuration is used as benchmark for the selected TE materials. The unit price of heat exchanging system is taken to be 2.05 \$ W<sup>-1</sup> K for this step. As presented in **Figure 18**, the efficiencies almost stay the same with different TEG leg length until the legs are too short when the contact resistances start to become comparable to resistances of the TE materials. On the other hand, the output power density decreases monotonically with the increasing of TEG leg length when temperature difference is kept constant, which is consistent with equation (15). The curves of cost-

performance ratios show returning points at optimal TEG leg lengths around which wide plateaus exist. For example, TEG with p-type 2 and n-type 1 (**Figure 18c**) can achieve the lowest cost-performance ratio of  $0.97 \text{ \$ W}^{-1}$  at leg length of 0.7 cm while retaining an efficiency of 19.7% and supplying a power density of  $3.2 \text{ Watt cm}^{-2}$ . Assembly of “p-type 1 + n-type 1” (**Figure 18a**) comes second with a slightly higher cost-performance ratio of  $0.99 \text{ \$ W}^{-1}$ , possibly attributing to more TE-TE interfaces it have. On the contrary, segmented TEGs with n-type 2 (Yb-filled SKD + HHs) (**Figure 18b** and **18d**) reach cost-performance as low as  $1.47 \text{ \$ W}^{-1}$  at leg length of 1.3 cm, with efficiency of 18.1% and output power density of  $2.2 \text{ Watt cm}^{-2}$ , despite of their much larger power factors. These results imply that TE materials with higher  $ZTs$  are more profitable than those with larger power factors.

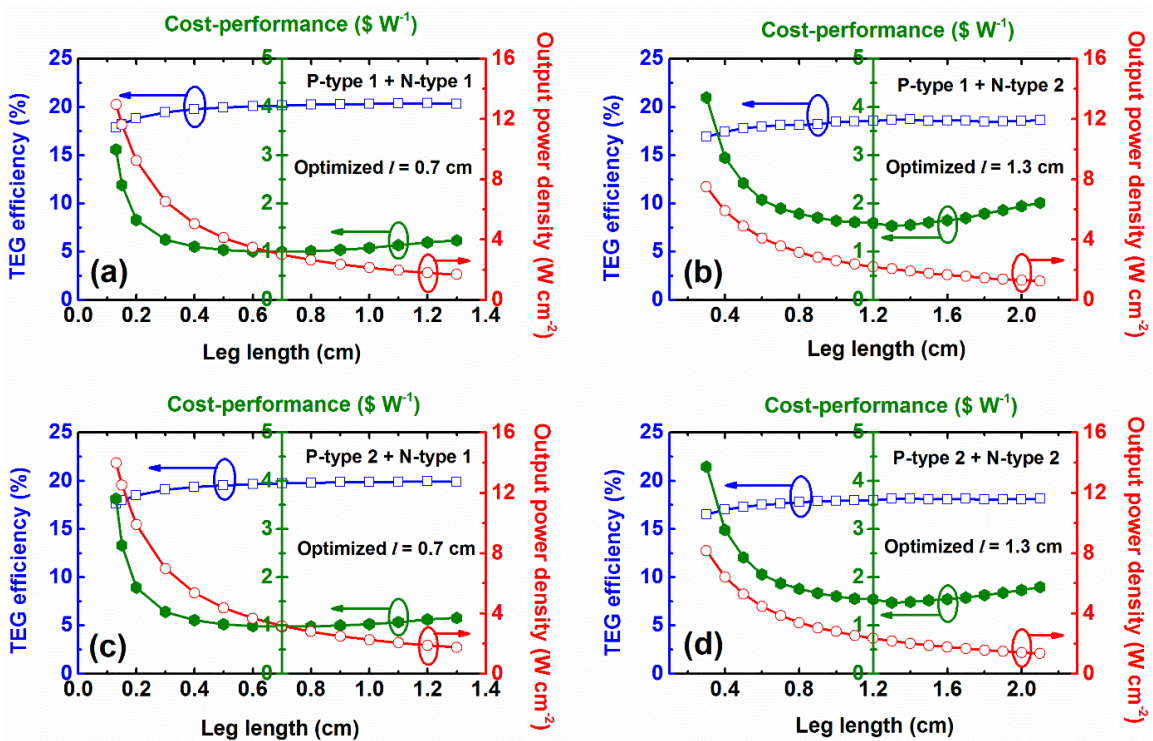


**Figure 18.** Cost-performance ratio versus leg lengths of different TEG modules.

In reality, it is challenging to maintain a cold-side temperature of 300 K for high temperature applications. The more economical approach is to allow the cold side temperature to increase.<sup>[106-107]</sup> **Figure 19** shows cost-performance ratios, TEG efficiencies and power densities at various cold-side temperature but fixed hot-side temperature at 1000 K. The unit price of heat exchanging system is chosen to be 10 \$ W<sup>-1</sup> K, which is closer to the current price compared to 2.05 \$ W<sup>-1</sup> K. It can be seen that the efficiency drops with the increase of the cold-side temperature, which is easy to understand since the Carnot efficiency decreases with the reduction of the temperature difference across the TEGs. However, the output power densities surprisingly rise with the declined temperature differences. The reason is that for a specific assembly of TE groups, saying “p-type 2 + n-type 1”, the optimal geometries at different temperature configurations are not the same, especially the optimized leg length. According to equation (15), if the diminution of the leg length outpaced the reduction of the temperature difference, the heat flux density and output power density will escalate. The cost-performance ratios experience a fast descending trend with the ascending temperature of the TEG cold-side, due to the reducing level of heat transfer coefficients. It should be pointed out that both the trends of the output power and cost-performance ratio won’t last infinitely and will see returning points at some higher temperature of the TEG cold side, when the decline of the cost will be overtaken by the reduction of the power generation. After all, the cost-performance ratios of segmented TEGs in this study can reach the benchmark of 1 \$ W<sup>-1</sup> at  $T_c = 373\text{ K}$ . The assemblies of “p-type 1 + n-type 1” and “p-type 2 + n-type 1” can achieve 0.88 \$ W<sup>-1</sup> and 0.86 \$ W<sup>-1</sup>, respectively. In contrast, assemblies of “p-type 1 + n-type 2” and “p-type 2 + n-type 2” can attain 1.13 \$ W<sup>-1</sup> and

$1.11 \text{ \$ W}^{-1}$ , respectively. Corresponding to the lowest cost-performance ratio of  $0.86 \text{ \$ W}^{-1}$  with the unit price of heat exchangers at  $10 \text{ \$ W}^{-1} \text{ K}$ , assemblies of “p-type 2 + n-type 1” could provide power densities of  $3.0 \text{ Watt cm}^{-2}$  with efficiency of 17.8%. These results indicate that the segmented TEGs have the potential to compete with other types of power generation methods, such as photovoltaic cells. The  $\sim 1 \text{ \$ W}^{-1}$  capability of the high-performance segmented TEGs announces the financial feasibility and competitiveness of the thermoelectric technology.

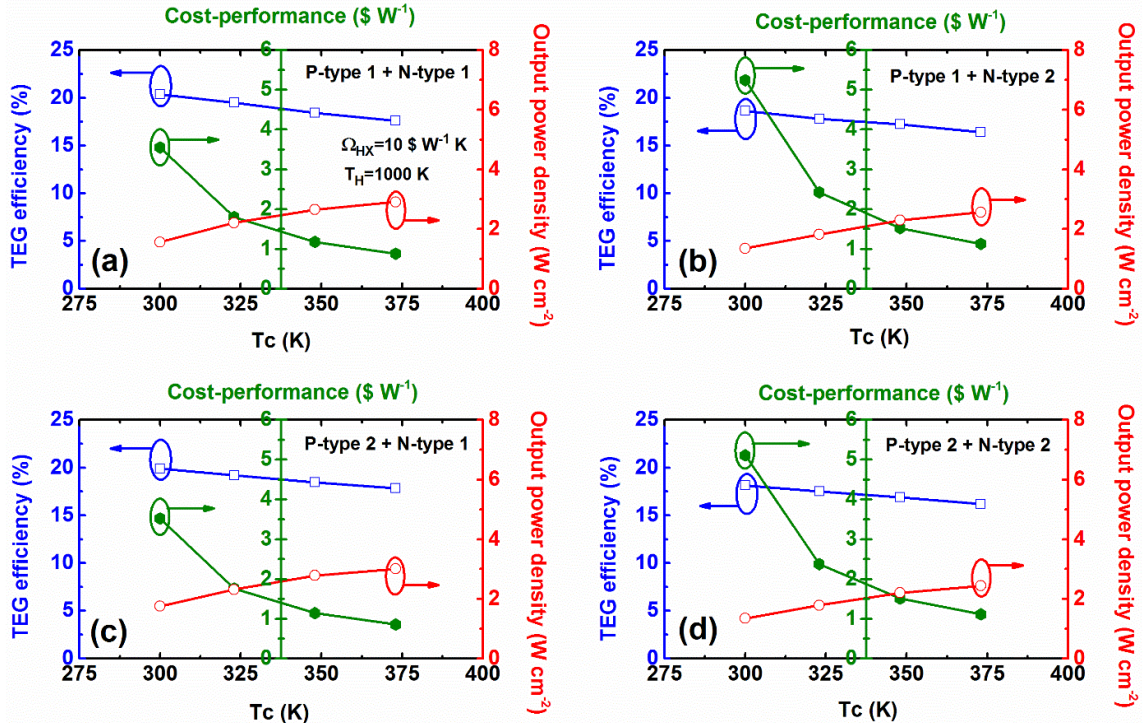


**Figure 19.** Cost-performance ratios, TEG efficiencies and power densities versus different cold-side temperature and fixed hot-side temperature at  $1000 \text{ K}$ . The unit price of  $10 \text{ \$ W}^{-1} \text{ K}$  for heat exchangers is used here.

## **CHAPTER 4. RAPID LAYER-SPECIFIC ANNEALING ENABLED BY ULTRAVIOLET LED WITH ESTIMATION OF DEPOSITION ENERGY FOR HIGH-PERFORMANCE PEROVSKITE SOLAR CELLS**

In this chapter, I demonstrate accurate-controlled photonic annealing on  $\text{CH}_3\text{NH}_3\text{PbI}_3$  ( $\text{MAPbI}_3$ ) PVSK thin film by using 365-nm LEDs. This wavelength selection aligns well with the peak absorption of  $\text{MAPbI}_3$  in the ultraviolet A (UVA) range at  $\sim 354$  nm.<sup>[108]</sup> There is a misconception that UV light is the cause of  $\text{MAPbI}_3$  decomposition.<sup>[109-111]</sup> I consider that this is not a proper conclusion without mentioning the dosage of the UV exposure. Annealing PVSK thin film is essentially an energy-absorbing and -consuming crystallization process. Any annealing method can actually damage the PVSK film if the energy supply is not well-controlled. For example, overheating can destroy PVSK films but that doesn't prevent the wide-spread usage of thermal annealing.<sup>[112-114]</sup> I show that with well-controlled dosages, UV irradiation can facilitate perovskite reaching a good crystalline state and favorable surface morphology. The resulting devices with simple planar inverted structure (p-i-n) ITO/PEDOT:PSS/  $\text{MAPbI}_3/\text{PC}_{71}\text{BM}/\text{Al}$  can achieve efficiency over 18% without annealing the  $\text{PC}_{71}\text{BM}$  layer, though the current density versus voltage characteristics (J-V curves) show obvious hysteretic behavior between the forward scan and reverse scan. In cases where  $\text{PC}_{71}\text{BM}$  also undergoes proper UV illumination, the hysteresis can be eliminated, while the best device PCE reaches a new height close to 19%. These results fully justify that if the UV dosage is well-managed, UV light is capable of annealing PVSK into high-quality thin film rather than simply damaging it. In addition, the UV-LED-annealing approach also provides a

convenient route for accurately estimating the energy required to grow PVK films of good quality for high-performance devices. I believe that energy is more appropriate than temperature for characterizing the crystallization process. With the temperature and time known for thermal annealing, it is still not possible to estimate the actual energy required to form high-quality PVK thin films. On the contrary, the deposition energy can be calculated from UV annealing with the irradiance and the illumination time, assuming an almost full absorption of the incident light. By using LEDs with nearly one single wavelength, an almost-full absorption (> 99.99%) can be guaranteed by the thickness of  $\text{MAPbI}_3$  active layer around 400 nm in my solar cells. The product of the irradiance of the light source and the illumination time yields a neat estimation of the energy that is necessary for fully crystallizing the  $\text{MAPbI}_3$  film to a quality required for device applications. In addition to the traditional  $\text{MAPbI}_3$  material, this novel photonic treatment approach could also find applications on other emerging PVK material systems for photovoltaics as well as all other PVK thin film based semiconductor devices, such as PVK light-emitting diodes and photodetectors.

#### **4.1 Experimental Section**

Materials preparation: Poly(3,4 - ethylenedioxythiophene:poly(styrenesulfonate) (PEDOT:PSS, Clevios AI 4083) was obtained from Heraeus Co. Lead iodide ( $\text{PbI}_2$ , 99.999%) was purchased from VWR. Methylammonium iodide (MAI, 98%) was purchased from Greatcell Solar (formerly known as Dyesol). [6,6] - phenyl -  $\text{C}_{71}$  - butyric acid methyl ester (PC<sub>71</sub>BM) was purchased from Nano-C. N,N - dimethylformamide (DMF, anhydrous,

99.8%), dimethyl sulfoxide (DMSO, anhydrous, 99.9%), toluene (anhydrous, 99.8%) and Chlorobenzene (CB, anhydrous, 99.8%) were purchased from Sigma-Aldrich. All chemicals were used as received without further purification.

Device fabrication: The ITO-glass substrates were ultrasonically washed within deionized water (1% Hellmanex), acetone, and isopropanol each for 30min successively. After drying, the cleaned ITO-glass substrates were treated by the UV-Ozone for 15min and then used immediately for sequential deposition of different layers. PEDOT:PSS layer was spin-coated (5,000 r.p.m. for 45 s) and annealed at 150 °C for 20 minutes. To form a PVK precursor, two milli-moles of PbI<sub>2</sub> and two milli-moles of MAI were mixed and dissolved in 1.4 mL DMF with 2 milli-moles of DMSO. The as-prepared MAPbI<sub>3</sub> precursor and PC<sub>71</sub>BM solutions (20 mg/mL, dissolved in CB) were stirred for overnight. The PVK precursor solution was dripped onto the PEDOT:PSS-coated ITO-glass substrates kept at room temperature. The spin-coating of PVK films was conducted in an N<sub>2</sub>-filled glovebox (below 1.0 ppm O<sub>2</sub> and H<sub>2</sub>O) at 4000 rpm for 45s. 10 seconds after the start of the spin-coating, 500 μL Toluene were dropped onto the PVK layer. PC<sub>71</sub>BM layer was spun at 4,000 r.p.m. for 35s (subject to UV annealing) to 70s (no annealing). Finally, the devices were completed by the thermal evaporation of aluminum as counter-electrode (~ 100 nm).

UV annealing and irradiance measurements: UV annealing was achieved by a Dymax RediCure LED emitter with the peak wavelength at 365 nm. Both the irradiance from the LED source and the transmission irradiance through different layers, including cleaned ITO/glass, PEDOT:PSS/ITO/glass, and the conversion of MAI-PbI<sub>2</sub>-DMSO to MAPbI<sub>3</sub> on top of PEDOT:PSS/ITO/glass, were measured by a radiometer RM-22 (from Opsytec) with a

UVA sensor (also from Opsytec, spectral range from 330 nm to 455 nm) calibrated at 365 nm.

Characterization: The X-ray diffraction (XRD) spectra were collected by a Bruker D8 Discover X-ray diffractometer. The absorption spectra were recorded using a UV-Vis spectrophotometer (UV-1800 from Shimadzu). Both the cross-sectional and the top-view scanning electron microscopy (SEM) images were taken using the JEOL 7000 field-emission scanning electron microscope. The *J-V* curves were measured by a semiconductor device analyzer (Agilent B1500A) under simulated AM 1.5 condition (Newport 91195A) with a power density of 100mW cm<sup>-2</sup>, which was calibrated with a standard reference cell (Oriel 91150V). The external quantum efficiency (EQE) was measured with a monochromator (Newport 74100), a xenon lamp (Newport 66902), a Si detector (Newport 71640) and an optical power meter (Newport 70310).

## 4.2 Results and Discussion

### 4.2.1 UV-LED-annealing of MAPbI<sub>3</sub> and PC<sub>71</sub>BM Films

The CH<sub>3</sub>NH<sub>3</sub>PbI<sub>3</sub> (MAPbI<sub>3</sub>) PVK films were directly deposited onto PEDOT:PSS-coated ITO-glass substrates in a glove box. CH<sub>3</sub>NH<sub>3</sub>I (MAI) and PbI<sub>2</sub> dissolved in DMF containing DMSO were dripped and spin-coated onto the PEDOT:PSS layer to form the MAI-PbI<sub>2</sub>-DMSO adduct. Toluene was used to perform the anti-solvent wash during the spin-coating process, resulting in a transparent film of MAI-PbI<sub>2</sub>-DMSO intermediate. After the spin-coating, films of MAI-PbI<sub>2</sub>-DMSO adduct on substrates were transferred out of the glove box for UV irradiation. In order to attain effective photonic annealing, the UV source employed in this study is an ultraviolet A (UVA) LED with the peak wavelength at 365 nm.

As illustrated in **Figure 20a**, the extinction coefficient  $k$  (absorption) of  $\text{MAPbI}_3$  has its peak value in the ultraviolet A (UVA) range at  $\sim 354 \text{ nm}$ .<sup>[108]</sup> Such peak absorption wavelength is in great match with the peak wavelength of 365 nm and narrow bandwidth of the spectrum from LED light source utilized. The thicknesses of normal  $\text{MAPbI}_3$  films (usually  $> 300 \text{ nm}$ ) and the large extinct coefficient of  $\text{MAPbI}_3$  at 365 nm ensure an almost-full absorption ( $> 99.99\%$ ) of the incoming UV light photons. The distance between the film surface and the UV light source was kept at 15 mm, corresponding to an irradiance of  $2.22 \text{ W cm}^{-2}$  when the output power was set to be 100%. For annealing the  $\text{MAPbI}_3$  layer, the UV illumination time was varied from 1 second to 13 seconds, with 1 second as increments. The UV-treated films were first checked visually for color changes. The transparent film began to change color quickly after the start of the UV illumination, reaching light-brown at  $\sim 3$  seconds, brown at  $\sim 7$  seconds and turning into dark brown at  $\sim 9$  seconds, after which the visible color change slowed down and became negligible. With 13-second of UV illumination, the dark-brown film began to turn whitish, indicating the decomposition of  $\text{MAPbI}_3$  into MAI and  $\text{PbI}_2$ . The color change from transparent (**Figure 20b**) to dark-brown (**Figure 20c**) indicates the transformation from the MAI- $\text{PbI}_2$ -DMSO adduct to  $\text{MAPbI}_3$  film. With UV annealing more than 9s, the obtained films appeared dark brown with a very smooth film surface. Back in the glove box, a thin layer of  $\text{PC}_{71}\text{BM}$  film as the electron-transport layer (ETL) was spin-coated directly on the UV-annealed PVK film. We noticed that the  $\text{PC}_{71}\text{BM}$  dissolved in CB had a high probability of partially washing off the underlying  $\text{MAPbI}_3$  PVK layers with UV annealing time less than 9 seconds. This phenomenon indicates that duration less than 9s of given UV intensity is not enough to form robust  $\text{MAPbI}_3$  films. The substrates after

deposition of PC<sub>71</sub>BM films were also transferred out of glove box for UV irradiation with the same LED source, as shown in **Figure 20d**. There was no change to the PC<sub>71</sub>BM films that could be detected visually. Sharing the same spin speed, two different spin-coating times were used to deposit PC<sub>71</sub>BM films: 35 seconds followed by further UV annealing, and 70 seconds for driving off the remnant CB solvent without UV annealing. The PC<sub>71</sub>BM layers were not able to endure the 100% output of UV radiation at the same distance, even for 0.5 second. Thus, reduced UV intensity lower than 100% (50%, 30% and 10%) were tried for 1-second and 0.5-second duration. Thermal-annealed samples were also fabricated as references for comparison.

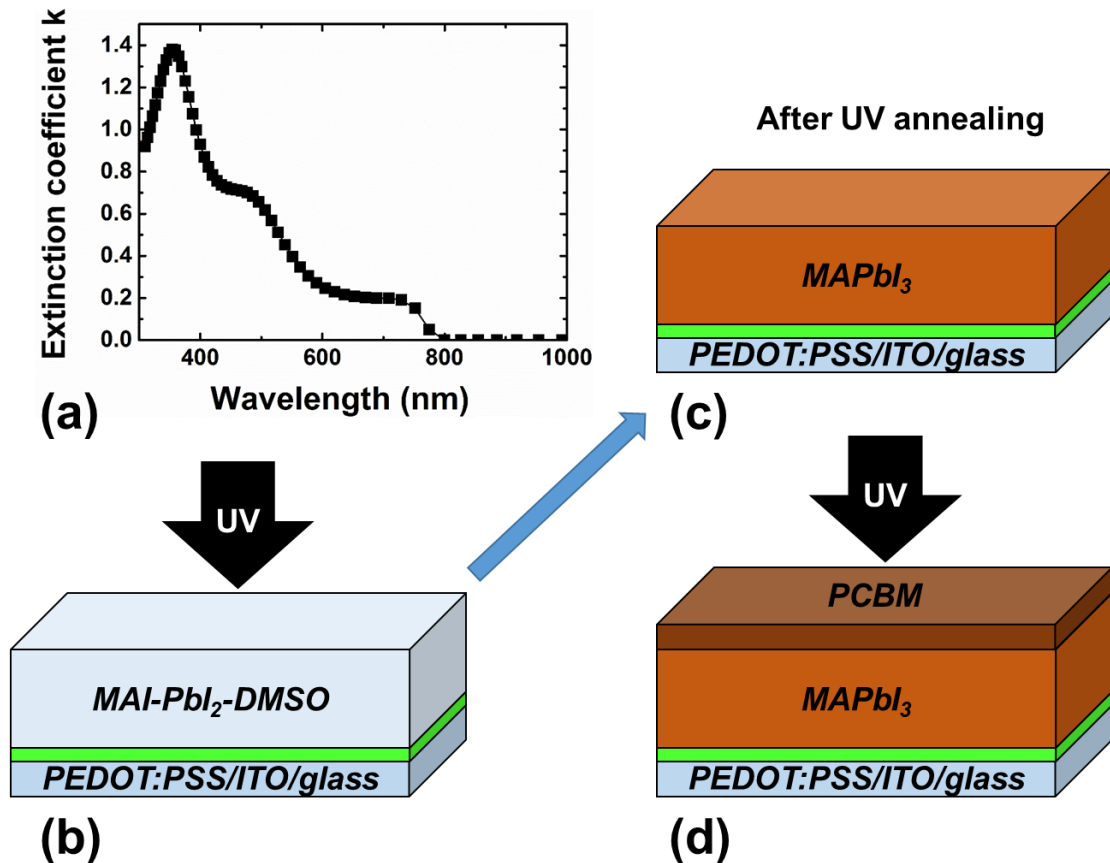


**Figure 20.** (a) spectral extinction coefficients of MAPbI<sub>3</sub> PVSK film; (b) illustration of UV annealing on the PVSK light-absorbing (active) layer, which starts as the transparent MAI-PbI<sub>2</sub>-DMSO adduct; c) dark brown MAPbI<sub>3</sub> film forms after proper UV annealing (> 9 seconds) and (d) illustration of UV annealing on the PCBM ETL layer, which doesn't show any visible color change.

#### 4.2.2 Photovoltaic (PV) Performances of PVSCs with UV-LED-annealing Only on PVSK Layer

The impact of UV annealing on the efficiency of PVSCs was investigated systematically. In order to explore the potential of UV annealing, inverted planar (p-i-n) PVSCs with a configuration of ITO/PEDOT:PSS/MAPbI<sub>3</sub>/PC<sub>71</sub>BM/Al were fabricated. Figure 21 shows the J-V characteristics of PVSCs based on thermal-annealed MAPbI<sub>3</sub> films and UV-annealed MAPbI<sub>3</sub> films with different UV-irradiation times, but without annealing of

any kind (neither thermal nor UV annealing) on PC<sub>71</sub>BM layers. The corresponding photovoltaic performance parameters for PVSCs, such as efficiency and fill factor (*FF*), have also been summarized in **Figure 21**. A typical control PVSC with the PVK layer thermal-annealed at 100 °C for 30 minutes exhibited PCEs of 12.56% and 14.50% from forward and reverse scans, respectively. In contrast, the UV-treated samples achieved notable concurrent enhancements of the PCE, *FF*, open-circuit voltage (*V<sub>OC</sub>*), and short-circuit current density (*J<sub>SC</sub>*). PVSCs with UV annealing of 11s yield much better photovoltaic performance, with PCEs of 16.24% and 18.66% from forward and reverse scans, respectively. The detailed photovoltaic parameters of the devices are listed in part a) of **Table 8**. **Figure 21b** shows the effect of UV annealing time on the performance of PVSC devices (reverse scan only for comparison). It is obvious that UV annealing of 11s produces PVK solar cells with not only the highest efficiency and fill factor, but also the largest *V<sub>OC</sub>* and *J<sub>SC</sub>*. Even 9s of UV annealing yields better device performance than the thermal-annealed devices. PVSCs with UV annealing of 13s show an apparent misshaped J-V curve, much lower *FF*, *V<sub>OC</sub>* and *J<sub>SC</sub>*, due to the degradation of the MAPbI<sub>3</sub> PVK film from over-dose exposure. PVSCs with UV annealing of 7s exhibit extremely low current density and show a bad shape in J-V curve because of insufficient energy to form the high-crystalline MAPbI<sub>3</sub> PVK film required at a device level. Nonetheless, the demonstrated UV-annealed devices showed much better photovoltaic performance than their thermal-annealed counterparts, highlighting the effectiveness of such a photonic treatment for constructing high-performance PVSCs. Furthermore, UV-annealed PVSCs can be fabricated within much shorter annealing time (in the order of seconds) and thus have better compatibility with those scale-up processing

methods such as large-scale roll-to-roll (R2R) manufacturing.

**Table 8.** Photovoltaic parameters of devices from both the UV- and thermal-annealing.

MAPbI <sub>3</sub> annealing	PC <sub>71</sub> BM annealing	Scan directions	Efficiency (%)	FF	V <sub>oc</sub> (V)	J <sub>SC</sub> (mA cm <sup>-2</sup> )	
<b>Part a</b>							
Thermal	N/A	Forward	12.56	62.66	0.95	-21.10	
		Reverse	14.50	72.30	0.95	-21.12	
		Average	13.53	67.48	0.95	-21.11	
UV		Forward	16.24	69.75	1.03	-22.60	
		Reverse	18.66	79.87	1.03	-22.68	
		Average	17.45	74.81	1.03	-22.64	
<b>Part b</b>							
Thermal	Thermal	Forward	14.68	72.52	0.96	-21.09	
		Reverse	14.80	73.20	0.96	-21.06	
		Average	14.74	72.86	0.96	-21.08	
UV	UV	Forward	18.80	80.08	1.04	-22.58	
		Reverse	18.90	80.33	1.04	-22.63	
		Average	18.85	80.21	1.04	-22.61	

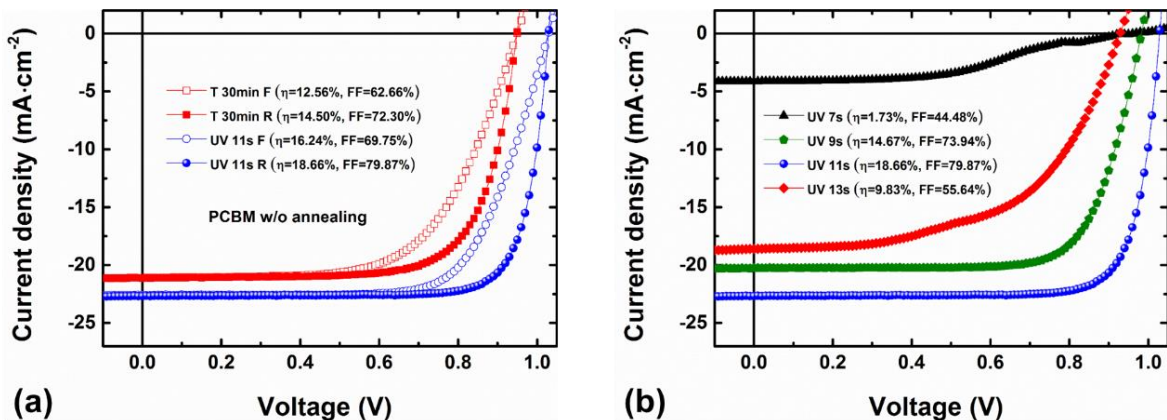


**Figure 21.** a) Performance comparison between thermal-annealed and UV-annealed PVSCs; b) the J-V characteristics of PVSCs in reverse scan with different UV annealing time from 7s to 13s on the PVSK active layer only. For all the devices involved, no annealing of any kind (neither thermal nor UV annealing) was applied on PC<sub>71</sub>BM layers.

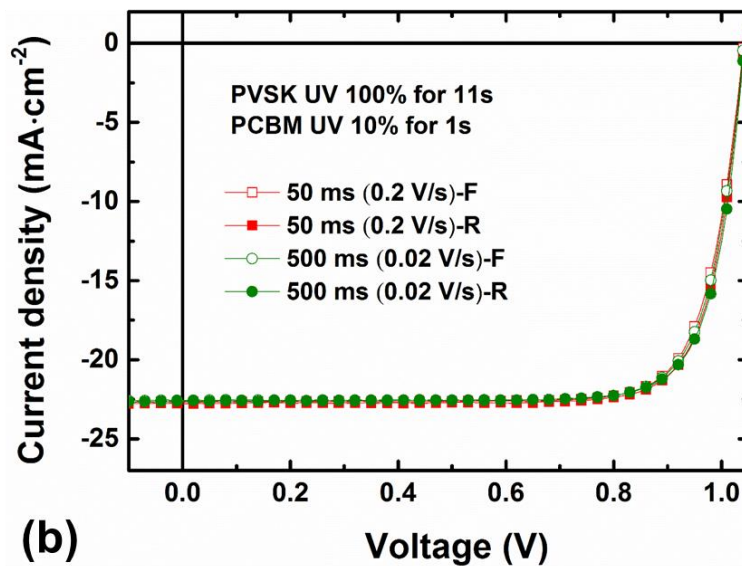
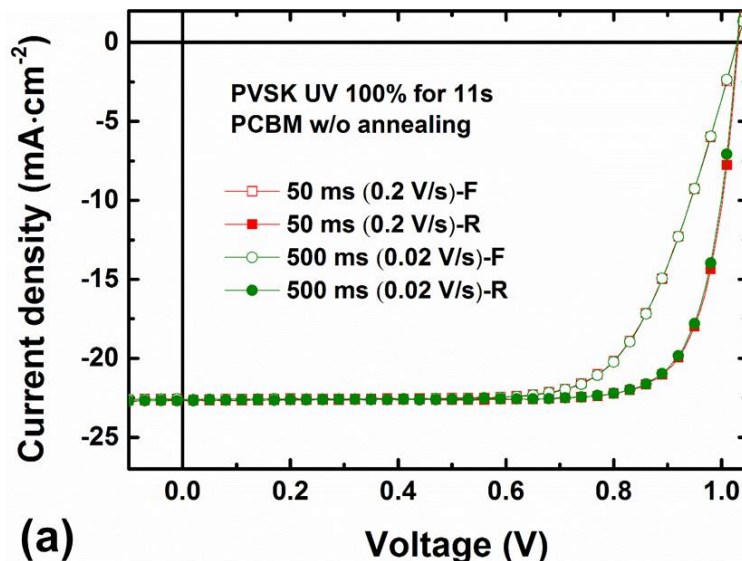


**Figure 22.** a) J-V curves with apparent hysteric behavior at different scan rates. PVSCs with UV annealing of 11s (100% intensity) on the  $\text{MAPbI}_3$  layer but no UV annealing on the  $\text{PC}_{71}\text{BM}$  layer. b) Hysteresis-free J-V characteristics at different scan rates, which are from the best PVSCs with the optimized UV-LED-annealing conditions: 11s (100% intensity) on the  $\text{MAPbI}_3$  active layer and 1s (10% intensity) on the  $\text{PC}_{71}\text{BM}$  ETL layer.

#### **4.2.3 Device Performance with UV-LED-annealing for Both MAPbI<sub>3</sub> PVK Active Layer and PC<sub>71</sub>BM ETL Layer**

The J-V curves of PVSCs with both thermal and UV annealing only on MAPbI<sub>3</sub> films show obvious hysteresis between reverse and forward scan modes (**Figure 21a**). Such behavior was observed in further examination at different scan rates (**Figure 22a**). It is anticipated that this hysteretic behavior was caused by the non-annealed PC<sub>71</sub>BM layers, which functioned as an incomplete electron transport layer, resulting in imbalanced electron and hole charge transport and collection.<sup>[115]</sup> In order to find the right dosage for UV annealing of the PC<sub>71</sub>BM films and remove the hysteresis, different exposure times and UV intensities were examined. Because UV annealing of 11s with 100% (2.22 W cm<sup>-2</sup>) intensity works best for PVK layer, this condition was kept unchanged while the optimization of UV annealing on PC<sub>71</sub>BM was executed. The thickness of the PC<sub>71</sub>BM layer in our devices is around 55 nm (**Figure 23**), much thinner than the MAPbI<sub>3</sub> active layer. With this thickness and the extinction coefficient of the PC<sub>71</sub>BM at 365nm<sup>[116]</sup>, only ~ 50% of the 365-nm UV light will be absorbed by the PC<sub>71</sub>BM layer. In consequence, shorter time and/or lower UV light intensity should be used on the PC<sub>71</sub>BM layer to prevent the unabsorbed half of the UV light from over-exposing the underlying MAPbI<sub>3</sub> thin film, which has already received the optimized 11s of 100% intensity UV irradiation. First, I tried shorter exposure times from 0.5s to 2s with unchanged UV intensity, i.e. 100% output from the UV LED source. 2s of 100% intensity UV light on PC<sub>71</sub>BM layer means an energetic equivalent of 1s of 100% UV light goes to PVK layer. As a result, the total exposure time of PVK layer to the UV light of 100% intensity is 12 seconds, which is beyond the optimized value 11s for PVK layer. With extremely high UV intensity in this study, even 1 more second of exposure will make a

huge difference in film quality. **Figure 24a** shows the J-V characteristics in both reverse and forward scans, with the corresponding photovoltaic performances briefed. It is evident that the 100% UV intensity is effective in removing the hysteresis. However, this intensity is so strong that even for 0.5 seconds, the device performance parameters dropped significantly compared to those of the best device without UV annealing on the PC<sub>71</sub>BM layer (**Figure 21a**). The performance degradation could be attributed to the damage to either PC<sub>71</sub>BM layer or PVSK layer, or possibly both. I then fixed the exposure time at 1s but varied UV intensities from 10% to 50% of the 2.22 W cm<sup>-2</sup> output. **Figure 24b** displays a clear trend in which 10% UV intensity for 1s results in the best device performance with hysteresis-free J-V characteristics. At 10% intensity, further decreasing the irradiation time to 0.5s fed energy deficient to get rid of the hysteresis behavior. After all, it turns out that UV annealing on the PC<sub>71</sub>BM layer is capable of eradicating hysteretic behavior, and the highest efficiency can be accomplished concurrently as long as appropriate UV exposure is performed on both the MAPbI<sub>3</sub> and PC<sub>71</sub>BM layer.

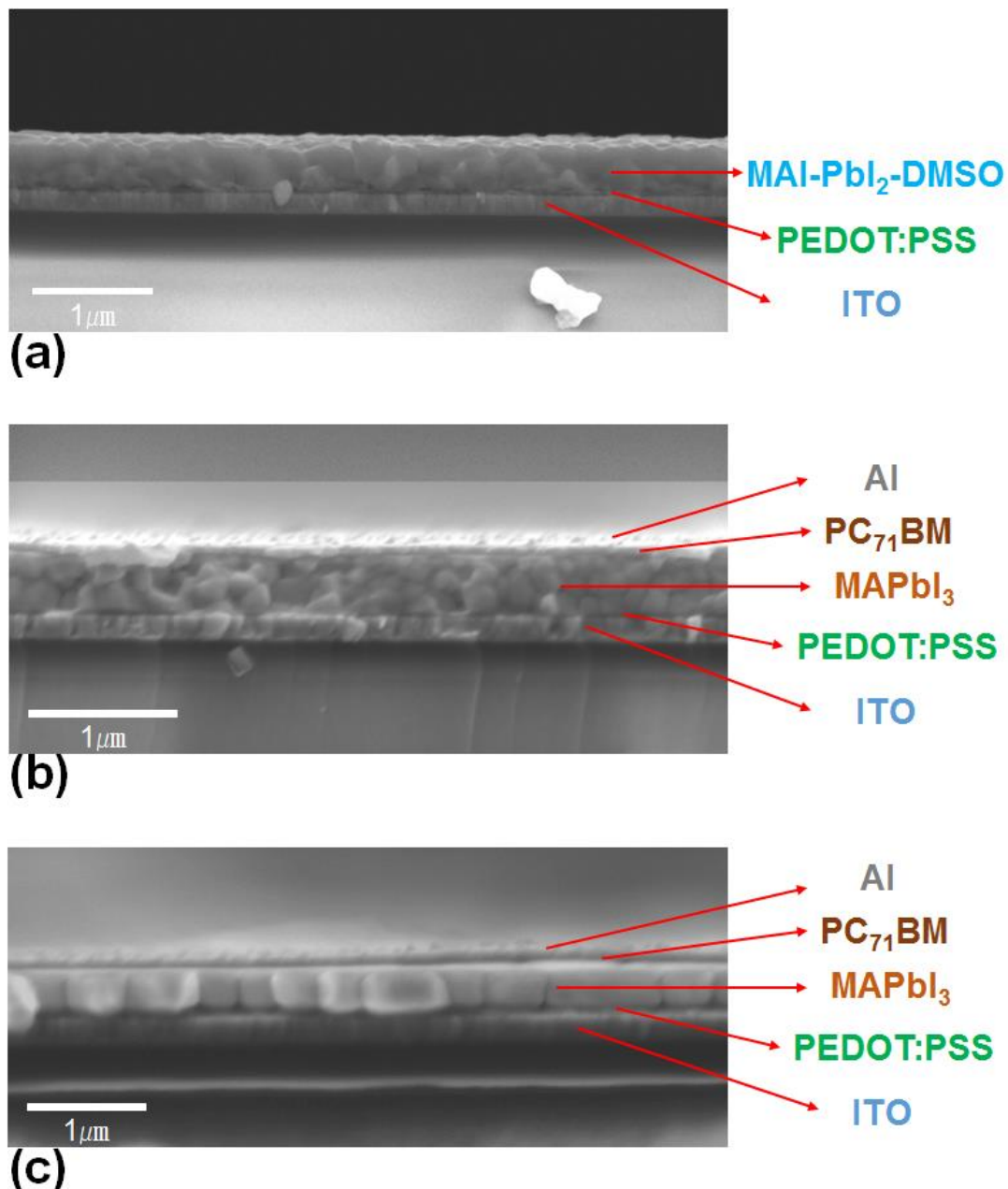


**Figure 23.** Cross-sectional SEM images of a) MAI-PbI<sub>2</sub>-DMSO / PEDOT:PSS / ITO / glass before any annealing, b) Al/PC<sub>71</sub>BM/MAPbI<sub>3</sub>/PEDOT:PSS/ITO with PVSK layer & PC<sub>71</sub>BM layer annealed by UV for 11s (100%) & 1s (10%), respectively and c) Al/PC<sub>71</sub>BM/MAPbI<sub>3</sub>/PEDOT:PSS/ITO with both the PVSK layer & PC<sub>71</sub>BM layer annealed by hot plate at 100 °C for 30 minutes.

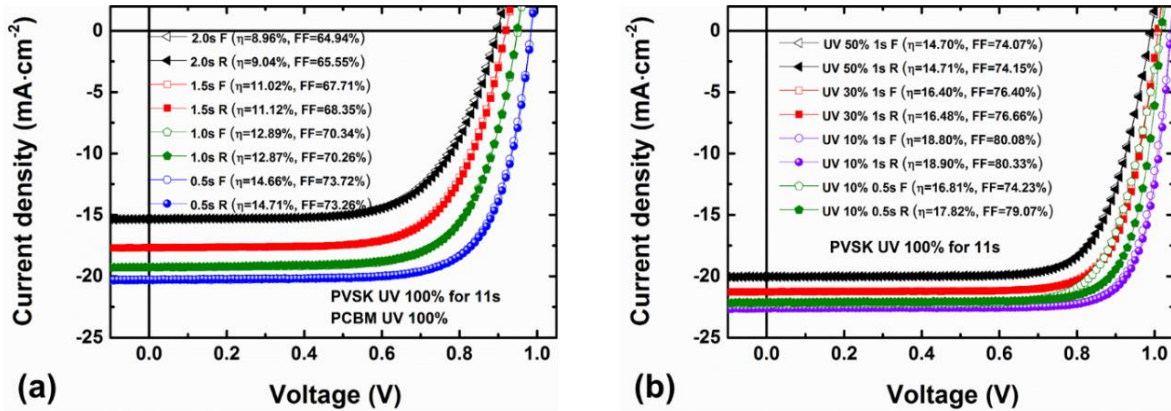


**Figure 24.** Optimization of UV annealing on the PC<sub>71</sub>BM layer: a) using 100% UV intensity on PC<sub>71</sub>BM with different irradiation time from 0.5s to 2s; b) irradiating the PC<sub>71</sub>BM layer for 1s with different UV intensities from 10% to 50%, while result of 10% UV intensity for 0.5s on PC<sub>71</sub>BM is also included. For all the devices involving in the PC<sub>71</sub>BM annealing optimization, 11 seconds of 100% UV intensity were applied to the PVSK layers.

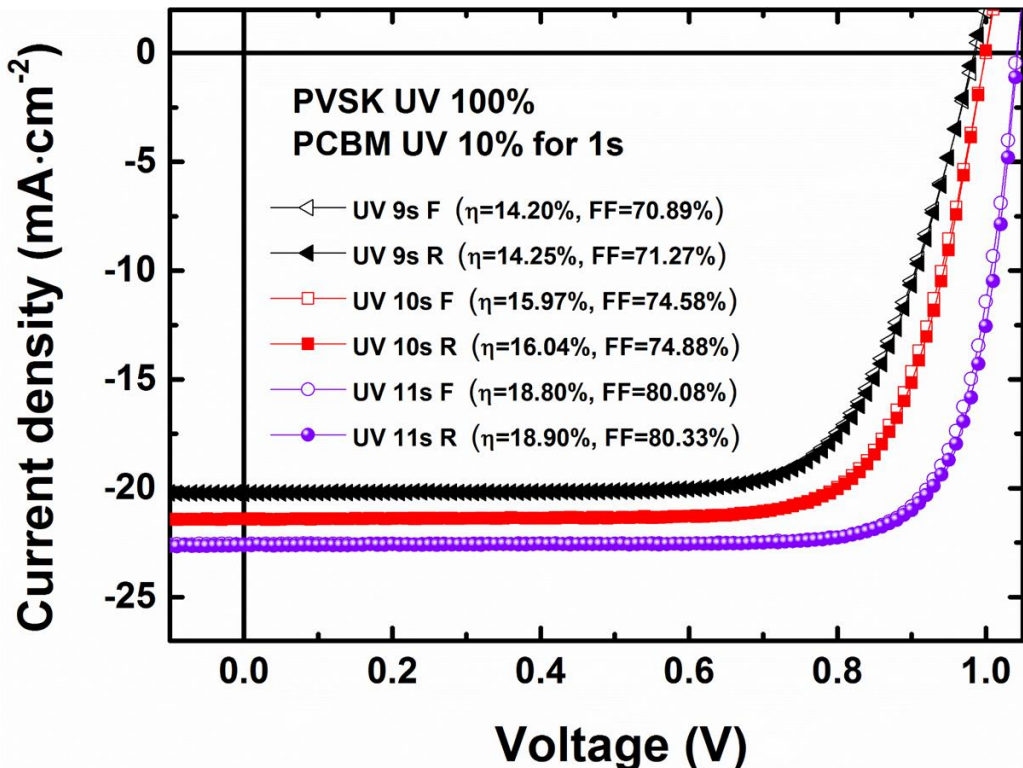


**Figure 25.** Performance comparison between devices with different UV annealing times from 9s to 11s with the same UV annealing condition on the PC<sub>71</sub>BM layer: 10% UV intensity for 1s.

In order to verify and prove that UV annealing of 11s is indeed the optimal condition that not only applies for PVSCs without PC<sub>71</sub>BM UV annealing (**Figure 21b**), but also for solar cells with UV irradiation on PC<sub>71</sub>BM ETL layer, different UV annealing times from 9s to 11s were used on the PVS<sub>K</sub> layer while keeping the same optimized UV condition on the PC<sub>71</sub>BM layer, i.e. 10% UV intensity with an exposure time of 1s. **Figure 25** shows that UV annealing of 11s is apparently the optimal condition for the MAPbI<sub>3</sub> layer in our inverted planar device configuration. A combination of 11s + 100% UV on MAPbI<sub>3</sub> active layer and 1s + 10% UV on the PC<sub>71</sub>BM layer produces the best device performance with averaged PCE of 18.85%, fill factor of 80.21%,  $V_{OC}$  of 1.04 V and  $J_{SC}$  of 22.61 mA cm<sup>-2</sup> from both forward and reverse scans. For comparison, PVSCs were fabricated with thermal annealing at 100 °C for 30 minutes on both the MAPbI<sub>3</sub> and PC<sub>71</sub>BM layers. **Figure 26a** shows comparison between our best thermal-annealed device and champion UV-annealed device. The UV-annealed device demonstrates much better photovoltaic performance than the thermal-annealed counterpart. Detailed PV parameters of related devices are listed in part b of **Table 8**. To the best of my knowledge, PCE of 18.85% is the highest efficiency achieved among the PVSCs with the inverted planar architecture of ITO/PEDOT:PSS/MAPbI<sub>3</sub>/PC<sub>71</sub>BM/Al, and 18.85% is also the highest demonstrated efficiency for any photonic-annealed PVS<sub>K</sub> solar cells reported. **Figure 26b** exhibits the external quantum efficiencies (EQE) and the corresponding integrated short-circuit current densities of the best thermal-annealed device and the champion UV-annealed device. For the UV-annealed device, the EQE of around 90% across the whole visible spectrum yields an integrated  $J_{SC}$  of 22.46 mA/cm<sup>2</sup>, which is very close to the values obtained from J-V measurements (**Table 8** part b). In contrast, the

integrated  $J_{SC}$  of 20.82 mA/cm<sup>2</sup> for the thermal-annealed device is also in good match with the values obtained from J-V measurements (**Table 8** part b). The EQE of the UV-annealed device is universally higher than that of the thermal-annealed device across the entire measured wavelength range, especially from 350 nm to 550 nm and from 700 nm to 750 nm. The EQE data explain why the UV-annealed device is better than their thermal-annealed counterpart, that is, the UV-annealed device is more efficient on either generating or extracting charge carriers than the thermal-annealed device. The EQE measurement is a better indication of the mechanism than other characterization methods such as XRD, UV-Vis and top-view SEM since the EQE is on the device level while other listed methods are just on the film level. For example, larger grain sizes under SEM might explain higher optical absorbance, but cannot guarantee better photovoltaic performance.<sup>[55]</sup> Higher efficiency simultaneously requires better optical and electrical properties. Good optical absorption alone won't warranty better PV performance, as exhibited by thermal-annealed devices in this study. We hypothesize that it is the better balance & coupling between the optical absorption and charge transport that results in the improved PV performance from the UV-annealed devices. **Figure 26c** and **26d** exhibit the performance reproducibility of PVSCs with UV annealing only on the MAPbI<sub>3</sub> active layer and UV annealing on both the MAPbI<sub>3</sub> and PC<sub>71</sub>BM layer, respectively. For PVSCs with UV-LED annealing on both the MAPbI<sub>3</sub> film and PC<sub>71</sub>BM layer, a median efficiency around 17% from 50 devices along with the champion efficiency of 18.85% were accomplished. These efficiencies and reproducibility from high-quality devices are solid evidence for the feasibility of rapid UV-LED-annealing on the PVSK active layer to achieve high-performance PVSK solar cells. To accurately assess

the hysteretic behaviors, the J-V characteristics have been measured at different scan rates of  $0.2 \text{ V s}^{-1}$  and  $0.02 \text{ V s}^{-1}$  in both forward and reverse scanning directions (**Figure 22**). Regardless of scan rate, devices without PC<sub>71</sub>BM annealed exhibit a strong hysteretic effect (**Figure 22a**), while devices with PC<sub>71</sub>BM annealed demonstrate hysteresis-free J-V curves (**Figure 22b**). This is a clear evidence that UV annealing of charge transport layer is capable of and effective at eliminating the hysteresis.<sup>[117]</sup>

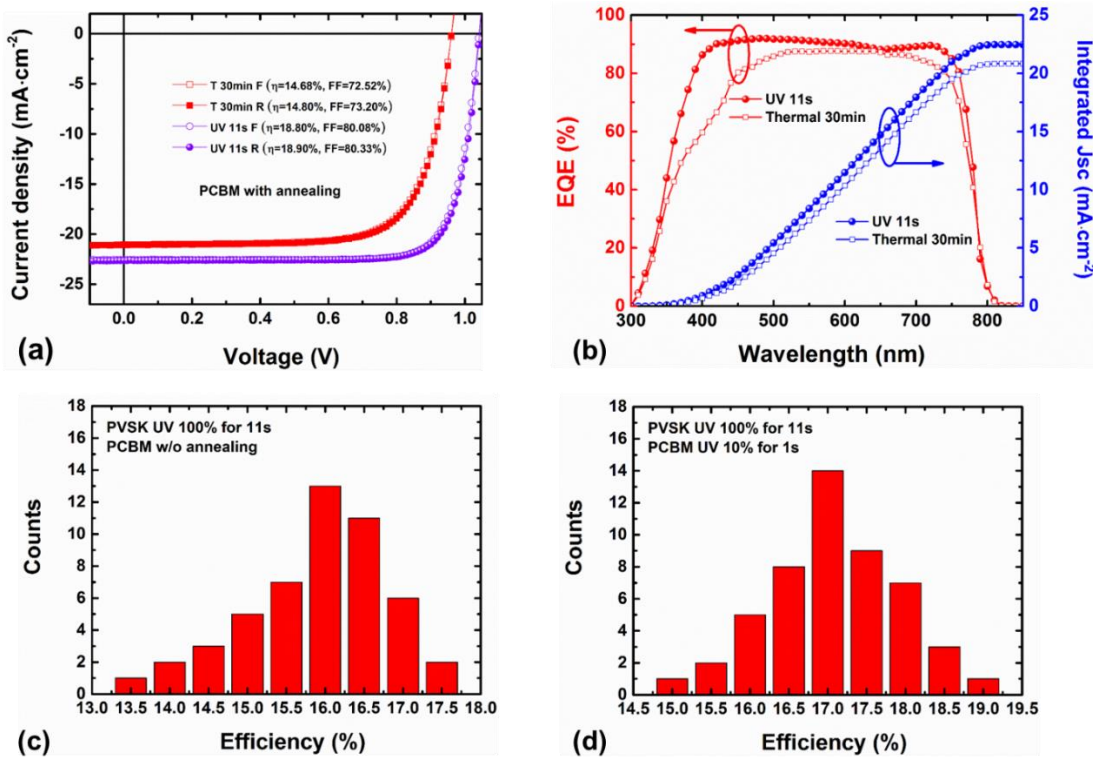


**Figure 26.** a) Hysteresis-free J-V characteristics of PVSCs with both PVK and PC<sub>71</sub>BM annealed (either UV-annealed or thermal-annealed); b) EQEs and integrated  $J_{scs}$  of the best thermal-annealed PVSC and the champion UV-annealed PVSC. Histograms of c) PVSCs (50 devices) with UV annealing of 11s (100% intensity) on the MAPbI<sub>3</sub> layer but no UV annealing on the PC<sub>71</sub>BM layer, and d) PVSCs (50 devices) with UV annealing of 11s (100% intensity) on the MAPbI<sub>3</sub> layer and UV annealing of 1s (10% intensity) on the PC<sub>71</sub>BM layer.

#### **4.2.4 Characterization of PVK Thin Films for Comparison in Performance**

It is crucial to have high-crystalline PVSK films with uniform and flat surface topography for attaining high-performance devices. In this study, DMSO and a Toluene-assisted anti-solvent wash were adopted to facilitate the formation of high-quality  $\text{MAPbI}_3$  films during spin-coating process. The XRD measurements (**Figure 27**) show that UV annealing of 7s is sufficient to transform  $\text{MAI-PbI}_2\text{-DMSO}$  adduct into  $\text{MAPbI}_3$  films. However, UV annealing of 7s is not enough to grow  $\text{MAPbI}_3$  films with device-level quality. The thermal-annealed samples and UV-annealed samples show similar XRD patterns, meaning that both of them have formed  $\text{MAPbI}_3$  with comparable crystallinities. These XRD results prove that if the dosage is well-managed, UV irradiation is as capable as thermal energy for turning PVSK precursors into  $\text{MAPbI}_3$  crystal. In the optical aspect, the PVSK film with UV annealing of 7s has the lowest overall UV-Visible (UV-Vis) absorption spectrum (**Figure 28**). With increasing UV annealing time, the PVSK films demonstrate better UV-Vis absorption, but still not as high as that of the sample with 30 minutes of thermal-annealing. This trend matches well with the colors of the films from different annealing conditions. The film with UV annealing of 7s exhibits only light-brown color, as compared to the dark-brown color induced by UV-annealing for 9s & above and thermal-annealing for 30 minutes. All of the UV-annealed films are not as dark as the thermal-annealed film (30 minutes). Although the difference in the UV-Vis results seems apparent, it should be noted that all of the films have good absorption since the absorbance values of 1, 2, 3, and 4 correspond to absorption rates of 90%, 99%, 99.9% and 99.99%, respectively in the **Figure 28**. The thickness of the PVSK layer is the same (~ 400nm, **Figure 23**), indicating

that the difference should be originating from the extinct coefficients of films with varied annealing conditions. Top-view SEM images (**Figure 29**) of PVK films with different UV annealing times from 0s to 13s are compared to that of the thermal-annealed film (100 °C for 30 minutes). All of the UV-annealed films demonstrate uniform morphology with densely packed domains without any void sites. The PVSK film with 11s (versus 9s) of UV annealing shows observable growth of grain sizes. Correlating to the improvement of the photovoltaic performance (**Figure 21b**), it is obvious that increasing the UV energy to this level is still beneficial for the crystal formation of high-quality MAPbI<sub>3</sub> PVSK films. The 13s film displays charge-accumulation islands (white spots) all over the film, indicating that this level of UV irradiation is over dosed and has already damaged the PVSK film, with some non-conduction precipitates generated. In fact, the MAPbI<sub>3</sub> films start to have a weak color change to lightly-whitish beginning with 13s of UV irradiation, suggesting a higher-than-necessary level of energy applied for the crystallization of MAPbI<sub>3</sub> films. The thermal-annealed PVSK films have larger grain sizes and higher light absorption than UV-annealed films, but they show lower short-circuit current ( $J_{SC}$ ). Tsai et. al. found that light-soaking after thermal-annealing can increase the device efficiency because of reduced non-radiative recombination.<sup>[70]</sup> We predict that UV annealing of the PVSK active layer may have similar or even better effects on suppressing recombination and enhancing charge transport. This is evidenced by the much enhanced short-circuit current ( $J_{SC}$ ), open-circuit voltage ( $V_{OC}$ ) and fill factor ( $FF$ ) of the UV-annealed samples as compared to that of their thermal-annealed counterparts in **Figure 21a**, since these parameters are good indicators for charge recombination and transport.<sup>[118]</sup>

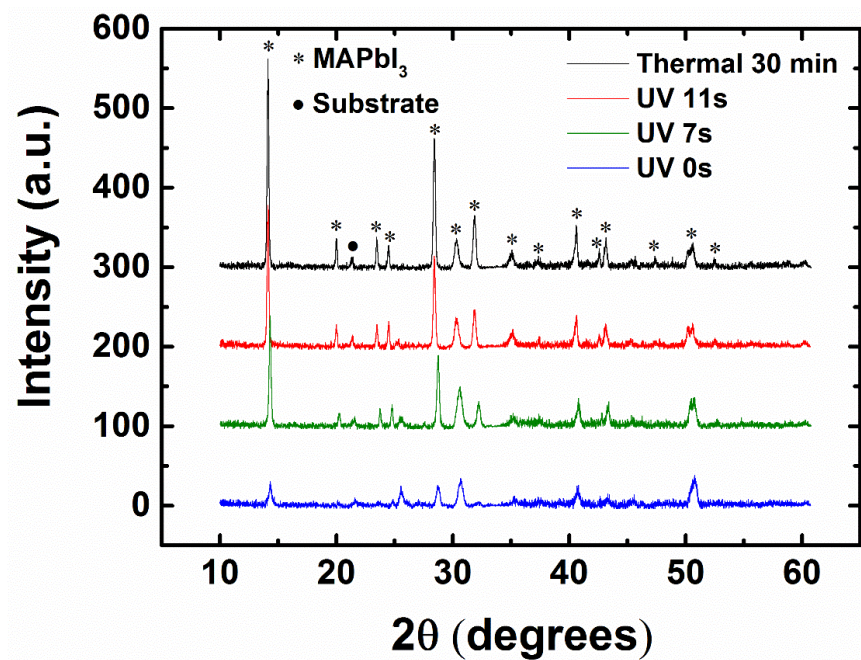


**Figure 27.** XRD characterization of perovskite thin films thermal-annealed at 100 °C for 30 minutes and UV-annealed samples with different irradiation times from 0s to 11s.

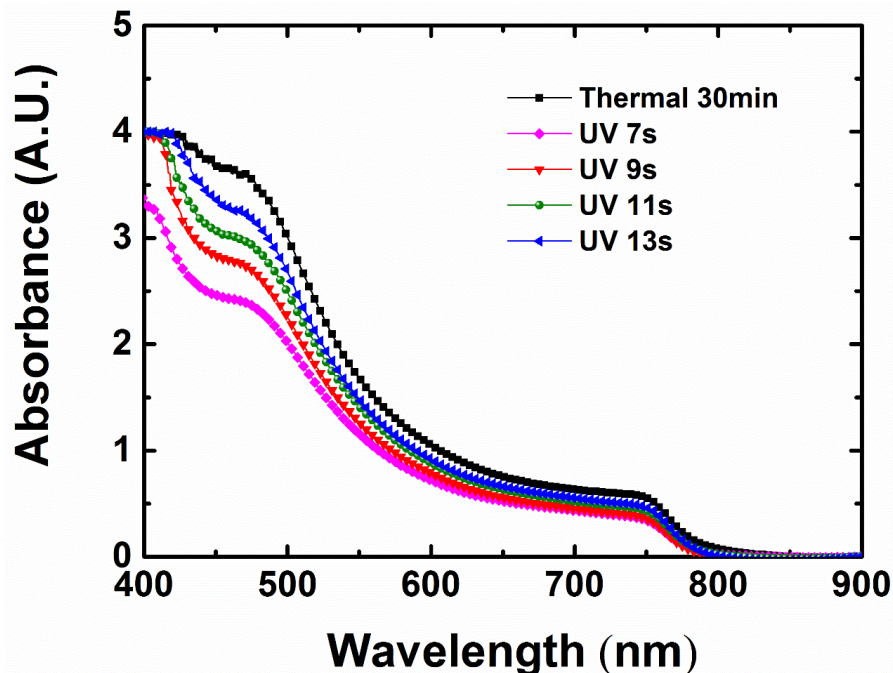


**Figure 28.** UV-Vis spectrum of perovskite thin film thermal-annealed at 100 °C for 30 minutes and UV-annealed samples with different illumination times from 7s to 13s.

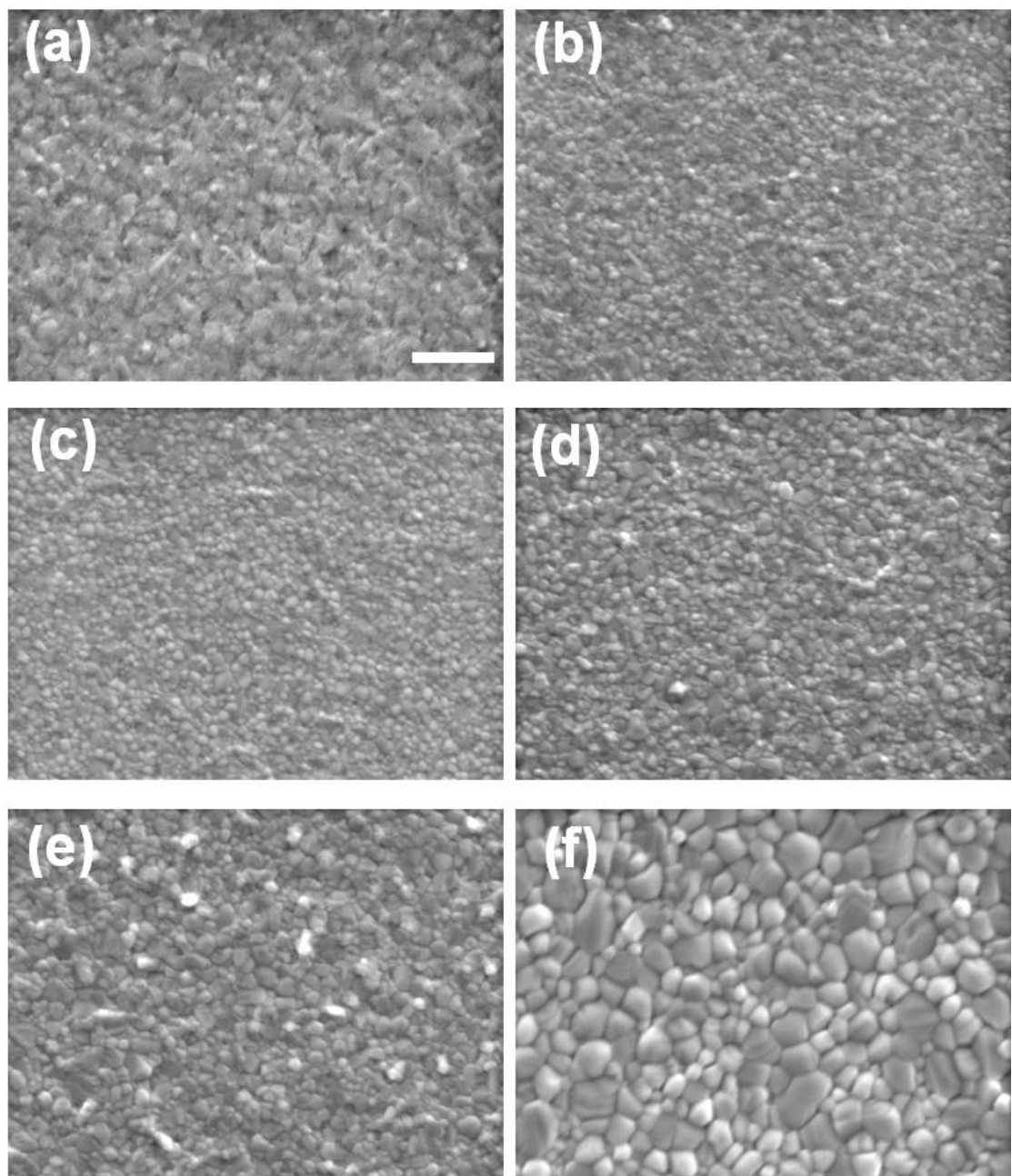


**Figure 29.** Top-view SEM images of a) non-annealed MAI-PbI<sub>2</sub>-DMSO film, b)-e) MAPbI<sub>3</sub> films with varied UV annealing times of 7s, 9s, 11s & 13s, and f) MAPbI<sub>3</sub> film with thermal-annealing at 100 °C for 30 minutes. The scale bar is 1 micrometer. All PVS<sub>K</sub> films are deposited on the PEDOT:PSS/ITO/glass substrates.

#### 4.2.5 Deposition energy of PVK Films

In addition to being an efficient tool for the creation of high-quality  $\text{MAPbI}_3$  films, this absorption-based UV-LED-annealing also allows calculation of the deposition energy required for the  $\text{MAPbI}_3$  PVSK films to reach a device-quality level. This deposition energy could serve as a characteristic parameter in evaluating the quality of PVSK films, since it is, in essence, the energy rather than the temperature that crystallizes the PVSK films. The absorption of light propagating through a material can be calculated by the equation  $A(k, z) = 1 - \exp(-4\pi kz/\lambda)$ , where  $k$ ,  $z$  and  $\lambda$  are the extinction coefficient, thickness of the material and wavelength of the light, respectively. The total energy being absorbed by the material can be denoted as  $E = S \times \int A(k, z) \times I dt$ , where  $S$ ,  $I$  and  $t$  are the area of the device, UV irradiance and time of UV exposure, respectively. If the absorption  $A(k, z)$  is nearly a constant ( $A$ ) and the UV irradiance  $I$  is independent of the time  $t$ , the total absorbed energy can be simplified to the form  $E = S \times A \times I \times t$ . This is indeed the case of the  $\text{MAPbI}_3$  layer, explained as follows. The  $k$  value is obtained from reference<sup>[108]</sup> and the thickness of  $\sim 400$  nm is measured from the cross-sectional SEM image shown in **Figure 23**. For the UV light of 365-nm wavelength, the absorption  $A(k, z)$  of the  $\text{MAPbI}_3$  film is calculated to be  $> 99.99\%$ , which is an almost-full absorption ( $A = 1$ ). The UV LED employed in this study offers a maximal output of  $24 \text{ W cm}^{-2}$  (at zero distance), which equates to the intensity of 240 suns at AM 1.5 condition but with pure UV light. During the experimental procedure, the distance between the target and the UV source is kept at 15 mm for a larger illumination area. At this distance, the corresponding irradiance  $I$  is measured to be  $2.22 \text{ W cm}^{-2}$  using a UV radiometer calibrated at 365 nm. This intensity level does not

depend on time as it is uniformly maintained over the entire device area during the whole UV annealing process. Our single device has an active area of  $0.142 \text{ cm}^2$ , precisely measured by counting the pixels through software ImageJ. With the density of  $4.286 \text{ g cm}^{-3}$  and molar mass of  $620 \text{ g mol}^{-1}$ , the mass and the molar amount of  $\text{MAPbI}_3$  in a device (volume of  $400 \text{ nm} \times 0.142 \text{ cm}^2$ ) are  $2.43 \times 10^{-5} \text{ g}$  and  $3.93 \times 10^{-8} \text{ mol}$ , respectively. The absorbed UV energy can be calculated as the product of the device area of  $0.142 \text{ cm}^2$ , the absorption of  $A = 1$ , the irradiance of  $2.22 \text{ W cm}^{-2}$  and the illumination time of  $11\text{s}$ , resulting in a value of  $3.47 \text{ J}$ . If this amount of energy is completely used for crystal formation, the deposition energy needed for the  $\text{MAPbI}_3$  film to reach a quality necessary for high-performance devices is  $1.43 \times 10^5 \text{ J g}^{-1}$  or  $8.83 \times 10^7 \text{ J mol}^{-1}$ . In terms of the thermal effect, it is speculated that there was no obvious temperature increase in the PVK film during the UV annealing. It is hard to monitor the temperature inside the  $\text{MAPbI}_3$  film or the substrate during the UV annealing, since the UV-exposure time is too short. However, the minimum energy required to heat certain amount of the related substances including glass, ITO, PEDOT:PSS and  $\text{MAPbI}_3$  materials together to a temperature can be estimated using equation  $Q = (C_p DV \Delta T) / (DV) = C_p \Delta T$ , where  $C_p$ ,  $D$ ,  $V$  and  $\Delta T$  are the specific heat, density, volume, and the temperature increased value, respectively. The volume is the product of thickness  $z$  and device active area  $S$ . The relevant physical properties of various materials are listed in

**Table 9.** Assuming an average specific heat capacity of  $1 \text{ J g}^{-1} \text{ K}^{-1}$ , the minimum energy will be  $100 \text{ J g}^{-1}$  for increasing the temperature of  $\Delta T = 100 \text{ K}$ , which is an extreme case.

Compared with the absorbed photonic energy, this  $100 \text{ J g}^{-1}$  is completely negligible. In other words, the thermal effect of the UV annealing is trivial unless the temperature is increased by

more than 10,000 K, which is impossible and not realistic. Therefore, in theory, the deposition energy of the MAPbI<sub>3</sub> PVSK film is very close to  $1.43 \times 10^5$  J g<sup>-1</sup> or  $8.83 \times 10^7$  J mol<sup>-1</sup>.

**Table 9.** Physical properties of materials for different layers.

Materials	Specific heat $C_p$	Density $D$	Thickness $z$	Extinct Coeff. @ 365nm
Unit	$J\ g^{-1}\ K^{-1}$	$g\cdot cm^{-3}$	$10^{-7}cm$	unitless
CH <sub>3</sub> NH <sub>3</sub> PbI <sub>3</sub>	0.3035	4.286	400	1.34757
PEDOT:PSS	1.19	1.270	25	N/A
ITO	1	1	150	N/A
SiO <sub>2</sub> glass	0.84	2.2	$10^6$	N/A

As mentioned before, the calculated theoretical energies are only valid if the film under UV annealing has a constant absorption ( $A = 1$ ) throughout the entire UV annealing time. However, while annealing, the PVSK film underwent a conversion from MAI-PbI<sub>2</sub>-DMSO adduct to MAPbI<sub>3</sub> crystal. The change of absorption  $A$  with time during the entire UV annealing process needs to be found before the theoretical calculated energies can be validated. **Figure 30a** illustrates a schematic of the UV transmission study including cleaned ITO/glass substrate, PEDOT:PSS-coated ITO/glass and MAI-PbI<sub>2</sub>-DMSO/PEDOT:PSS/ITO/glass. The values of transmission intensities were monitored using the UV radiometer through an 11s irradiation period, as shown in **Figure 30b**. The UV source intensity is the irradiance measured at 15 mm from the UV LED source. This intensity level is set as the benchmark and labeled as 100% in **Figure 30a**. It can be seen that the transmission through a bare ITO-glass substrate is 93.3%. The UV source intensity (100%)

has been attenuated by less than 6.7%, indicating a great transparency of ITO-glass to the 365-nm UV light. It is interesting that coating a thin layer of PEDOT:PSS does not further decrease the transmitted UV intensity, but actually increases it slightly to 93.9%. It is speculated that this thin layer of PEDOT:PSS does not absorb the incident UV light, but rather slightly enhances the anti-reflectivity of the ITO-glass, resulting in an overall increase of light transmission. The MAI-PbI<sub>2</sub>-DMSO deposited on PEDOT:PSS/ITO/glass under 11s of UV irradiation is in fact the UV annealing process itself. It can be seen that in the first 3 seconds (**Figure 30b**), a tiny amount of light passed through the PVSK film. The maximum transmission of 1.73% (**Figure 30a**) occurs at the very beginning, corresponding to the MAI-PbI<sub>2</sub>-DMSO adduct in the UV annealing process. As shown in **Figure 30b**, the transmission intensity quickly drops below 1% in the first 3s and finally reaches 0.09% at the end of the 11s duration, when the film is already complete MAPbI<sub>3</sub>. In addition, the reflection of UV light was also monitored during 11-second UV annealing of the PVSK film. The results show that the reflecting UV intensity was so low that it is trivial, regardless of measuring angle (direction). With negligible reflection, the actual absorption of the PVSK film (first adduct and then MAPbI<sub>3</sub>) can be obtained by comparing the transmission data through different structures. In specific, the transmission difference between the PEDOT:PSS/ITO/glass (93.9%) and MAI-PbI<sub>2</sub>-DMSO/PEDOT:PSS/ITO/glass (1.73%) can be seen as the absorption of the MAI-PbI<sub>2</sub>-DMSO adduct. Its value is 93.9% minus 1.73%, giving the MAI-PbI<sub>2</sub>-DMSO adduct film an absorption *A* greater than 92%. Similarly, the absorption of the MAPbI<sub>3</sub> film can be acquired by subtracting the transmission of the MAPbI<sub>3</sub>/PEDOT:PSS/ITO/glass (0.09%) from the transmission of the PEDOT:PSS/ITO/glass

(93.9%), yielding an absorption  $A$  just under 94%. Thus, the real absorption  $A$  of the PVS<sub>K</sub> film during the 11s of UV annealing is in the range from 92% to 94% with an average around 93%. This indicates the absorption of the MAI-PbI<sub>2</sub>-DMSO adduct film is almost the same as that of the crystallized MAPbI<sub>3</sub> film for the UVA light utilized in this study. Therefore, it is safe to conclude that the absorption of the PVS<sub>K</sub> film can be approximated as a constant throughout the entire UV annealing time. Although this value is not the same as the 100% in the theoretical calculations, the prior method of estimating the deposition energy of the MAPbI<sub>3</sub> film remains valid, only with the absorption value now being another constant  $A = 93\%$ . As a result, the more accurate deposition energy of MAPbI<sub>3</sub> film required for achieving a high-performance PVSC device is adjusted from  $1.43 \times 10^5 \text{ J g}^{-1}$  ( $8.83 \times 10^7 \text{ J mol}^{-1}$ ) to  $1.33 \times 10^5 \text{ J g}^{-1}$  ( $8.21 \times 10^7 \text{ J mol}^{-1}$ ). Earlier, the theoretical absorbance calculation predicted that the MAPbI<sub>3</sub> film would absorb 99.99% of the incident UV light. In reality, however, experimental transmission measurements showed that the MAPbI<sub>3</sub> film only absorbed 92% to 94% of the light. This is because, like any other LED source, the employed UV LED does not emit light with an absolutely single wavelength. As shown in **Figure 30a**, the radiation released from the UV LED has a peak wavelength of 365 nm with wavelength edges extending to 350 nm in the deeper UV direction and to over 380 nm in the visible direction. Specifically, there is a tiny portion of visible light included in the irradiation from the UV LED source. This visible light accounts for the 1.73% transmission through the visually transparent MAI-PbI<sub>2</sub>-DMSO adduct film and the 0.09% transmission through the dark-brown MAPbI<sub>3</sub> film. Also, it is worth noting that UV intensity can be increased much higher (up to  $24 \text{ W cm}^{-2}$ ) if the source-target distance is reduced. With higher UV intensity,

the UV annealing time can be significantly shortened. In our experiment, the optimized UV exposure time of 11 seconds is based on a UV intensity of  $2.22 \text{ W cm}^{-2}$ , which is the direct consequence of the 15-mm source-target distance. The illumination height of 15-mm from target was chosen to uniformly cover the PVSK active area due to the limitation of our LED UV light source. If a high-intensity UV LED array is used, the annealing time could be further dropped even below 1 second, which will be a perfect match for large scale roll-to-roll manufacturing. After all, no matter what intensity (and consequent annealing time) is implemented, the gravimetric and molar energy should remain identical for the same PVSK material to reach the same level of film quality.

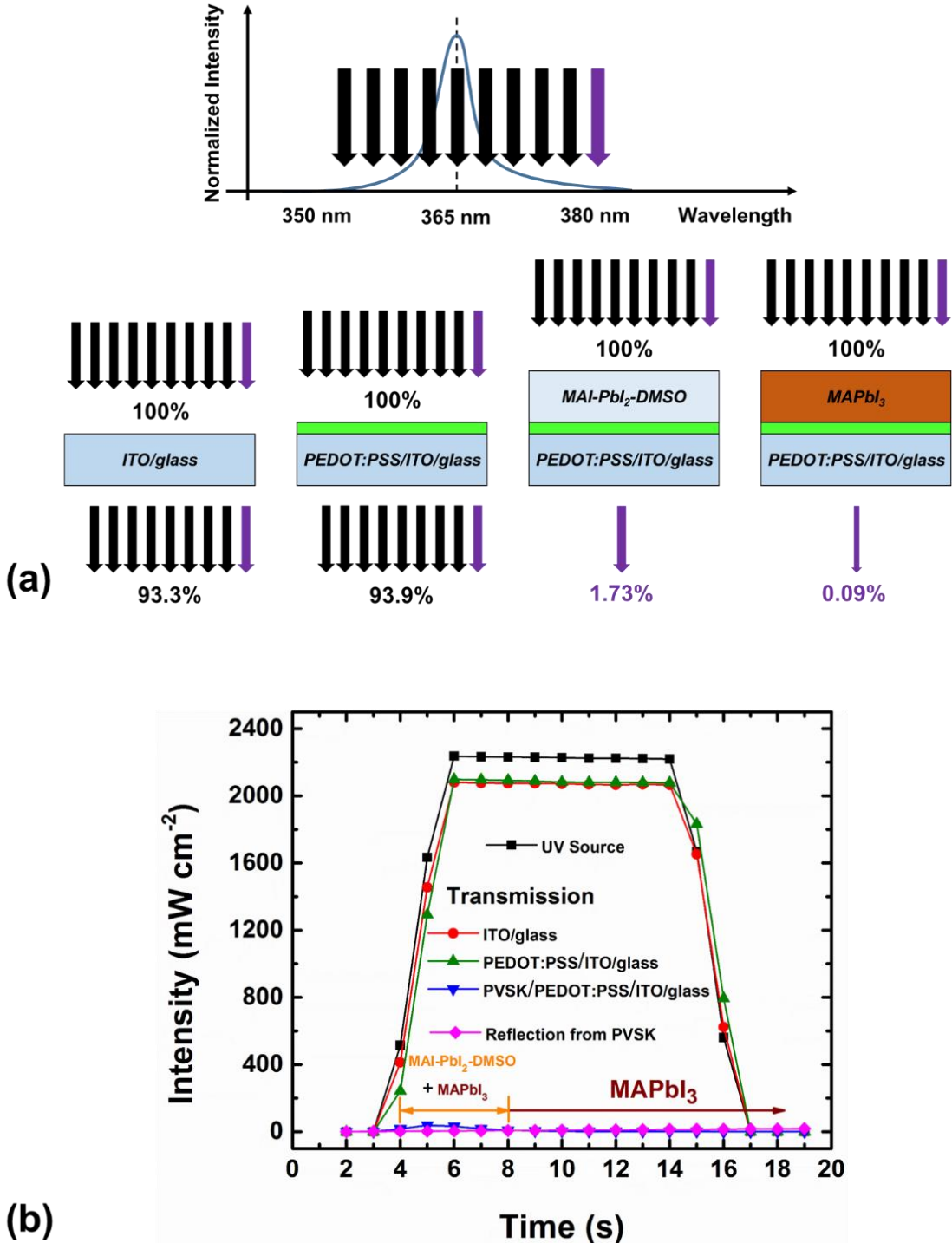


**Figure 30.** a) Schematic of transmission measurement through different layers, including cleaned ITO/glass, PEDOT:PSS/ITO/glass, and the conversion of MAI-PbI<sub>2</sub>-DMSO to MAPbI<sub>3</sub> on top of PEDOT:PSS/ITO/glass. The UV source intensity is labeled as 100% as benchmark for all the transmission percentage denotation. And b) transmission & reflection intensities during 11 seconds of UV irradiation. The PVSK layer underwent a transformation from MAI-PbI<sub>2</sub>-DMSO adduct to MAPbI<sub>3</sub> during this 11-second period.

## **CHAPTER 5. TOWARDS SCALABLE PEROVSKITE SOLAR MODULES USING BLADE-COATING AND RAPID THERMAL PROCESSING**

The power conversion efficiency (PCE) of perovskite solar cells (PVSCs) has rapidly increased from 3.8% to more than 25.2% in the past decade.<sup>[44-46, 119]</sup> So far, all the PVSCs that broke the world-record of efficiency have active area smaller than 0.1 cm<sup>2</sup>. Small active areas are commonly adopted world-wide in scientific demonstration and technology development for one reason: it is much simpler to maintain the uniformity of the coated films across a small area therefore much easier to achieve a better efficiency. Small active area can only be used for demonstration of performance possibilities, but beyond that has no practical use. There are two main factors that limit the upscaling of PVSCs. One is the coating technique and the other is the annealing process. The most prevalent methods for coating and annealing are spin-coating and convective thermal annealing (i.e. hot-plate), respectively. These approaches are dependable but could never easily be scaled-up to module size areas. Advanced coating and annealing practices should be adopted to obtain uniform and good quality films on large areas.

Among scalable printing technologies, blade-coating has been demonstrated to be successful in perovskite photovoltaics.<sup>[55, 120-121]</sup> Blade-coating provides advantages such as capability of processing a wide range of fluids with high and low viscosity.<sup>[122]</sup> Moreover, blade-coating is a great step up from spin-coating towards ultimate roll-to-roll (R2R) deposition with slot-die coating.<sup>[123-124]</sup> In addition, blade-coating is more suitable in the lab-scale compared to the slot-die coating because the former will not have to deal with the dead-

volume like the latter thus will consume less ink in small batches.<sup>[125]</sup> In order to realize large-scale manufacturing of PVSCs, traditional annealing methods like hot-plate annealing should be avoided since they are energy-inefficient and time-consuming (at a time scale of minutes or an hour), which will impede the high-speed character of blade-coating, or any other R2R printing technique.<sup>[57-67]</sup> Nevertheless, annealing processes other than hot-plate annealing continue to be explored. Microwave radiation was utilized to anneal mixed-halide perovskites  $\text{CH}_3\text{NH}_3\text{PbI}_{3-x}\text{Cl}_x$ . Xu et al. showed an annealing time of 6 minutes resulting in devices with a PCE of only 10.29%.<sup>[126]</sup> Wang et al. demonstrated post-annealing microwave treatment also on  $\text{CH}_3\text{NH}_3\text{PbI}_{3-x}\text{Cl}_x$  and improved the efficiency to 13.39%.<sup>[127]</sup> Three minutes of microwave irradiation was cast on  $\text{CH}_3\text{NH}_3\text{PbI}_3$  ( $\text{MAPbI}_3$ ) perovskite films to fabricate PVSCs with PCEs up to 14.91%.<sup>[128]</sup> In addition to the low efficiencies, the microwave-annealing is likely not compatible with the R2R printing since it requires a closed environment to confine the microwave energy. Near-infrared (NIR) laser was used to crystallize  $\text{MAPbI}_3$  perovskite films, leading to a device PCE of 11.3%.<sup>[129]</sup> A 450-nm laser was adopted to anneal  $\text{MAPbI}_3$  perovskite films, resulting in an optimal efficiency of 17.8%.<sup>[130]</sup> Laser-annealing was claimed to achieve faster crystallization of perovskite films than the thermal annealing, but it is difficult to be scaled-up due to slow raster scan rate thereby small area coverage. Flash lamp annealing was demonstrated on  $\text{MAPbI}_3$  perovskite films with an annealing time of less than 3 ms by using a high energy xenon light. In terms of X-ray diffraction (XRD) results, this flash xenon light produced films with better crystallinity than the conventional thermal annealing, but no device was made.<sup>[131]</sup> Also with a xenon lamp, Troughton et al. demonstrated a PCE of 11.3% by flash-annealing  $\text{CH}_3\text{NH}_3\text{PbI}_{3-x}\text{Cl}_x$ .

perovskite films in 1 milliseconds (ms).<sup>[72]</sup> Lavery et al. pulse-annealed MAPbI<sub>3</sub> thin films within 2 ms via intense light irradiated from a xenon lamp. The consequential devices exhibited PCEs up to 12.3%, which is similar to those of their thermally-annealed samples.<sup>[73]</sup> With the help of intense pulsed xenon light and diiodomethane additive, Ankireddy et al. were able to fabricate MAPbI<sub>3</sub>-based PVSCs with a device efficiency of 16.5%.<sup>[132]</sup> Compared with the above-mentioned photonic annealing methods, rapid thermal processing (RTP, also known as rapid thermal annealing, RTA) is a widely used technique in industry for processing semiconductors.<sup>[133]</sup> Sanchez et al. applied RTP annealing to inorganic mixed-halide CsPbI<sub>x</sub>Br<sub>3-x</sub> perovskite films, achieving PCE over 10%.<sup>[134]</sup> With 40 s of RTP, Pool et al. attained PCE of 14.15% on inorganic formamidinium lead iodide (FAPbI<sub>3</sub>) perovskite films, comparable to the efficiency of 13.80% from hot-plate annealing.<sup>[74]</sup> Park et al. annealed mixed-cation (MAPbI<sub>3</sub>)<sub>0.85</sub>(FAPbI<sub>3</sub>)<sub>0.15</sub> perovskite layer by RTP at 120 °C for 10 minutes under N<sub>2</sub> atmosphere. Their device PCE surpassed 17% but accompanied by a low fill factor (FF) of 68%.<sup>[135]</sup> With 3 min of RTP in nitrogen, Dou et al. managed to make MAPbI<sub>3</sub>-based PVSCs with PCE of 18.0%.<sup>[136]</sup> All the aforementioned researches employed small device area (0.1 cm<sup>2</sup> or smaller), it was not until recently that larger device area has been implemented with radiative annealing. RTP annealing has been shown to work on both the MAPbI<sub>3</sub> and triple-cation mixed-halide (MAFACsPbIBr) perovskite layers, producing PVSCs with active area of 1.4 cm<sup>2</sup>. The corresponding PCEs have been reported to reach 14.6 % with FF of 69.8% and ~ 15.0% with FF of ~ 61%, respectively.<sup>[137-138]</sup> Compared with their small devices, both the efficiency and FF dropped considerably. Although RTP appeared functioning on perovskite films, none of the aforesaid investigations went beyond spin-

coating for deposition of perovskite active layer. So far, only Breuning et al. combined the blade-coating with RTP to manufacture PVSCs in helium. Their champion device displayed a PCE of 16.8% with an active area of  $0.1\text{ cm}^2$ .<sup>[139]</sup>

In this chapter, blade-coating and RTP have been used to fabricate planar p-i-n PVSCs and modules. The PVSCs made from RTP for less than 30 seconds have equivalent photovoltaic performance as devices fabricated from hot-plate annealing for 2 minutes. The RTP method successfully decreases the annealing time of blade-coated  $\text{MAPbI}_3$  films by more than four-fold as compared to the conventional thermal annealing. The resulting small devices with an active area of  $0.105\text{ cm}^2$  show a best average PCE over 18.47% from forward and reverse scans. Mini-modules with an active area over  $2.7\text{ cm}^2$  exhibit a champion average PCE over 17.73% from forward and reverse scans. To the best of my knowledge, these efficiencies are the highest for PVSCs processed by the combination of blade-coating and RTP. Furthermore, high fill factors have been achieved, with average values of 79.90% and 74.77% for the small device and mini-module, respectively. In addition, both the blade-coating and RTP were performed in ambient environment. These results justify the feasibility of RTP for the upscaling fabrication of PVSCs. Although blade-coating and RTP have been proven to be effective in the lab scale, more advanced methods such as slot-die coating and LED annealing are required in order to realize R2R printing and large-scale production of PVSCs.

## 5.1 Experimental Section

Materials preparation: Poly(triary amine) (PTAA) were purchased from Sigma-

Aldrich. Lead iodide ( $\text{PbI}_2$ , 99.9985%) and methylammonium iodide (MAI) was acquired from Alfa Aesar and Greatcell Solar respectively. Methylammonium chloride (MACl, >98.0%) and Bathocuproine (BCP, >99.0%, sublimed) were obtained from TCI. Poly [(9,9 - bis(3' - (N,N - dimethylamino)propyl) - 2,7 - fluorene) - alt - 2,7 - (9,9 - dioctylfluorene)] dibromide (PFN-Br) was ordered from 1-Material. Fullerene C60 (>99.5%) was purchased from Lumtech. All solvents, such as toluene, methanol, N,N - dimethylformamide (DMF), Dimethyl sulfoxide (DMSO), N-Methyl-2-pyrrolidone (NMP), were purchased from Sigma-Aldrich in anhydrous grade.

Device fabrication: The ITO-glass were cut into 1-inch wide slides, which were ultrasonically brushed with Liquinox detergent solution (Liquinox : DI water = 1 : 20), then rinsed with DI water thoroughly. After  $\text{N}_2$ -blow drying, the cleaned ITO-glass slides substrates were treated by the UV-Ozone for 15min and then used immediately for sequential coating of different layers. All the blade-coating, hot-plate annealing and RTP were performed in ambient environment. Regardless of solution type, 20  $\mu\text{L}$  of solution were applied for a substrate with dimension of 1 inch x 5 inches. PTAA was dissolved in toluene to form a 10mg/ml solution. PTAA layer was blade-coated with a gap height  $\sim$  100  $\mu\text{m}$  at a coating speed of 10 mm/s and then annealed at 100  $^{\circ}\text{C}$  for 10 minutes. After PTAA layer, PFN in methanol (0.4mg/ml) was employed to modify the hydrophobicity of PTAA.<sup>[140]</sup> PFN was blade-coated with the same coating parameters but no annealing. On top of PFN layer, the perovskite layer was blade-coated with a gap height  $\sim$  150  $\mu\text{m}$  at a coating speed of 7.5 mm/s. Perovskite precursor solution was composed of 1.2M MAI, 1.2M  $\text{PbI}_2$ , and 0.06M MACl in a mixed solvent (DMF:DMSO:NMP = 0.91:0.07:0.02 volume ratio). No anti-

solvent was used. Instead, an air-knife was employed to pre-dry the blade-coated perovskite films before annealing of any kind. The ITO-glass slides were further cut into 1x1 inch<sup>2</sup> substrates. For the control sets, perovskite films were annealed at 140 °C for 2 minutes on a hot plate. For the RTP samples, different RTP conditions were utilized as outlined in **Table 10**. The RTP instrument was a commercial Ulvac MILA-3000 minilamp Annealer. The thermocouple inside the RTP instrument is attached to a piece of silicon. Samples were floating above the silicon piece without any physical contact, meaning that the measured temperature was not necessarily the same as the actual temperature of the sample. After annealing, the 1x1 inch<sup>2</sup> substrates were loaded into a thermal evaporator for consecutive deposition of C<sub>60</sub>, BCP and silver, with thicknesses of 30 nm, 6 nm and 100 nm, respectively.

Characterization: The X-ray diffraction (XRD) data were measured by a Bruker D8 Discover X-ray diffractometer. UV-Visible (UV-Vis) spectrophotometer (Cary 6000-i) was used to collect the absorption spectra. The top-view SEM images were recorded using a JEOL 7000 field-emission scanning electron microscope (SEM). The *J-V* curves were measured by a Class AAA solar simulator with a Xe-arc lamp and AM1.5G filter from PV measurement, and illumination intensity was calibrated with a NREL certified Si reference cell. Monochromator (Newport 74100) and optical power meter (Newport 70310) were utilized to measure the external quantum efficiency (EQE) with a xenon lamp (Newport 66902) and a Si detector (Newport 71640).

## 5.2 Results and Discussion

### 5.2.1 Thermal Budget of RTP on Perovskite Layer

The annealing effect of RTP on the PCE of PVSCs was investigated methodically. In order to explore the thermal budget of RTP, planar p-i-n PVSCs with a structure of ITO/PTAA/PFN/MAPbI<sub>3</sub>/C<sub>60</sub>/BCP/Ag were fabricated. **Figure 31** shows the trends of photovoltaic parameters of PVSCs based on both hot-plate-annealed MAPbI<sub>3</sub> films and RTP-annealed MAPbI<sub>3</sub> films with different RTP temperatures and time. The photovoltaic parameters have been extracted directly from J-V characteristics, including PCE, fill factor (*FF*), short-circuit current density (*J<sub>SC</sub>*) and open-circuit voltage (*V<sub>OC</sub>*). The detailed photovoltaic values have been summarized in **Table 10**. The reference PVSC contains the MAPbI<sub>3</sub> layer hot-plate-annealed at 140 °C for 2 minutes (120 s). In contrast, the trends of RTP at 110 °C and 140 °C are included in **Figure 31** for side-by-side comparison with the hot-plate annealing. It can be seen that regardless of temperature, there are PCE peaks for RTP as function of the annealing time. For RTP at 110 °C the highest PCE occurs at 30 s of annealing time, with a value of 15.14%. On the other hand, 20 s of annealing appears the best for RTP at 140 °C, with a PCE of 14.93%. The *FFs*, *J<sub>SC</sub>* and *V<sub>OC</sub>* all follow the same trend as that of PCEs for both RTP temperatures, drastically change in the range between 5 s and 120 s. With a fixed RTP temperature, variation of RTP time is equal to changing of energy supply to crystallization and formation of perovskite films. Time scale of 120 s might not be overwhelming for hot-plate annealing but is certainly too long in the case of RTP. Thus, it is not hard to understand the observed substantial effects of RTP temperatures and time on the photovoltaic performance. Unlike the PCE and *FF*, both *J<sub>SC</sub>* and *V<sub>OC</sub>* see trends

with obvious plateaus, especially with  $V_{OC}$ , between 30 s and 120 s. A PVSC is first a diode, once the diode is formed, the voltage response is not expected to change radically. For both RTP temperatures in **Figure 31**, annealing time of 5 s or 10 s are not sufficient to form high-quality perovskite films that are good enough for devices. On contrary, annealing time over 60 s is apparent more than the perovskite films can handle, resulting in considerable degradation on the device performance. More trends have been plotted in **Figure 32** using the data from **Table 10**, with fixed RTP time (5 s, 10 s and 20 s) but varying RTP temperature. With decreasing RTP time, it is clear that elevated temperatures are needed for the peak PCEs, from 140 °C at 20 s to 200 °C at 5 s. These results are solid evidence that it is the annealing energy rather than RTP temperature or RTP time alone that determines the annealing process. Energy amount less than necessary is not able to completely anneal perovskite films. Excessive amount of energy will degrade perovskite films and energy overdose will eventually create films that have poor quality and show inferior performance. The highlighted (dashed line) section in **Table 10** outlines those RTP conditions that can over-anneal  $\text{MAPbI}_3$  films, i.e. turn film color to yellow, indicating decomposing of  $\text{MAPbI}_3$  into  $\text{PbI}_2$ . The hot-plate control PVSC shows PCE of 14.37%  $FF$  of 76.93%,  $J_{SC}$  of 17.98 mA cm<sup>-2</sup> and  $V_{OC}$  of 1.04 V. The RTP-treated samples achieved similar PCE,  $FF$ ,  $J_{SC}$ , and  $V_{OC}$  at two specific conditions: 110 °C for 30 s and 140 °C for 20 s. It is worth noting that these temperatures of RTP are set point temperatures, the actual temperature might not be the same, especially the perovskite films. The entire annealing process happens within tens of seconds, it is impossible to measure the actual temperature of the perovskite films in the current experimental set-up (more details in the Experimental Section).

**Table 10.** Optimization process of RTP versus hot-plate annealing. Active area = 0.105 cm<sup>2</sup>.

Temp (°C) \ Time (s)	120	60	30	20	10	5
110	11.74%, 70.42% 1.02 V 16.40 mA/cm <sup>2</sup>	14.00%, 73.41% 1.03 V 18.51 mA/cm <sup>2</sup>	15.14%, 76.75% 1.05 V 18.74 mA/cm <sup>2</sup>	12.11%, 68.94% 1.03 V 17.01 mA/cm <sup>2</sup>	9.21%, 67.97% 0.84 V 16.11 mA/cm <sup>2</sup>	6.33%, 59.79% 0.77 V 13.84 mA/cm <sup>2</sup>
140	11.03%, 70.04% 1.01 V 15.67 mA/cm <sup>2</sup>	13.95%, 73.18% 1.02 V 18.79 mA/cm <sup>2</sup>	14.59%, 74.98% 1.03 V 18.83 mA/cm <sup>2</sup>	14.93%, 76.45% 1.05 V 18.67 mA/cm <sup>2</sup>	13.57%, 72.34% 1.02 V 18.39 mA/cm <sup>2</sup>	8.07%, 66.83% 0.81 V 14.85 mA/cm <sup>2</sup>
170						
200						
220						
250						
Hot-plate 140	14.37%, 76.93% 1.04 V 17.98 mA/cm <sup>2</sup>					N/A

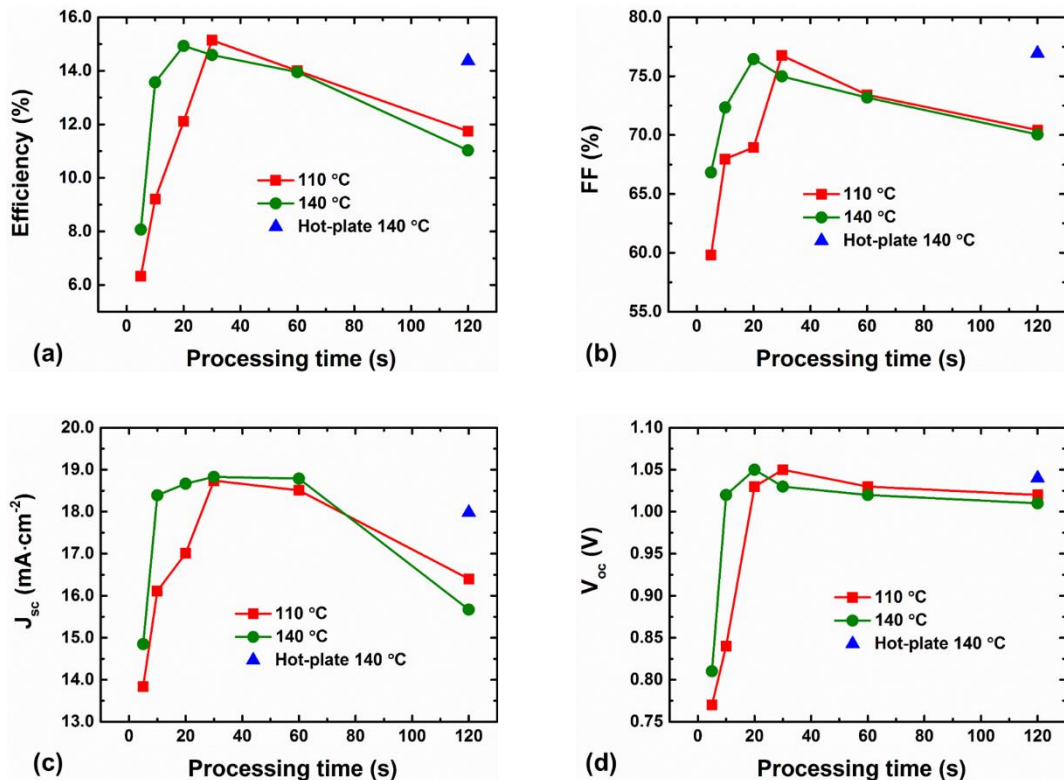


**Figure 31.** Trends of a) efficiency, b) FF, c) J<sub>sc</sub> and d) V<sub>oc</sub> at different RTP temperatures for different time. Active area = 0.105 cm<sup>2</sup>.

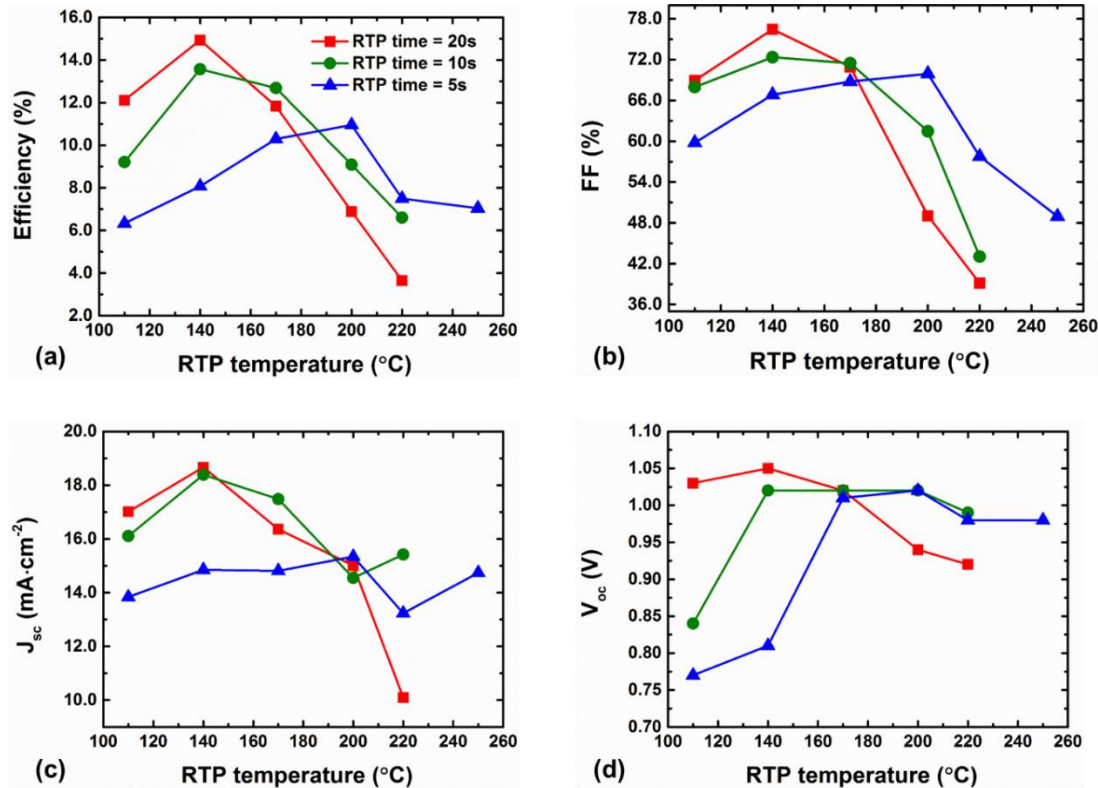


**Figure 32.** Trends of a) efficiency, b) FF, c)  $J_{sc}$  and d)  $V_{oc}$  at different RTP temperatures for 5, 10 and 20 seconds. Active area =  $0.105 \text{ cm}^2$ .

**Figure 33** shows XRD spectra and UV-Vis absorbance of samples from selected annealing conditions. XRD and UV-Vis results are very close for three conditions: RTP at 110 °C for 30 s, RTP at 140 °C for 20 s and hot-plate annealing at 140 °C for 2 minutes. This is in good agreement with the similar photovoltaic performance shared by these three annealing conditions. Sample annealed by RTP at 110 °C for 5s has sharp but weakest peak intensity. It means that the  $\text{MAPbI}_3$  has formed but not reached a good quality yet, supported by its much weaker UV-Vis absorbance than those from other annealing conditions. **Figure 34** compares SEM top-view morphologies of  $\text{MAPbI}_3$  films from selected annealing conditions. Similar densely-packed films with defined grains have been observed for the

same three conditions: RTP at 110 °C for 30 s, RTP at 140 °C for 20 s and hot-plate annealing at 140 °C for 2 minutes. The SEM image of a disordered morphology verifies that RTP at 110 °C for 5 s provides insufficient energy for annealing the perovskite film. In contrast, RTP at 250 °C for 5 s supplies an overdose of energy to the perovskite film, leading to larger grain sizes, which might explain the higher UV-Vis absorbance and XRD peak intensity, but also damaging the film and creating cracks and other defects in it.

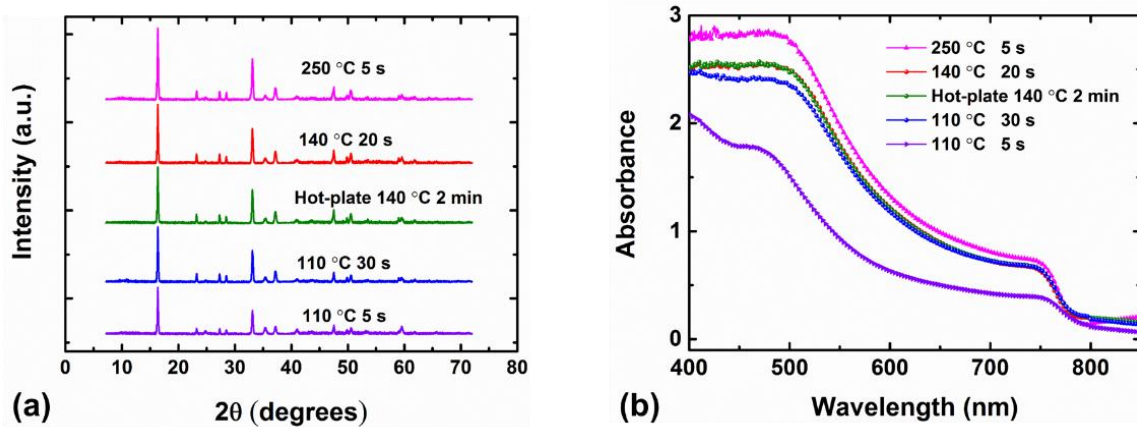


**Figure 33.** a) XRD and b) UV-Vis results of selected annealing conditions.

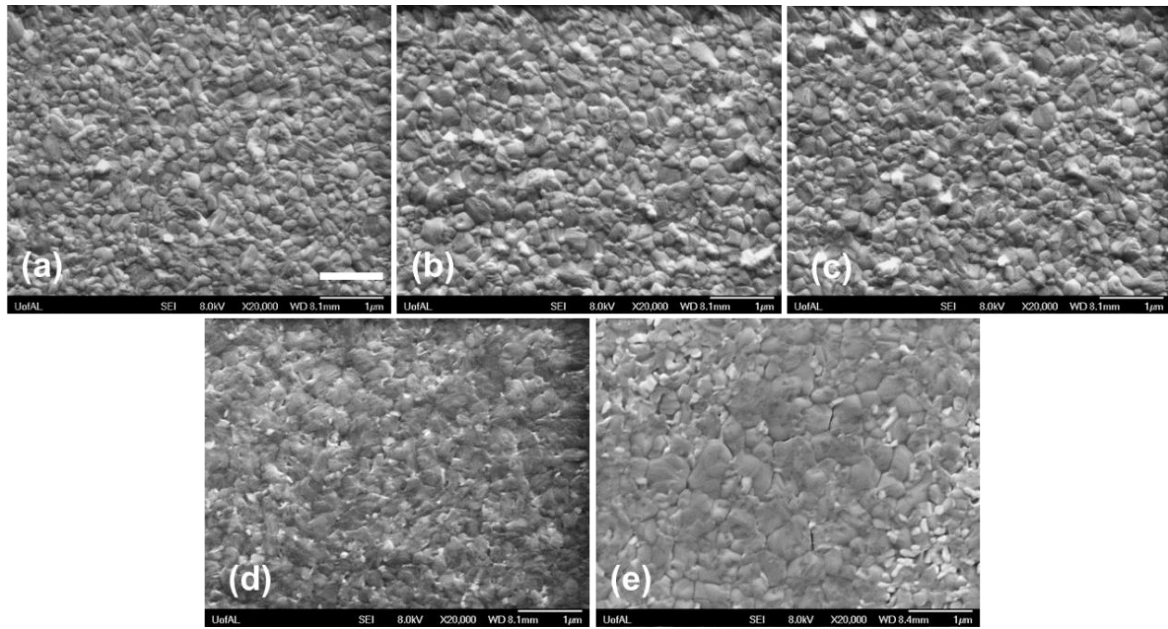


**Figure 34.** Top-view SEM images of RTP films at a) 110 °C for 30 s, b) 140 °C for 20 s, c) hot-plate annealed at 140 °C for 2 minutes, d) 110 °C 5 s, and e) 250 °C 5 s. The scale bar is 1  $\mu\text{m}$ .

More devices have been made on the best RTP conditions as well as the hot-plate control condition. **Figure 35a** shows comparison between the best hot-plate reference device and top RTP devices. The device from hot-plate annealing demonstrates PCEs of 17.34% and 18.71% from forward and reverse scans, respectively. PVSCs with RTP at 140 °C for 20 s yield a slightly overall better photovoltaic performance, with PCEs of 18.33% and 18.60% from forward and reverse scans, respectively. In contrast, RTP at 110 °C for 30 s leads to PCEs slightly less than 17.5%. **Figure 35b** exhibits the external quantum efficiency (EQE) and the corresponding integrated  $J_{\text{SC}}$  of the devices with the same annealing conditions as shown in **Figure 35a**. RTP at 140 °C for 20 s and hot-plate annealing at 140 °C for 2 minutes have almost identical EQE curve, marginally better than that of RTP at 110 °C for 30 s. In spite of annealing methods, the integrated  $J_{\text{SCs}}$  calculated from the EQEs are very close to the

values acquired from J-V measurements (**Figure 35a**). The good match between J-V and EQE measurements confirms the validity of obtained photovoltaic parameters. The similarities of photovoltaic performance from RTP at 140 °C for 20 s and hot-plate annealing at 140 °C for 2 minutes also agree with the findings from XRD, UV-Vis and SEM results. Nevertheless, the demonstrated RTP devices showed comparable photovoltaic performance to their hot-plate-annealed counterparts, underlining the success of such a radiative treatment for building high-performance PVSCs. More importantly, the annealing time of RTP is significantly shorter than that of the traditional thermal annealing (20 s versus 2 minutes). As a result, RTP has much better compatibility with large-scale manufacturing methods such as the R2R processing. Assuming a R2R printing speed of 10 cm per second,<sup>[141]</sup> the RTP equipment will only need 2 m length (10 cm/s times 20 s) as compared to a 12 m long (10 cm/s times 2 min) oven if the traditional thermal annealing is used.

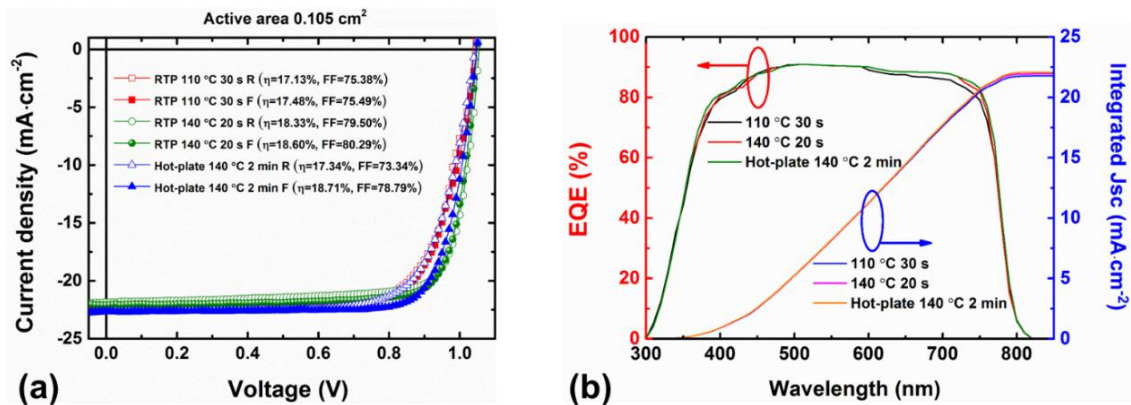


**Figure 35.** a) J-V curves of RTP devices at 110 °C for 30 s & 140 °C for 20 s, and hot-plate annealed at 140 °C for 2 minutes. b) EQEs of the corresponding devices.

### 5.2.2 Upscaling of PVSCs

Mini-modules of PVSCs have been made adopting the optimal RTP condition i.e. 140 °C for 20 s and the hot-plate condition 140 °C for 2 minutes. The detailed structure of mini-modules can be found in the reference.<sup>[142]</sup> Each mini-module comprises three sub-cells monolithically interconnected in series. The designated area of a mini-module is 3 cm<sup>2</sup> (including dead area from interconnections) with a geometric fill factor of 0.9, giving an active device area of 2.7 cm<sup>2</sup>. **Figure 36** shows comparison between the champion RTP mini-module and the best hot-plate-annealed mini-module. In **Figure 36a**, J-V curves of RTP mini-module exhibit active-area PCE over 17.73%, which is comparable to the active-area PCE over 16.65% from the hot-plate-annealed mini-module. The difference on PCEs is mainly from different  $J_{SC}$  and  $FF$ . The RTP and hot-plate mini-modules have an almost identical  $V_{OC}$  = 3.12 V, which is equivalent to an average of 1.04 V for each individual sub-cell for these three-cell mini-modules. The photovoltaic performance of the RTP mini-module is very similar to that of the small-area device as shown in **Figure 35a**. This not only confirms that the RTP/blade-coated perovskite film has high quality over the large area, but also proves that the combination of RTP & blade-coating is suitable for upscaling the manufacture of PVSCs.

**Figure 36b** provides quasi-SPO (stabilized power output) of the RTP and hot-plate mini-modules. The quasi-SPO has been measured with an approximating method by sweeping voltage in a very small range near the maximal power point (MPP) for some time. The left inset of **Figure 36b** marks the respective MPPs (point A and B) for the RTP and hot-plate mini-modules in their power-voltage (P-V) curves. The right inset of **Figure 36b** is a photo of the mini-module. The statistics of the J-V measurements are displayed in **Figure 37**. The data

for the box charts were extracted from over 30 J-V measurements for RTP and hot-plate mini-modules each. It is worth noting that all the measurements, J-V and quasi-SPO, were carried out in ambient environment without any thermal or humidity control. In addition, the quasi-SPOs were measured after all the J-V data had been collected, meaning that the mini-modules had already been exposed to air and experienced thermal stress for quite some time before SPO measurements. This explains why the efficiencies extracted from quasi-SPOs are not as high as those from the J-V measurements.

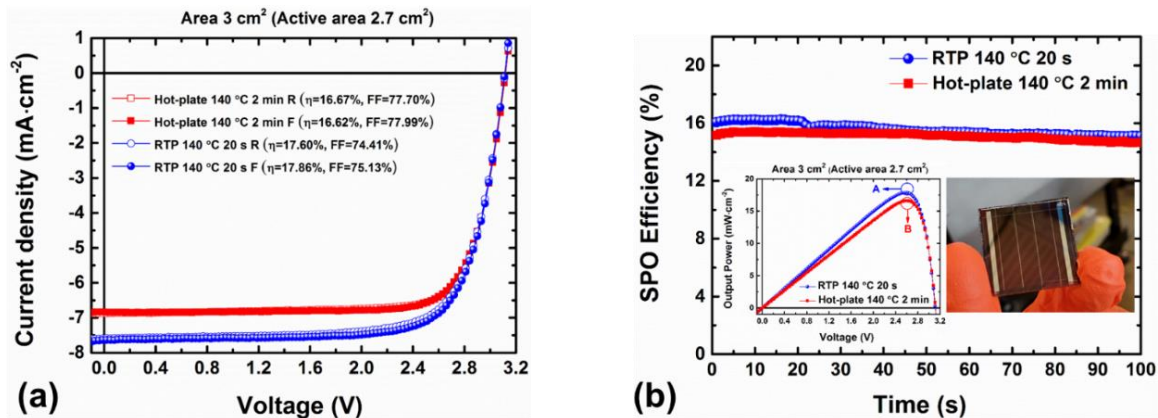


**Figure 36.** a) J-V curves of mini-modules made from RTP at 140 °C for 20 s and hot-plate annealed at 140 °C for 2 minutes. b) quasi-SPOs of the corresponding mini-modules. Active area = 2.7 cm<sup>2</sup>. Inset left: P-V curves of mini-modules; Inset right: photo of a mini-module.

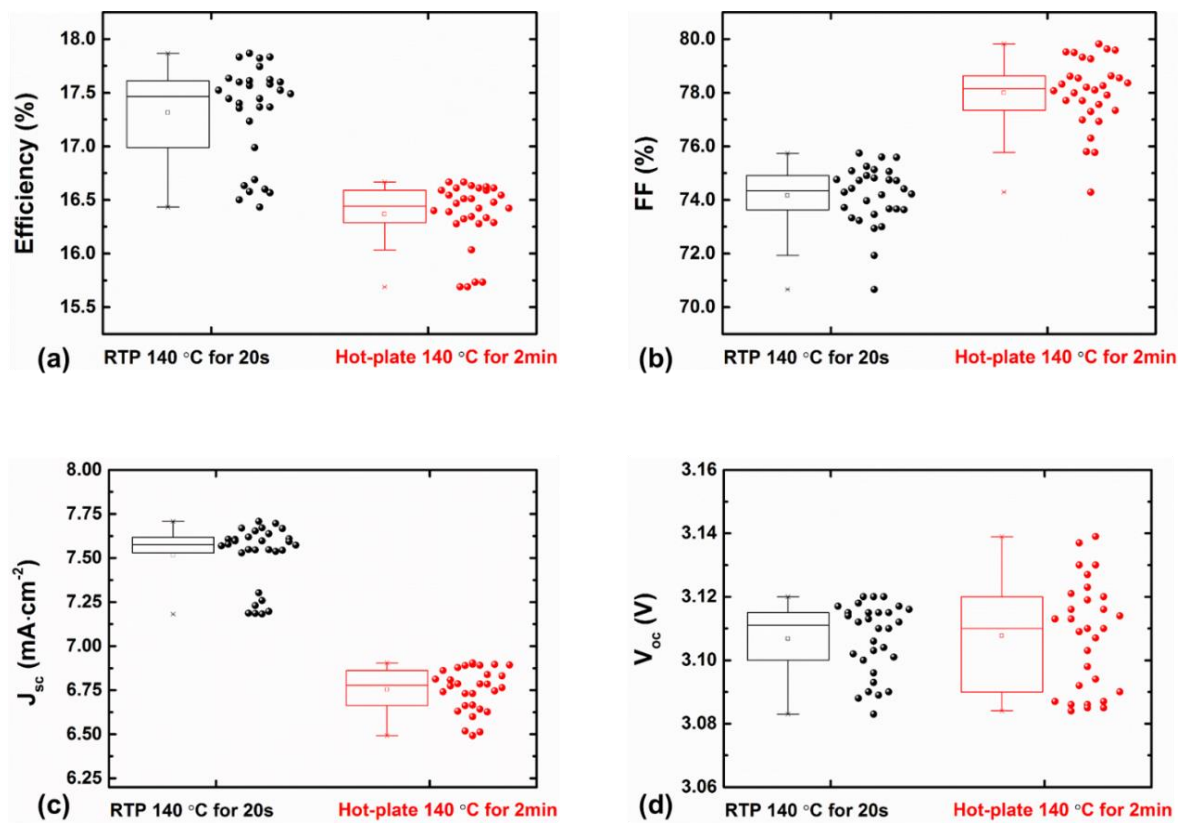


**Figure 37.** Box charts of a) efficiency, b)  $FF$ , c)  $J_{sc}$  and d)  $V_{oc}$  for mini-modules annealed by RTP and hot plate. Active area =  $2.7 \text{ cm}^2$ .

## CHAPTER 6. CONCLUSIONS AND FUTURE WORK

### 6.1 Conclusions

This dissertation demonstrates simulation study of thermoelectric generators (TEGs) and experimental study of perovskite solar cells (PVSCs).

In Chapter 2, a series of 3D TEG modules, including symmetrical and non-symmetrical models with diversified geometries and up to 128 unicouples, have been established in ANSYS environment. Manifold TE materials, whose signature properties, such as the Seebeck coefficients, electrical resistivities and thermal conductivities are all temperature dependent and extracted directly from recent publications. It is found that the TEG modules with the current best p-type TE materials teamed up with the strongest n-type TE materials could yield efficiencies of up to 17.0% and 20.9% at  $\Delta T = 500$  K and  $\Delta T = 700$  K, respectively. The achieved high efficiencies approximate the theoretical efficiency upper limits, validating that the best p-type SnSe and the strongest n-type SiGe in the high temperature realm, hold the potential to combine with the traditional high-ZT low-temperature materials, such as p-type BiSbTe and n-type CuBiTeSe. Bridged by the intermediate segments for the sake of the compatibility, such combination is able to create high-performance TEG devices without adversely affecting each other between components. In addition, the output power densities over 2.1 Watt cm<sup>-2</sup> are feasible at optimal geometrical ratio with a temperature difference of 700 K, even with  $\Delta T = 500$  K, the output power densities can reach and exceed 1.0 Watt cm<sup>-2</sup>. Due to the fact that the n-type TE materials are

universally weaker than their p-type counterparts, unsymmetrical geometry of  $A_n < A_p$  is necessary in obtaining the optimized TEG performance. Results also show that the proposed relationship  $\frac{A_n}{A_p} = \sqrt{\frac{\rho_n(T) \cdot \kappa_p(T)}{\rho_p(T) \cdot \kappa_n(T)}} = \left( \sum_{T_c}^{T_h} \sqrt{\frac{\rho_n(T) \cdot \kappa_p(T)}{\rho_p(T) \cdot \kappa_n(T)}} \Delta T \right) / (T_h - T_c)$  can be used to accurately speculate the optimal geometrical ratio for the maximum efficiency of TEG modules. From the perspective of the compatibility factor, a successful segmentation of different TE materials can be achieved by a gradual change of  $s$  value from one end of the TEG leg to the other, even if  $s$  of the cold side and the hot side differ by more than a factor of 2. Furthermore, the influence of thermal radiation and contact resistances has also been investigated. The results show that thermal radiation has limited effect on the TEG performance while contact resistances, particularly the electrical one, could have destructive impact on the TEG efficiency and output power. Nevertheless, the plateaus showing at lower contact resistances provide tolerance space for interface quality in building high performance segmented TEGs from the current best TE materials.

In Chapter 3, segmented TEG modules are constructed by currently high-performance TE materials, including various Chalcogenides, SiGe alloy, Skutterudites and Half-Heuslers. These TE materials are prudently chosen based on an overall consideration of the TE figure of merit ( $ZT$ ), compatibility factors and power factors. Four different segmented TEG modules are built up by assembling two groups of p-type TE materials and two groups of n-type TE materials. 3D finite-element analysis with ANSYS was conducted for systematical modelling of these segmented TEG modules. All the temperature-dependent TE properties were extracted directly from the published experimental data, covering a temperature range from 300 K to 1000 K. Contact effects including the electrical and thermal contact resistances

are also considered, at both the TE-TE and TE-electrode interfaces. Two kinds of boundary conditions (BCs) are imposed, with type I representing the temperature of 1000 K at hot side versus 300 K (323K, 348K, 373K) at cold end of TEG modules and type II having 1000 K held at hot sides while varying the heat transfer coefficients of cold sides. These two classes of BCs are adopted to discover the optimal TEG leg cross-sectional area ratios ( $A_n/A_p$ ) and optimum leg lengths of TEG modules, respectively. The results show that the TE materials with high power factors, such as Yb-filled SKD and HHs, are preferred only for the applications in which cost is not a major concern. When expenses are taken into account, successful segmentation of high-ZT TE materials exhibit remarkable advantages: a cost-performance ratio of  $\sim 0.86 \text{ \$ W}^{-1}$  with an efficiency of 17.8% and a power density of 3.0 Watt cm $^{-2}$  have been demonstrated. On the other hand, their rivals with larger power factors can only make segmented TEG modules capable of offering a cost-performance ratio of  $\sim 1.11 \text{ \$ W}^{-1}$ , efficiency of 16.2% and output power density of 2.4 Watt cm $^{-2}$ . The demonstrated low cost-effectiveness, high efficiency and large output power density are a perfect match for high temperature applications such as automobiles, aircrafts and industrial furnaces. The design method and procedure shown in this study can serve as a guidance to the planning and implementation of cost-effective TEG systems. More importantly, these results not only confirm ZT as the number one criterion for selecting TE materials, but also forecast the commercial viability and competitiveness of segmented TEGs in the same metrics as other renewable energy sources.

In Chapter 4, I demonstrated rapid LED UV light annealing on PVSK active layer and achieved efficiency over 18% in a simple planar inverted structure ITO/PEDOT:PSS/

MAPbI<sub>3</sub>/PC<sub>71</sub>BM/Al without any further device engineering. With subsequent UV annealing of the PC<sub>71</sub>BM ETL layer, PCE close to 19% from the best cell has been attained without any hysteresis. To my best knowledge, this PCE above 18% is the highest efficiency accomplished from photonic treatments. Different in principle from other photonic treatment techniques, this LED UV annealing method is based on complete light absorption, rather than inefficient photonic-to-thermal annealing that could heat up and damage flexible substrates. The LED light source is able to provide a specific UV wavelength for maximum light absorption and is very efficient in energy conversion from electricity to photonic radiation. Furthermore, the complete UV light absorption and negligible reflection and heat transfer to surrounding materials allow me to accurately estimate the deposition energy required to form PVSK film at the device quality level. With the feature of rapid and layer-specific annealing, this fast LED UV annealing technology paves the way for high-speed printing of high-performance PVSCs on flexible substrate for mass production. In addition to the traditional MAPbI<sub>3</sub> material, this novel photonic treatment could also be applied to other emerging PVSK material systems in photovoltaic applications and could be extended to all other PVSK thin-film based semiconductor devices, such as PVSK LEDs and photodetectors.

In Chapter 5, I demonstrate successful blade-coating and rapid thermal processing (RTP) for fabrication of planar p-i-n PVSCs in ambient environment. Both small devices and mini-modules have been made, with active areas of 0.105 cm<sup>2</sup> and 2.7 cm<sup>2</sup>, respectively. The best small device shows an average PCE over 18.47% from forward and reverse scans, while the champion mini-module exhibits an average PCE over 17.73% from scans of different directions. In addition, these efficiencies are accompanied by high fill factors, with average

values of 79.90% and 74.77% for the best small device and mini-module, respectively. The efficiency of the top mini-module is the highest so far for cm<sup>2</sup>-scale PVSCs annealed by RTP. Furthermore, RTP method reduces the annealing time of blade-coated MAPbI<sub>3</sub> films from 2 minutes for hot plate to less than 30 seconds. This four-fold decrease of annealing time will facilitate the road towards high-speed coating of perovskite layers. These results validate the practicability of using RTP method for upscaling the manufacturing of PVSCs. Likely the blade-coating will be replaced by slot-die coating and RTP will be substituted by LED arrays to realize R2R printing and large-scale manufacturing of PVSCs.

## 6.2. Future Work

This dissertation has already proved the concept of photonic annealing with UV LED. However, the configuration of ITO/PEDOT:PSS/ MAPbI<sub>3</sub>/PC<sub>71</sub>BM/Al was used without any device engineering. These choices of materials are good for proof-of-concept but limit the device efficiency and stability of PVSCs. Efficiency of 19% is decent but still far away from the theoretical upper limit. According to Shockley-Queisser theory<sup>[143]</sup>, the lead-containing PVSCs have a theoretical maximal PCE over 31%, which corresponds to  $J_{SC} = 27.26$  mA/cm<sup>2</sup>,  $V_{OC} = 1.26$  V and  $FF = 90.2\%$ . Currently even the state-of-the-art PVSCs have all of these parameters far below the theoretical maxima<sup>[46]</sup>, indicating a large room for improvement.

The future work will target at PCE of > 25%, which can be broken down into  $J_{SC} > 25.0$  mA/cm<sup>2</sup>,  $V_{OC} > 1.18$  V,  $FF > 85\%$ . ITO/NiO<sub>x</sub>/triple-cation-mixed-halide-PVSK/SnO<sub>2</sub>/Al is the most promising PVSC architecture to attain these parameters while maintaining the

promise of high-stability and low-cost solution processing. Employing metal oxides rather than organic materials (PEDOT:PSS or PC<sub>71</sub>BM) as charge transporting layers (CTLs) has been demonstrated to significantly enhance device stability.<sup>[60]</sup> Inorganic nickel oxide (NiO<sub>x</sub>) for hole transport layer (HTL) and tin oxide (SnO<sub>2</sub>) for electron transport layer (ETL) are the most promising CTLs on the route towards highly-stable, high-efficiency and cost-efficient PVSCs. As being metal oxides, they promise exceptional charge transport capability, noble intrinsic chemical stability, easy solution processing and low material costs.<sup>[144-146]</sup> However, with commonly used hot-plate annealing, metal-oxides require high temperatures and long duration to form the desired crystallinity.<sup>[144]</sup> Since a hot plate (or any other thermal annealing) heats all the stacking layers simultaneously, the flexible substrates and PVS<sub>K</sub> absorber layer could be damaged because of their limited temperature tolerance up to 150 °C for a short period.<sup>[147]</sup> Also, lengthy annealing with a hot plate is not compatible with high-speed printing. In the future work, photonic irradiation from UV LEDs will be utilized to achieve rapid and layer-specific annealing for the NiO<sub>x</sub> HTL and SnO<sub>2</sub> ETL without damaging the underlying flexible substrate and PVS<sub>K</sub> absorber layer, respectively. Unlike hot plate heating in which each layer shares the same temperature via thermal conduction, LED photonic treatment is able to selectively supply energy to a specific layer through photon absorption. First, the wavelength of LED irradiation can be specifically chosen to reach a peak absorption in the target layer. Second, strong photon absorption and exponential decay of light intensity in the aiming layer could have energy supply concentrated on a single layer, leading to a highly-selective photonic treatment. Along with a well-controlled LED irradiation time that limits heat transfer through thermal conduction, layer-specific annealing

can be achieved without detrimentally affecting underlying films. With this highly-selective annealing technology through UV LEDs, both high-quality  $\text{NiO}_x$  and  $\text{SnO}_2$  CTLs can be stacked in the same solar cell device, which will not only improve PVSC stability by providing effective physical protection to PVK absorber layer, but also promote the charge transport and efficiency, achieving the best of both worlds. In addition, perovskite systems with mixed-cations and mixed-anions will be engineered for thermal stability and further improvement in efficiency. The compositional engineering based on triple-cation mixed-halide perovskites will significantly improve the intrinsic thermal stability of the PVK materials while high-quality metal oxides will enhance the environmental stability, effectively preventing infiltration of moisture & oxygen and contact metal diffusion into PVK absorber layer as well.<sup>[45, 144-146, 148-149]</sup>

## REFERENCES

- [1] H. J. Goldsmid, *Introduction to thermoelectricity*, Springer Science & Business Media, **2009**.
- [2] L. A. Fisk, *Science* **2005**, 309, 2016.
- [3] G. J. Snyder, *Electrochem. Soc. Interface* **2008**, 17, 54.
- [4] C. J. W. Smith, J. S. Cahill, A. Nuhoglu, *PAM Review: Energy Science & Technology* **2016**, 3, 86.
- [5] C. Gayner, K. K. Kar, *Progress in Materials Science* **2016**, 83, 330.
- [6] S. Twaha, J. Zhu, Y. Yan, B. Li, *Renew. Sustain. Energy Rev.* **2016**, 65, 698.
- [7] H. Alam, S. Ramakrishna, *Nano Energ.* **2013**, 2, 190.
- [8] M. H. Elsheikh, D. A. Shnawah, M. F. M. Sabri, S. B. M. Said, M. H. Hassan, M. B. A. Bashir, M. Mohamad, *Renew. Sustain. Energy Rev.* **2014**, 30, 337.
- [9] P. Sundarraj, D. Maity, S. S. Roy, R. A. Taylor, *RSC Adv.* **2014**, 4, 46860.
- [10] X. Zheng, C. Liu, Y. Yan, Q. Wang, *Renew. Sustain. Energy Rev.* **2014**, 32, 486.
- [11] T. M. Tritt, M. Subramanian, *MRS BULL.* **2006**, 31, 188.
- [12] L. E. Bell, *Science* **2008**, 321, 1457.
- [13] W. Xie, J. He, H. J. Kang, X. Tang, S. Zhu, M. Laver, S. Wang, J. R. Copley, C. M. Brown, Q. Zhang, *Nano Lett.* **2010**, 10, 3283.
- [14] H. Zhao, J. Sui, Z. Tang, Y. Lan, Q. Jie, D. Kraemer, K. McEnaney, A. Guloy, G. Chen, Z. Ren, *Nano Energ.* **2014**, 7, 97.
- [15] H. Wu, L.-D. Zhao, F. Zheng, D. Wu, Y. Pei, X. Tong, M. Kanatzidis, J. He, *Nat. Commun.* **2014**, 5, 4515.

- [16] L.-D. Zhao, S.-H. Lo, Y. Zhang, H. Sun, G. Tan, C. Uher, C. Wolverton, V. P. Dravid, M. G. Kanatzidis, *Nature* **2014**, 508, 373.
- [17] S. Wang, W. Xie, H. Li, X. Tang, *Intermetallics* **2011**, 19, 1024.
- [18] L. Pan, D. Bérardan, N. Dragoe, *J. Am. Chem. Soc.* **2013**, 135, 4914.
- [19] G. Joshi, T. Dahal, S. Chen, H. Wang, J. Shiomi, G. Chen, Z. Ren, *Nano Energ.* **2013**, 2, 82.
- [20] W. Liu, X. Tang, H. Li, K. Yin, J. Sharp, X. Zhou, C. Uher, *J. Mater. Chem.* **2012**, 22, 13653.
- [21] D. Mei, Y. Li, Z. Yao, H. Wang, T. Zhu, S. Chen, *J. Alloys Compd.* **2014**, 609, 201.
- [22] S. Bathula, M. Jayasimhadri, N. Singh, A. Srivastava, J. Pulikkotil, A. Dhar, R. Budhani, *Appl. Phys. Lett.* **2012**, 101, 213902.
- [23] W. Liu, H. S. Kim, S. Chen, Q. Jie, B. Lv, M. Yao, Z. Ren, C. P. Opeil, S. Wilson, C.-W. Chu, *Proc. Natl. Acad. Sci.* **2015**, 112, 3269.
- [24] A. D. LaLonde, Y. Pei, G. J. Snyder, *Energy Environ. Sci.* **2011**, 4, 2090.
- [25] S. N. Guin, V. Srihari, K. Biswas, *J. Mater. Chem. A* **2015**, 3, 648.
- [26] D. Wu, Y. Pei, Z. Wang, H. Wu, L. Huang, L. D. Zhao, J. He, *Adv. Func. Mater.* **2014**, 24, 7763.
- [27] P. Puneet, R. Podila, M. Karakaya, S. Zhu, J. He, T. M. Tritt, M. S. Dresselhaus, A. M. Rao, *Sci. Rep.* **2013**, 3.
- [28] W. S. Liu, Q. Zhang, Y. Lan, S. Chen, X. Yan, Q. Zhang, H. Wang, D. Wang, G. Chen, Z. Ren, *Adv. Energy Mater.* **2011**, 1, 577.
- [29] K. F. Hsu, S. Loo, F. Guo, W. Chen, J. S. Dyck, C. Uher, T. Hogan, E. Polychroniadis, M. G. Kanatzidis, *Science* **2004**, 303, 818.
- [30] X. Shi, J. Yang, J. R. Salvador, M. Chi, J. Y. Cho, H. Wang, S. Bai, J. Yang, W. Zhang, L. Chen, *J. Am. Chem. Soc.* **2011**, 133, 7837.
- [31] R. Basu, S. Bhattacharya, R. Bhatt, M. Roy, S. Ahmad, A. Singh, M. Navaneethan, Y. Hayakawa, D. Aswal, S. Gupta, *J. Mater. Chem. A* **2014**, 2, 6922.

- [32] D. M. Rowe, *Thermoelectrics handbook: macro to nano*, CRC press, **2005**.
- [33] J. Xiao, T. Yang, P. Li, P. Zhai, Q. Zhang, *Appl. Energy* **2012**, 93, 33.
- [34] X. Liang, X. Sun, H. Tian, G. Shu, Y. Wang, X. Wang, *Appl. Energy* **2014**, 130, 190.
- [35] Z. Liu, S. Zhu, Y. Ge, F. Shan, L. Zeng, W. Liu, *Appl. Energy* **2017**, 190, 540.
- [36] G. J. Snyder, *Appl. Phys. Lett.* **2004**, 84, 2436.
- [37] H. Ali, B. S. Yilbas, A. Al-Sharafi, *Appl. Energy* **2017**, 187, 367.
- [38] G. J. Snyder, T. S. Ursell, *Phys. Rev. Lett.* **2003**, 91, 148301.
- [39] K. McEnaney, D. Kraemer, Z. Ren, G. Chen, *J. Appl. Phys.* **2011**, 110, 074502.
- [40] C. Hadjistassou, E. Kyriakides, J. Georgiou, *Energy Convers. Manag.* **2013**, 66, 165.
- [41] P. H. Ngan, D. V. Christensen, G. J. Snyder, L. T. Hung, S. Linderoth, N. V. Nong, N. Pryds, *Phys. Status Solidi A* **2014**, 211, 9.
- [42] U. Erturun, K. Erermis, K. Mossi, *Appl. Therm. Eng.* **2014**, 73, 126.
- [43] A. Rezania, L. Rosendahl, H. Yin, *J. of Power Sources* **2014**, 255, 151.
- [44] A. Kojima, K. Teshima, Y. Shirai, T. Miyasaka, *J. Am. Chem. Soc.* **2009**, 131, 6050.
- [45] Y. Yang, J. You, *Nature* **2017**, 544, 155.
- [46] Y. Rong, Y. Hu, A. Mei, H. Tan, M. I. Saidaminov, S. I. Seok, M. D. McGehee, E. H. Sargent, H. Han, *Science* **2018**, 361, eaat8235.
- [47] J. Burschka, N. Pellet, S.-J. Moon, R. Humphry-Baker, P. Gao, M. K. Nazeeruddin, M. Graetzel, *Nature* **2013**, 499, 316.
- [48] D. Liu, T. L. Kelly, *Nat. Photon.* **2014**, 8, 133.
- [49] N. J. Jeon, J. H. Noh, Y. C. Kim, W. S. Yang, S. Ryu, S. Il Seol, *Nat. Mater.* **2014**, 13, 897.
- [50] W. Nie, H. Tsai, R. Asadpour, J.-C. Blancon, A. J. Neukirch, G. Gupta, J. J. Crochet, M. Chhowalla, S. Tretiak, M. A. Alam, H.-L. Wang, A. D. Mohite, *Science* **2015**, 347, 522.

- [51] W. Zhang, M. Saliba, D. T. Moore, S. K. Pathak, M. T. Hörantner, T. Stergiopoulos, S. D. Stranks, G. E. Eperon, J. A. Alexander-Webber, A. Abate, *Nat. Commun.* **2015**, 6, 6142.
- [52] Q. Tai, P. You, H. Sang, Z. Liu, C. Hu, H. L. Chan, F. Yan, *Nat. Commun.* **2016**, 7, 11105.
- [53] D. Bi, C. Yi, J. Luo, J.-D. Décoppet, F. Zhang, S. M. Zakeeruddin, X. Li, A. Hagfeldt, M. Grätzel, *Nat. Energy* **2016**, 1, 16142.
- [54] Y. Wu, X. Yang, W. Chen, Y. Yue, M. Cai, F. Xie, E. Bi, A. Islam, L. Han, *Nat. Energy* **2016**, 1, 16148.
- [55] M. Yang, Z. Li, M. O. Reese, O. G. Reid, D. H. Kim, S. Siol, T. R. Klein, Y. Yan, J. J. Berry, M. F. van Hest, *Nat. Energy* **2017**, 2, 17038.
- [56] H. Chen, F. Ye, W. Tang, J. He, M. Yin, Y. Wang, F. Xie, E. Bi, X. Yang, M. Grätzel, *Nature* **2017**, 550, 92.
- [57] J.-H. Im, I.-H. Jang, N. Pellet, M. Graetzel, N.-G. Park, *Nat. Nanotechnol.* **2014**, 9, 927.
- [58] N. Ahn, D.-Y. Son, I.-H. Jang, S. M. Kang, M. Choi, N.-G. Park, *J. Am. Chem. Soc.* **2015**, 137, 8696.
- [59] C. Bi, Q. Wang, Y. Shao, Y. Yuan, Z. Xiao, J. Huang, *Nat. Commun.* **2015**, 6, 7747.
- [60] J. You, L. Meng, T.-B. Song, T.-F. Guo, Y. M. Yang, W.-H. Chang, Z. Hong, H. Chen, H. Zhou, Q. Chen, Y. Liu, N. De Marco, Y. Yang, *Nat. Nanotechnol.* **2016**, 11, 75.
- [61] C.-H. Chiang, C.-G. Wu, *Nat. Photon.* **2016**, 10, 196.
- [62] D. Koushik, W. J. Verhees, Y. Kuang, S. Veenstra, D. Zhang, M. A. Verheijen, M. Creatore, R. E. Schropp, *Energy Environ. Sci.* **2017**, 10, 91.
- [63] H. Tan, A. Jain, O. Voznyy, X. Lan, F. P. G. de Arquer, J. Z. Fan, R. Quintero-Bermudez, M. Yuan, B. Zhang, Y. Zhao, *Science* **2017**, 355, 722.
- [64] W. S. Yang, B.-W. Park, E. H. Jung, N. J. Jeon, Y. C. Kim, D. U. Lee, S. S. Shin, J. Seo, E. K. Kim, J. H. Noh, *Science* **2017**, 356, 1376.
- [65] N. Arora, M. I. Dar, A. Hinderhofer, N. Pellet, F. Schreiber, S. M. Zakeeruddin, M. Grätzel, *Science* **2017**, 358, 768.
- [66] S.-H. Turren-Cruz, M. Saliba, M. T. Mayer, H. Juárez-Santiesteban, X. Mathew, L.

Nienhaus, W. Tress, M. P. Erodici, M.-J. Sher, M. G. Bawendi, *Energy Environ. Sci.* **2018**, 11, 78.

- [67] D. Luo, W. Yang, Z. Wang, A. Sadhanala, Q. Hu, R. Su, R. Shivanna, G. F. Trindade, J. F. Watts, Z. Xu, *Science* **2018**, 360, 1442.
- [68] W. Nie, J.-C. Blancon, A. J. Neukirch, K. Appavoo, H. Tsai, M. Chhowalla, M. A. Alam, M. Y. Sfeir, C. Katan, J. Even, *Nat. Commun.* **2016**, 7, 11574.
- [69] D. W. DeQuilettes, W. Zhang, V. M. Burlakov, D. J. Graham, T. Leijtens, A. Osherov, V. Bulović, H. J. Snaith, D. S. Ginger, S. D. Stranks, *Nat. Commun.* **2016**, 7, 11683.
- [70] H. Tsai, R. Asadpour, J.-C. Blancon, C. C. Stoumpos, O. Durand, J. W. Strzalka, B. Chen, R. Verduzco, P. M. Ajayan, S. Tretiak, *Science* **2018**, 360, 67.
- [71] J. Troughton, C. Charbonneau, M. J. Carnie, M. L. Davies, D. A. Worsley, T. M. Watson, *J. Mater. Chem. A* **2015**, 3, 9123.
- [72] J. Troughton, M. J. Carnie, M. L. Davies, C. Charbonneau, E. H. Jewell, D. A. Worsley, T. M. Watson, *J. Mater. Chem. A* **2016**, 4, 3471.
- [73] B. W. Lavery, S. Kumari, H. Konermann, G. L. Draper, J. Spurgeon, T. Druffel, *ACS Appl. Mater. Interfaces* **2016**, 8, 8419.
- [74] V. L. Pool, B. Dou, D. G. Van Campen, T. R. Klein-Stockert, F. S. Barnes, S. E. Shaheen, M. I. Ahmad, M. F. Van Hest, M. F. Toney, *Nat. Commun.* **2017**, 8, 14075.
- [75] A. I. M. Leguy, Y. Hu, M. Campoy-Quiles, M. I. Alonso, O. J. Weber, P. Azarhoosh, M. Van Schilfgaarde, M. T. Weller, T. Bein, J. Nelson, *Chem. Mater.* **2015**, 27, 3397.
- [76] Z. Ouyang, H. Abrams, R. Bergstone, Q. Li, F. Zhu, D. Li, *Adv. Energy Mater.* **2019**, 1902898.
- [77] D. Kraemer, B. Poudel, H.-P. Feng, J. C. Caylor, B. Yu, X. Yan, Y. Ma, X. Wang, D. Wang, A. Muto, *Nat. Mater.* **2011**, 10, 532.
- [78] J. J. D'Angelo, E. J. Timm, F. Ren, B. D. Hall, E. Case, H. Schock, M. Kanatzidis, D. Y. Chung, T. P. Hogan, presented at MRS Proceedings **2007**.
- [79] Y. X. Gan, F. W. Dynys, *Mater. Chem. Phys.* **2013**, 138, 342.
- [80] T. Sakamoto, T. Iida, Y. Honda, M. Tada, T. Sekiguchi, K. Nishio, Y. Kogo, Y. Takanashi, *J. Electron. Mater.* **2012**, 41, 1805.

- [81] D. Ebling, K. Bartholomé, M. Bartel, M. Jägle, *J. Electron. Mater.* **2010**, 39, 1376.
- [82] R. Björk, *J. Electron. Mater.* **2015**, 44, 2869.
- [83] T. Dahal, Q. Jie, G. Joshi, S. Chen, C. Guo, Y. Lan, Z. Ren, *Acta Mater.* **2014**, 75, 316.
- [84] S. Aminorroaya Yamini, H. Wang, D. Ginting, D. R. Mitchell, S. X. Dou, G. J. Snyder, *ACS Appl. Mater. Interfaces* **2014**, 6, 11476.
- [85] P. Ziolkowski, P. Poinas, J. Leszczynski, G. Karpinski, E. Müller, *J. Electron. Mater.* **2010**, 39, 1934.
- [86] O. Höglblom, R. Andersson, *J. Electron. Mater.* **2014**, 43, 2247.
- [87] Z. Ouyang, D. Li, *Sci. Rep.* **2016**, 6.
- [88] W. Liu, X. Yan, G. Chen, Z. Ren, *Nano Energ.* **2012**, 1, 42.
- [89] G. Rogl, P. Rogl, *Current Opinion in Green and Sustainable Chemistry* **2017**.
- [90] L. Huang, Q. Zhang, B. Yuan, X. Lai, X. Yan, Z. Ren, *Materials Research Bulletin* **2016**, 76, 107.
- [91] Q. Zhang, J. Liao, Y. Tang, M. Gu, C. Ming, P. Qiu, S. Bai, X. Shi, C. Uher, L. Chen, *Energy Environ. Sci.* **2017**, 10, 956.
- [92] S. K. Yee, S. LeBlanc, K. E. Goodson, C. Dames, *Energy Environ. Sci.* **2013**, 6, 2561.
- [93] S. LeBlanc, S. K. Yee, M. L. Scullin, C. Dames, K. E. Goodson, *Renew. Sustain. Energy Rev.* **2014**, 32, 313.
- [94] H. Kim, W. Kim, *Appl. Energy* **2015**, 139, 205.
- [95] N. S. Benday, D. M. Dryden, K. Kornbluth, P. Stroeve, *Appl. Energy* **2017**, 190, 764.
- [96] L.-D. Zhao, G. Tan, S. Hao, J. He, Y. Pei, H. Chi, H. Wang, S. Gong, H. Xu, V. P. Dravid, *Science* **2015**, aad3749.
- [97] X. Meng, Z. Liu, B. Cui, D. Qin, H. Geng, W. Cai, L. Fu, J. He, Z. Ren, J. Sui, *Adv. Energy Mater.* **2017**.
- [98] K. S. Kim, Y. M. Kim, H. Mun, J. Kim, J. Park, A. Y. Borisevich, K. H. Lee, S. W. Kim, *Adv. Mater.* **2017**.

- [99] S. Chen, Z. Ren, *Materials today* **2013**, 16, 387.
- [100] T. J. Hendricks, S. Yee, S. LeBlanc, *J. Electron. Mater.* **2016**, 45, 1751.
- [101] E. Hazan, O. Ben - Yehuda, N. Madar, Y. Gelbstein, *Adv. Energy Mater.* **2015**, 5.
- [102] X. Hu, P. Jood, M. Ohta, M. Kunii, K. Nagase, H. Nishiate, M. G. Kanatzidis, A. Yamamoto, *Energ. Environ. Sci.* **2016**, 9, 517.
- [103] G. Joshi, B. Poudel, *J. Electron. Mater.* **2016**, 45, 6047.
- [104] C. Fu, S. Bai, Y. Liu, Y. Tang, L. Chen, X. Zhao, T. Zhu, *Nat. Commun.* **2015**, 6.
- [105] H. Zhou, X. Mu, W. Zhao, D. Tang, P. Wei, W. Zhu, X. Nie, Q. Zhang, *Nano Energ.* **2017**, 40, 274.
- [106] R. He, D. Kraemer, J. Mao, L. Zeng, Q. Jie, Y. Lan, C. Li, J. Shuai, H. S. Kim, Y. Liu, *Proc. Natl. Acad. Sci.* **2016**, 113, 13576.
- [107] H. S. Kim, W. Liu, G. Chen, C.-W. Chu, Z. Ren, *Proc. Natl. Acad. Sci.* **2015**, 112, 8205.
- [108] P. Löper, M. Stuckelberger, B. Niesen, J. Werner, M. Filipič, S.-J. Moon, J.-H. Yum, M. Topič, S. De Wolf, C. Ballif, *The journal of physical chemistry letters* **2014**, 6, 66.
- [109] K. Domanski, E. A. Alharbi, A. Hagfeldt, M. Grätzel, W. Tress, *Nat. Energy* **2018**, 1.
- [110] F. Li, M. Liu, *J. Mater. Chem. A* **2017**, 5, 15447.
- [111] I. Mesquita, L. Andrade, A. Mendes, *Renew. Sustain. Energy Rev.* **2017**.
- [112] J.-P. Correa-Baena, M. Saliba, T. Buonassisi, M. Grätzel, A. Abate, W. Tress, A. Hagfeldt, *Science* **2017**, 358, 739.
- [113] M. L. Petrus, J. Schlipf, C. Li, T. P. Gujar, N. Giesbrecht, P. Müller - Buschbaum, M. Thelakkat, T. Bein, S. Hüttner, P. Docampo, *Adv. Energy Mater.* **2017**.
- [114] M. Asghar, J. Zhang, H. Wang, P. Lund, *Renew. Sustain. Energy Rev.* **2017**, 77, 131.
- [115] J. You, Z. Hong, Y. Yang, Q. Chen, M. Cai, T.-B. Song, C.-C. Chen, S. Lu, Y. Liu, H. Zhou, *ACS Nano* **2014**, 8, 1674.
- [116] Q. An, F. Zhang, L. Li, J. Wang, J. Zhang, L. Zhou, W. Tang, *ACS Appl. Mater. Interfaces* **2014**, 6, 6537.

- [117] Y. Li, L. Meng, Y. M. Yang, G. Xu, Z. Hong, Q. Chen, J. You, G. Li, Y. Yang, Y. Li, *Nat. Commun.* **2016**, 7, 10214.
- [118] W. Tress, M. Yavari, K. Domanski, P. Yadav, B. Niesen, J. P. C. Baena, A. Hagfeldt, M. Graetzel, *Energy Environ. Sci.* **2018**, 11, 151.
- [119] Y. Wang, M. I. Dar, L. K. Ono, T. Zhang, M. Kan, Y. Li, L. Zhang, X. Wang, Y. Yang, X. Gao, *Science* **2019**, 365, 591.
- [120] Y. Zhong, R. Munir, J. Li, M.-C. Tang, M. R. Niazi, D.-M. Smilgies, K. Zhao, A. Amassian, *ACS Energy Lett.* **2018**, 3, 1078.
- [121] C. Li, J. Yin, R. Chen, X. Lv, X. Feng, Y. Wu, J. Cao, *J. Am. Chem. Soc.* **2019**, 141, 6345.
- [122] Z. Li, T. R. Klein, D. H. Kim, M. Yang, J. J. Berry, M. F. van Hest, K. Zhu, *Nature Reviews Materials* **2018**, 3, 18017.
- [123] P. Cheng, H. Bai, N. K. Zawacka, T. R. Andersen, W. Liu, E. Bundgaard, M. Jørgensen, H. Chen, F. C. Krebs, X. Zhan, *Adv. Sci.* **2015**, 2.
- [124] T. M. Schmidt, T. T. Larsen-Olsen, J. E. Carle, D. Angmo, F. C. Krebs, *Adv. Energy Mater.* **2015**, 5.
- [125] D. H. Kim, J. B. Whitaker, Z. Li, M. F. van Hest, K. Zhu, *Joule* **2018**, 2, 1437.
- [126] J. Xu, Z. Hu, X. Jia, L. Huang, X. Huang, L. Wang, P. Wang, H. Zhang, J. Zhang, *Org. Electron.* **2016**, 34, 84.
- [127] K.-L. Wang, C.-C. Zhang, Y.-R. Jiang, H.-R. Liu, X.-M. Li, S. M. Jain, H. Ma, *New Journal of Chemistry* **2019**.
- [128] Q. Cao, S. Yang, Q. Gao, L. Lei, Y. Yu, J. Shao, Y. Liu, *ACS Appl. Mater. Interfaces* **2016**, 8, 7854.
- [129] T. Jeon, H. M. Jin, S. H. Lee, J. M. Lee, H. I. Park, M. K. Kim, K. J. Lee, B. Shin, S. O. Kim, *ACS nano* **2016**, 10, 7907.
- [130] F. Li, W. Zhu, C. Bao, T. Yu, Y. Wang, X. Zhou, Z. Zou, *Chem. Comm.* **2016**, 52, 5394.
- [131] R. Muydinov, S. Seeger, S. H. B. V. Kumar, C. Klimm, R. Krahnert, M. R. Wagner, B. Szyszka, *Thin Solid Films* **2018**, 653, 204.
- [132] K. Ankireddy, A. H. Ghahremani, B. Martin, G. Gupta, T. Druffel, *J. Mater. Chem. A*

**2018**, **6**, 9378.

- [133] M. I. Ahmad, D. G. Van Campen, J. D. Fields, J. Yu, V. L. Pool, P. A. Parilla, D. S. Ginley, M. F. Van Hest, M. F. Toney, *Review of Scientific Instruments* **2015**, **86**, 013902.
- [134] S. Sanchez, N. Christoph, B. Grobety, N. Phung, U. Steiner, M. Saliba, A. Abate, *Adv. Energy Mater.* **2018**, **8**, 1802060.
- [135] J. Park, J. W. Choi, W. Kim, R. Lee, H. C. Woo, J. Shin, H. Kim, Y. J. Son, J. Y. Jo, H. Lee, *RSC Adv.* **2019**, **9**, 14868.
- [136] B. Dou, V. L. Pool, M. F. Toney, M. F. van Hest, *Chem. Mater.* **2017**, **29**, 5931.
- [137] S. Sanchez, X. Hua, N. Phung, U. Steiner, A. Abate, *Adv. Energy Mater.* **2018**, **8**, 1702915.
- [138] S. Sánchez, M. Vallés-Pelarda, J.-A. Alberola-Borràs, R. Vidal, J. J. Jerónimo-Rendón, M. Saliba, P. P. Boix, I. Mora-Seró, *Materials Today* **2019**.
- [139] K. Bruening, B. Dou, J. Simonaitis, Y.-Y. Lin, M. F. van Hest, C. J. Tassone, *Joule* **2018**, **2**, 2464.
- [140] J. Lee, H. Kang, G. Kim, H. Back, J. Kim, S. Hong, B. Park, E. Lee, K. Lee, *Adv. Mater.* **2017**, **29**, 1606363.
- [141] Y. Deng, C. H. Van Bracke, X. Dai, J. Zhao, B. Chen, J. Huang, *Science Advances* **2019**, **5**, eaax7537.
- [142] M. Yang, D. H. Kim, T. R. Klein, Z. Li, M. O. Reese, B. J. Tremolet de Villers, J. J. Berry, M. F. van Hest, K. Zhu, *ACS Energy Lett.* **2018**, **3**, 322.
- [143] W. Shockley, H. J. Queisser, *J. Appl. Phys.* **1961**, **32**, 510.
- [144] P. K. Kung, M. H. Li, P. Y. Lin, Y. H. Chiang, C. R. Chan, T. F. Guo, P. Chen, *Advanced Materials Interfaces* **2018**, **5**, 1800882.
- [145] Q. Jiang, X. Zhang, J. You, *Small* **2018**, **14**, 1801154.
- [146] L. Xiong, Y. Guo, J. Wen, H. Liu, G. Yang, P. Qin, G. Fang, *Adv. Func. Mater.* **2018**, **28**, 1802757.
- [147] P. Zhao, B. J. Kim, X. Ren, D. G. Lee, G. J. Bang, J. B. Jeon, W. B. Kim, H. S. Jung, *Adv. Mater.* **2018**, **30**, 1802763.

- [148] R. Singh, P. K. Singh, B. Bhattacharya, H.-W. Rhee, *Applied Materials Today* **2019**, 14, 175.
- [149] M. Saliba, T. Matsui, J.-Y. Seo, K. Domanski, J.-P. Correa-Baena, M. K. Nazeeruddin, S. M. Zakeeruddin, W. Tress, A. Abate, A. Hagfeldt, *Energy Environ. Sci.* **2016**, 9, 1989.

## APPENDIX

### LIST OF PUBLICATIONS AND PATENTS

#### **Journal Publications**

1. **Zhongliang Ouyang**, Henry Abrams, Robert Bergstone, Quantao Li, Feng Zhu, and Dawen Li\*, “Rapid Layer-Specific Annealing Enabled by Ultraviolet LED with Estimation of Crystallization Energy for High-Performance Perovskite Solar Cells”, *Advanced Energy Materials*, 2019, 1902898. Inside front cover.
2. **Zhongliang Ouyang** and Dawen Li\*, "Design of segmented high-performance thermoelectric generators with cost in consideration", *Applied Energy*, 221, 112-121 (2018).
3. **Zhongliang Ouyang** and Dawen Li\*, "Modelling of segmented high-performance thermoelectric generators with effects of thermal radiation, electrical and thermal contact resistances", *Scientific Reports*, 6, 24123 (2016)
4. Ziyou Zhou, Shoieb Shaik, **Zhongliang Ouyang**, Feng Yan, and Dawen Li\*, "Controllable growth of perovskite thin films via a seeded approach", *Journal of Vacuum Science and Technology A*, 37, 021201 (2019). Featured article.
5. Sheng Bi, **Zhongliang Ouyang**, Shoieb Shaik, and Dawen Li\*, "Effect of Donor-Acceptor Vertical Composition Profile on Efficiency of Organic Bulk Heterojunction

Solar Cells", *Scientific Reports*, 8, 9574 (2018)

6. **Zhongliang Ouyang**, Mengjin Yang, James B. Whitaker, Dawen Li\* and Maikel F. A. M. van Hest\*, "Towards scalable perovskite solar modules using blade-coating and rapid thermal processing", paper in preparation, (2020).
7. Shoieb Shaik<sup>†</sup>, Ziyou Zhou<sup>†</sup>, **Zhongliang Ouyang**<sup>†</sup>, Rebecca Han, and Dawen Li\*, "Polymer additive assisted fabrication of compact and ultra-smooth perovskite thin films with fast lamp annealing", paper in preparation, (2020).

## Patents

1. Dawen Li and **Zhongliang Ouyang**, "Rapid Metal Oxide Layer-Specific Photonic Treatment Using UV LED for Fabrication of Flexible Perovskite Structures", utility patent (US16/247,055) filed in 2019.
2. Dawen Li and **Zhongliang Ouyang**, "Rapid Layer-Specific Photonic Treatment for High-Speed Printing of Perovskite Layers", provisional patent (62/748,626), 2018